

**BINARY CLUSTERS PRODUCED WITH CLUSTER BEAM
DEPOSITION FOR ELECTROCHEMISTRY AND
HETEROGENEOUS CATALYSIS**

by

Yubiao Niu

A thesis submitted to the University of Birmingham for the degree of

DOCTOR OF PHILOSOPHY



Nanoscale Physics Research Laboratory

School of Physics & Astronomy

University of Birmingham

September 2018

UNIVERSITY OF
BIRMINGHAM

University of Birmingham Research Archive

e-theses repository

This unpublished thesis/dissertation is copyright of the author and/or third parties. The intellectual property rights of the author or third parties in respect of this work are as defined by The Copyright Designs and Patents Act 1988 or as modified by any successor legislation.

Any use made of information contained in this thesis/dissertation must be in accordance with that legislation and must be properly acknowledged. Further distribution or reproduction in any format is prohibited without the permission of the copyright holder.

Abstract

This thesis describes the production, characterisation and catalytic performance of nanoclusters fabricated by cluster beam deposition using the magnetron sputtering, gas condensation technique. MoS₂-based clusters and Au-based clusters are demonstrated in electrochemistry (HER) and gas phase heterogeneous catalysis (CO oxidation), respectively. The atomic structure analysis of the clusters was performed with aberration-corrected scanning transmission electron microscope with high angle annular dark field (HAADF-STEM). Size-controlled (MoS₂)₃₀₀ clusters deposited on amorphous carbon present an incomplete multi-layer structure with the absence of extended crystalline order. Such a layered structure was also found in Ni-MoS₂ hybrid clusters [with a mass corresponding to (MoS₂)₁₀₀₀] produced by dual target magnetron sputtering. Compared with MoS₂ clusters, a significant enhancement in HER activity by Ni-MoS₂ hybrid clusters was found. However, both MoS₂ clusters (Mo:S = 1:0.9) and Ni-MoS₂ clusters (Mo:S = 1:1.8) present a sulphur-deficient composition. In order to overcome the sulphur deficiency of the MoS₂ clusters, a sulphur-enrichment technique based on a combination of sulphur addition (by sublimation) and annealing inside the cluster beam vacuum chamber was performed on size-selected (MoS₂)₁₀₀₀ clusters. This process led to a notable increase in extended crystallinity and a moderate increase in size (from 5.5 nm to 6.0 nm in diameter). Compared with Ni-MoS₂ clusters, the sulphur-enriched MoS₂ clusters show even more enhancement on the HER activities with more than 30-fold increases in exchange current densities.

We have demonstrated a method of inhibiting the sintering of Au clusters in Au-based catalysis by exploring the stabilisation of supported Au clusters against sintering by alloying with Ti. Size-selected Au₂₀₅₇ (405, 229 amu) clusters and similar mass Au/Ti nanoalloy clusters (400, 000 amu) were produced by cluster beam deposition onto thin silica films. A strong anchoring

effect was found in the case of Au/Ti clusters by HAADF-STEM experiments, consistent with DFT calculations by collaborators. Different sintering mechanisms were revealed between Au cluster dimers and Au/Ti cluster dimers. Preliminary CO oxidation measurements on Au and Au/Ti clusters indicates that Au/Ti clusters are promising as catalysts. Au/Ti clusters show catalytic activity on CO oxidation while Au clusters are non-active due to the serious sintering and the support effect.

Acknowledgements

First, I would like to say thank you to Prof. Richard E. Palmer for providing me with the opportunity to study in NPRL and your excellent guidance; to Dr Andrey Kaplan and Dr Neil V. Rees for helping me on the research work.

I would like to thank Prof. Feng Yin for training me on the cluster beam source and sharing a lot of his valuable experience; to Dr Nan Jian, Dr Kuo-Juei Hu, Dr Jian Liu and Dr Caroline Blackmore for training me on STEM and helping me with image analysis.

I would also like to say thanks to everyone else from NPRL for friendship, companion and help.

I would like to extend my gratitude to Daniel Escalera López for the joint project on MoS₂ clusters; to Béla Sebök and Philomena Schlexer for the joint project on Au/Ti; to Dr Jinlonf Yin from Teer Coatings Ltd and Prof. Peter Lievens from KU Leuven for the help on secondments, to everyone in the CATSENSE project for having fun and learning together.

Last but not the least, I would like to say special thanks to my parents and brother for their selfless love and great help.

Author's Publications

- [1] Escalera-López D, **Niu Y**, Yin J, Cooke K, Rees NV, Palmer RE. Enhancement of the hydrogen evolution reaction from Ni-MoS₂ hybrid nanoclusters. *ACS Catalysis* 2016, 6(9): 6008-6017.
- [2] **Niu Y**, Park S, Palmer R. Modification of deposited, size-selected MoS₂ nanoclusters by sulphur addition: An aberration-corrected stem study. *Inorganics* 2016, 5(4): 1.
- [3] **Niu Y**, Schlexer P, Sebok B, Chorkendorff I, Pacchioni G, Palmer RE. Reduced sintering of mass-selected Au clusters on SiO₂ by alloying with Ti: an aberration-corrected STEM and computational study. *Nanoscale* 2018, 10(5): 2363-2370.
- [4] Escalera-López D, **Niu Y**, Park S, Isaacs M, Wilson K, Palmer RE, Rees NV. Hydrogen evolution enhancement of ultra-low loading, size-selected molybdenum sulfide nanoclusters by sulfur enrichment. *Applied Catalysis B: Environmental* 2018, 235: 84-91.

Table of Contents

Abstract	i
Acknowledgements	iii
Author's Publications	iv
Table of Contents	v
List of Figures	viii
List of Tables	xi
Abbreviations	xii
Chapter 1 Introduction and Background	1
1.1 Cluster Science.....	1
1.2 Catalysis with Clusters	3
1.2.1 What Catalysis is and Why Clusters	3
1.2.2 Cluster Beam Deposition Techniques	11
1.2.3 Catalysis in Energy and Environment	19
1.2.4 Au Nanocatalysis and Sintering.....	23
References	29
Chapter 2 Experimental Methods	44
2.1 Cluster Beam Deposition.....	45
2.1.1 Cluster beam source	45
2.1.2 Cluster Formation.....	46
2.1.3 Cluster Beam Optics.....	47
2.1.4 Time-of-Flight Mass Filter	48

2.1.5 Cluster Deposition.....	51
2.2 Scanning Transmission Electron Microscopy (STEM)	53
2.2.1 Electron Source	54
2.2.2 Lens and Aberration	55
2.2.3 Imaging System and Z-Contrast Images.....	59
2.3 Electrochemical Measurement.....	62
2.4 Micro-reactor	65
2.5 Other Techniques	67
2.5.1 X-ray Photoelectron Spectroscopy	67
2.5.2 Low Energy Ion Scattering	68
References	70

Chapter 3 Atomic Structures and HER Activities of MoS₂ Clusters and Ni-MoS₂

clusters.....	73
3.1 Introduction.....	73
3.2 Materials and Methods	75
3.3 Structure and Composition Analysis of the Clusters	78
3.4 Electrocatalytic Activity to HER	89
3.5 Conclusions.....	94
References	96

Chapter 4 Modification of Deposited, Size-Selected MoS₂ Clusters by Sulphur-

Enrichment and Their HER Activities.....	102
4.1 Introduction.....	102
4.2 Materials and Methods	103
4.3 Atomic Structure of As-Deposited MoS ₂ Clusters	105
4.4 Atomic Structure of Sulphur-Added MoS ₂ Clusters.....	112

4.5 The Effect of The Sulphur Addition and Annealing Treatment	116
4.6 Electrocatalytic Activity to HER	118
4.7 Conclusions.....	121
References	122
Chapter 5 Reduced Sintering of Mass-Selected Au Clusters on SiO₂ by Alloying with Ti	126
5.1 Introduction.....	126
5.2 Materials and Methods	128
5.3 STEM Study of the Sintering Process.....	130
5.4 XPS and LEIS of the clusters	137
5.5 DFT Calculations of Surface Anchoring.....	140
5.6 CO Oxidation on Au and Au/Ti clusters.....	144
5.7 Conclusions.....	147
References	149
Chapter 6 Conclusions and Outlook	154

List of Figures

Figure 1.1	Time-of-flight mass spectra of positively charged Ta and Nb clusters.	2
Figure 1.2	CO oxidation activity of Au supported on TiO ₂ as a function of the size of Au nanoparticles.	3
Figure 1.3	Illustration of the primary catalytic process.	5
Figure 1.4	Catalytic activities of Pt _n (n = 1 to 14) clusters supported on indium tin oxide to ethanol oxidation reaction.	9
Figure 1.5	CO oxidation on size-selected Au, Pt, Pd and Rh clusters.	10
Figure 1.6	The catalytic activity and stability of mass-selected PtGd clusters for oxygen reduction reaction.	10
Figure 1.7	Schematic of seeded supersonic nozzle cluster source.	12
Figure 1.8	Schematic of laser ablation cluster source.	13
Figure 1.9	Schematic illustration of the size selected cluster beam source in NPRL.	15
Figure 1.10	Schematic of the pulsed arc discharge cluster source.	16
Figure 1.11	Schematic of the liquid metal cluster source.	17
Figure 1.12	Schematic of the principle of the matrix assembly cluster source.	18
Figure 1.13	Global primary energy consumption from 1992 to 2017.	20
Figure 1.14	Shares of global primary energy consumption from 1965 to 2017.	20
Figure 1.15	Schematic of electrochemical water splitting.	21
Figure 1.16	The sandwich structure of MoS ₂ monolayer.	22
Figure 1.17	Catalytic activities of Au particle for CO oxidation.	25
Figure 1.18	Schematic of the reaction mechanisms for CO oxidation on supported Au nanoparticles.	26
Figure 2.1	Schematic illustration of the size selected cluster beam source in our group.	45
Figure 2.2	Schematic illustration of the cluster generation chamber.	47
Figure 2.3	Schematic illustration of the ion optics chamber.	48
Figure 2.4	Schematic illustration of the Time-of-Flight chamber.	49
Figure 2.5	Schematic of the principle of the lateral Time-of-Flight mass filter.	50
Figure 2.6	Sample holder schematics.	52
Figure 2.7	Schematic of an aberration-corrected STEM and a photograph of the JEOL 2100F STEM in our group.	53
Figure 2.8	A very fine field emission gun tip and a schematic of the configuration in a FEG.	55
Figure 2.9	Schematic diagram of magnetic lens used in the TEM.	56
Figure 2.10	Schematic of spherical aberration.	57
Figure 2.11	Schematic of hexapole and electron beam shape after passing through the hexapole.	58

Figure 2.12	Configuration of the double-hexapole corrector and the beam shapes at first and second hexapole.	59
Figure 2.13	Schematic diagram of high angle and low angle elastic scattering, and detector setup in STEM.	60
Figure 2.14	Schematic of a standard three-electrode set-up.	63
Figure 2.15	An example graph of LSV and Tafel plot based on two theoretical catalysts.	65
Figure 2.16	A photograph of micro-reactor and a schematic diagram of the design of microreactor.	66
Figure 2.17	Schematic of X-ray photoelectron spectroscopy.	68
Figure 2.18	Schematic of the principle of low energy ion scattering.	69
Figure 3.1	Schematic of the cluster beam system.	76
Figure 3.2	Mass spectra obtained by time-of-flight.	79
Figure 3.3	STEM images and size distribution in diameter based on the cluster surface area..	80
Figure 3.4	STEM image and EDX mapping of Ni-MoS ₂ clusters.	81
Figure 3.5	STEM image of Ni-MoS ₂ hybrid cluster and example HAADF intensity line profile.	82
Figure 3.6	Detailed XPS spectra of Mo 3d and S 2p for fresh and 14 h air exposed (MoS ₂) ₃₀₀ clusters.	85
Figure 3.7	Detailed XPS spectra of Mo 3d and S 2p for fresh and 14 h air exposed (Ni-MoS ₂) ₁₀₀₀ clusters.	86
Figure 3.8	Detailed XPS spectra of Ni 2p fresh and 14 h air exposed Ni clusters.	88
Figure 3.9	Detailed XPS spectra of Ni 3d for fresh and 14 h air exposed (Ni-MoS ₂) ₁₀₀₀ clusters.	88
Figure 3.10	Linear sweep voltammograms recorded at 5 mm diameter glassy carbon modified with clusters.	89
Figure 3.11	Tafel plots of the Ni-doped/undoped MoS ₂ clusters with scan rate: 25 mV s ⁻¹ .	93
Figure 4.1	Schematic illustration of the size selected cluster beam source together with sulphur addition chamber.	104
Figure 4.2	STEM images of as-deposited size-selected (MoS ₂) ₁₀₀₀ clusters shown.	106
Figure 4.3	HAADF-STEM image and simulated structure of side-on (MoS ₂) ₆₅₀ cluster (bilayer).	108
Figure 4.4	STEM images of (MoS ₂) ₁₀₀₀ clusters deposited on amorphous carbon.	109
Figure 4.5	STEM image of annealed (MoS ₂) ₁₀₀₀ clusters deposited on silica.	110
Figure 4.6	STEM images of (MoS ₂) ₅₀₀ clusters deposited on amorphous carbon and silica.	111
Figure 4.7	STEM images of (MoS ₂) ₁₀₀₀ clusters with sulphur addition and annealing.	113
Figure 4.8	Detailed Mo 3d and S 2p XPS spectra of sulphurised, annealed (MoS ₂) ₁₀₀₀ clusters.	115
Figure 4.9	STEM images of MoS ₂ clusters after annealing only and after sulphur addition only of as-deposited samples, (MoS ₂) ₁₀₀₀ .	117
Figure 4.10	Linear sweep voltammograms of glassy carbon samples modified with clusters	119
Figure 5.1	Schematic illustration of the two sintering mechanisms of supported particles.	127
Figure 5.2	STEM images of dimers of Au ₂₀₅₇ and of Au/Ti clusters continuously exposed to electron beam irradiation.	131

Figure 5.3	The length of the major axis of the cluster dimers as a function of the time of exposure to the electron beam.	132
Figure 5.4	Sintering process of Au ₂₀₅₇ dimer continuously exposed to electron beam irradiation.	133
Figure 5.5	Sintering process of Au ₂₀₅₇ dimer continuously exposed to electron beam irradiation.	134
Figure 5.6	STEM images of Au/Ti (400k amu) cluster dimer with two connected clusters continuously exposed to electron beam irradiation.	134
Figure 5.7	STEM images of Au/Ti cluster dimers with a larger gap continuously exposed to electron beam irradiation.	135
Figure 5.8	STEM images of Au/Ti cluster dimer continuously exposed to electron beam irradiation.	136
Figure 5.9	XPS spectra of Au ₂₀₅₇ and Au/Ti clusters deposited on Si/SiO ₂ slabs.	137
Figure 5.10	Detailed XPS spectra of the Ti 2p region.	138
Figure 5.11	LEIS spectra of Au ₂₀₅₇ and Au/Ti clusters deposited on Si/SiO ₂ slabs.	139
Figure 5.12	Top and side views of Au ₂₀ supported on the fully hydroxylated α -quartz (001) surface from DFT simulations.	142
Figure 5.13	CO oxidation activity measurements of the first pair of Au ₂₀₅₇ and Au/Ti (400k amu) micro-reactor samples.	144
Figure 5.14	SEM images of Au ₂₀₅₇ and Au/Ti (400k amu) clusters before and after 100°C for 1 h in 1 bar of O ₂ :CO=4:1 mixture.	146
Figure 5.15	Size distributions of Au ₂₀₅₇ and Au/Ti (400k amu) clusters before and after 100°C for 1 h in 1 bar of O ₂ :CO=4:1 mixture.	147

List of Tables

Table 1.1	Summary of cluster beam sources.	19
Table 3.1	Composition analysis of six hybrid Ni-MoS₂ clusters based on HAADF-STEM images.	84
Table 5.1	Adsorption energies E_{ADS} (eV), average Bader charges $q_{\text{AVG}}(\text{Au or Ti})$ (e) on the Au or Ti atoms in the cluster and total Bader charge on the cluster $q_{\text{TOT}}(\text{Cluster})$ (e) from DFT simulations.	142

Abbreviations

STM	Scanning Tunnelling Electron Microscope/Microscopy
TEM	Transmission Electron Microscope/Microscopy
XPS	X-ray Photoelectron Spectroscopy
AFM	Atomic Force Microscopy
HER	Hydrogen Evolution Reaction
OER	Oxygen Evolution Reaction
TMD	Transition Metal Dichalcogenide
HV	High Vacuum
STEM	Scanning Transmission Electron Microscope/Microscopy
Cs	Spherical Aberration
HAADF	High Angle Annular Dark Field
BF	Bright Field
FEG	Field Emission Gun
DF	Dark Field
CV	Cyclic Voltammograms
LSV	Linear Sweep Voltammograms
SCE	Saturated Calomel Electrode
WE	Working Electrode

RE	Reference Electrode
CE	Counter Electrode
SHE	Standard Hydrogen Electrode
QMS	Quadrupole Mass Spectrometer
GC	Glassy Carbon
sccm	Standard Cubic Centimetres Per Minute
EDX	Energy Dispersive X-ray Spectroscopy
FFT	Fast Fourier Transformation
NHE	Normal Hydrogen Electrode
CVD	Chemical Vapour Deposition
ORR	Oxygen Reduction Reaction
LEIS	Low Energy Ion Scattering
SEM	Scanning Electron Microscope

Chapter 1

Introduction and Background

1.1 Cluster Science

Clusters, or equivalently nanoclusters, are generally defined as collections of 2 to $\sim 10^6$ atoms with a diameter lying between a few angstroms and ~ 20 nm. The establishment of the field of cluster science can be dated back to early 1980's when the "magic numbers" were discovered [1, 2]. It turned out that particularly stable electronic configurations can be found in clusters consisting of certain numbers of atoms (magic number). For example, Figure 1.1 shows the time-of-flight mass spectra of positively ionised Ta and Nb clusters produced from laser ablation cluster source [3]. It can be found that the spectra intensities of both Ta and Nb clusters with $n = 7, 13, 15, 22, 29$ are much higher than those of neighbouring clusters. Those n values are called magic numbers, and those clusters with magic numbers are traditionally considered to be easily formed in the gas phase and more stable than the ones lying between the magic numbers [4-6]. At the same time, the invention of the scanning tunnelling microscope (STM) [7] and electrochemical STM [8] together with the continuous improvement of the resolution of the transmission electron microscope (TEM) delivered the capability to directly image individual clusters [9, 10], which has notably promoted the evolution of cluster science. In addition, with the development of more sophisticated theoretical treatment of clusters as well as the prospect of applications in material science, scientific interest in cluster science is growing [11, 12].

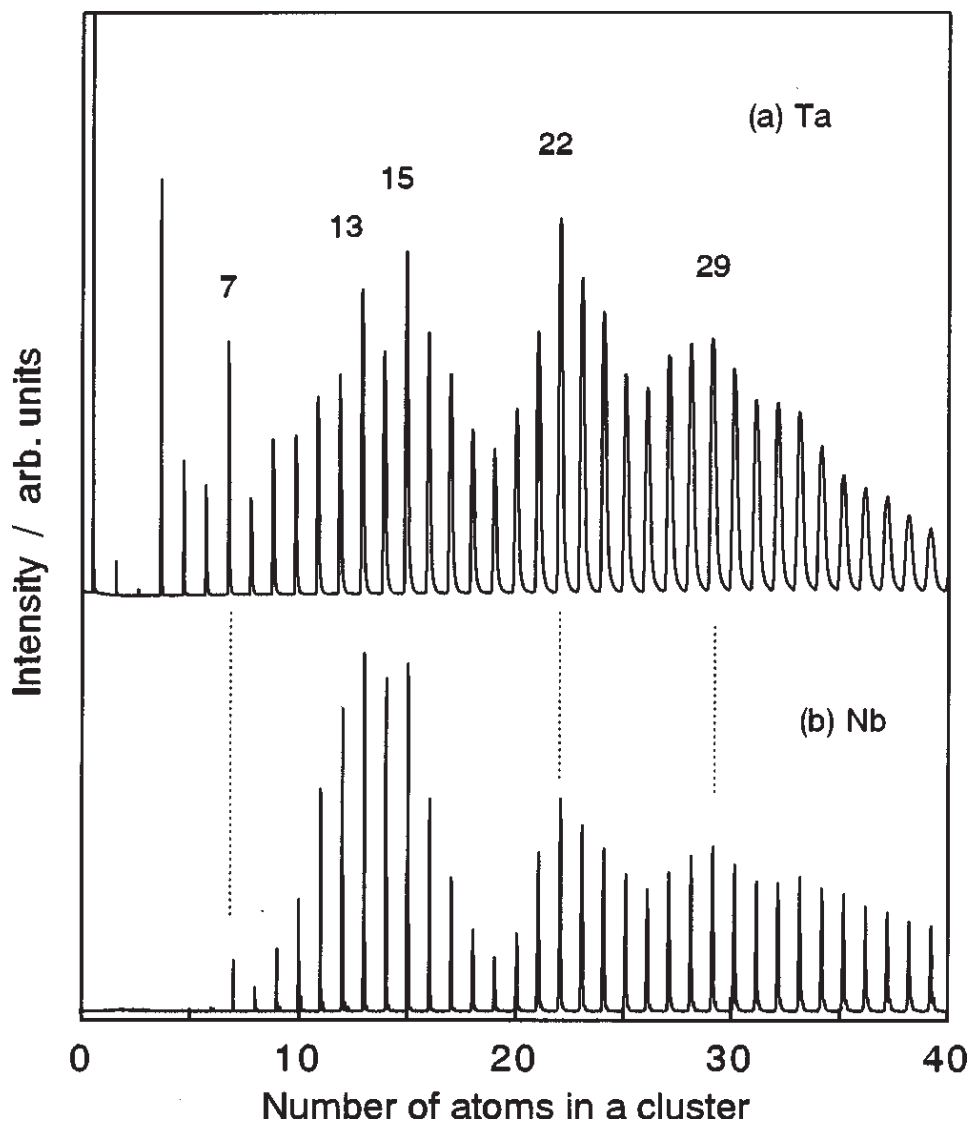


Figure 1.1 Time-of-flight mass spectra of positively charged Ta and Nb clusters fabricated from a laser ablation cluster source. The figure was reproduced from reference[3].

Cluster science emphasises the unique size-dependent properties of clusters, which are distinctly different from the corresponding bulk materials or individual atoms [13, 14]. For example, the catalytic activity to CO oxidation over Au/TiO₂ shown in Figure 1.2 presents a strong size-dependent characteristic [15]. The reasons behind this are the increase of the surface area to bulk ratio and the change of the electronic band structure. When a material is shrunk from the bulk to the nanoscale, the surface area to bulk ratio significantly increases, introducing more edges and corners which are often identified as active sites in catalysis [16, 17]; these

new sites may bring new properties that cannot be found in bulk materials [18], for example, there may be an enhancement of the catalytic activities of bulk materials. At the same time, with the shrinking of the size, the electronic band structure will exhibit discrete energy levels [19, 20], which can dramatically alter the electronic properties of the clusters with consequence for the catalytic activities too.

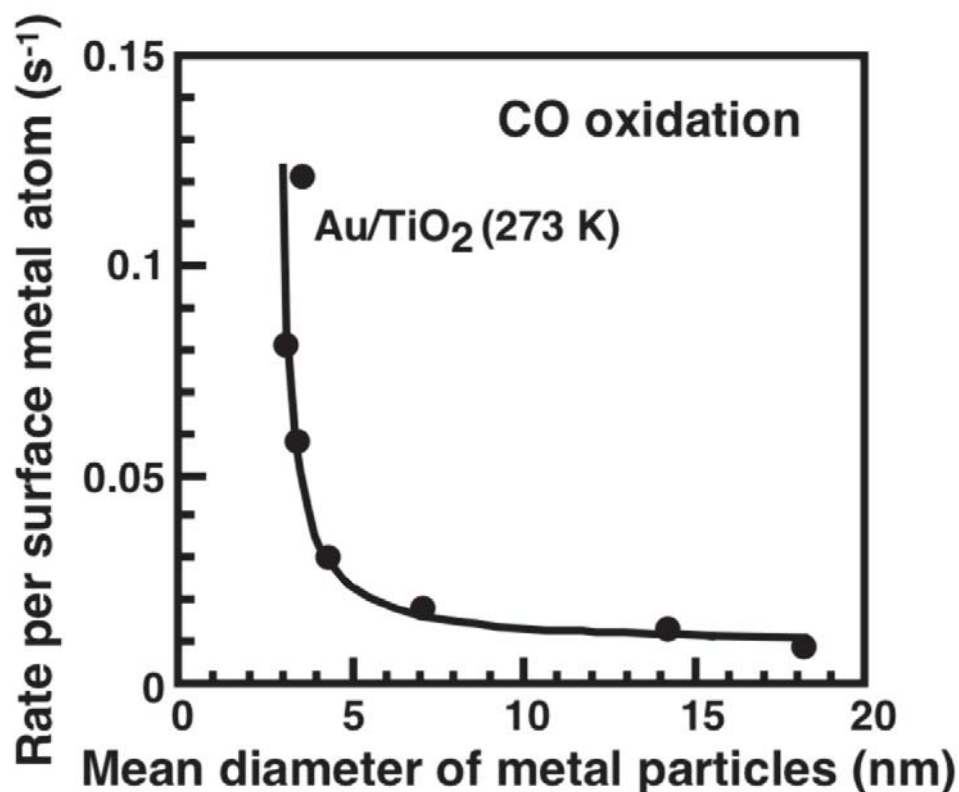


Figure 1.2 CO oxidation activity of Au supported on TiO₂ as a function of the size of Au nanoparticles, reproduced from reference [15].

1.2 Catalysis with Clusters

1.2.1 What Catalysis is and Why Clusters

Catalysis is ubiquitous and plays an increasingly important role both in nature and in the chemical industry [21-23]. A significant number of products, like fuels, fine chemicals,

medicines and many other valuable products used by society, would not be available without catalytic processes [24-26]. The definition of catalysis is that the increase in the rate of a chemical reaction due to the presence of catalyst, in which the catalyst participates in the chemical reaction but is not itself consumed [23, 27]. Due to the preservation of the catalyst during the reaction, it is able to keep on catalysing new reaction cycle. Catalysis can be typically divided into homogeneous catalysis and heterogeneous catalysis, according to the number of the phases involved in the catalytic reaction. If the catalyst is in the same phase as the reactants, the reaction is homogeneous. In contrast, if the catalyst is in a different phase from the reactants, the reaction is heterogeneous. Homogeneous catalysis is prevalent in biological systems like the enzyme processes in the human body, while many of the catalytic reactions (90%) in the chemical industry are heterogeneous [28], for example, ammonia synthesis and catalytic cracking of gas oil.

The primary catalytic process has been widely and intensively studied since the last century. It mainly consists of several elementary steps as illustrated in Figure 1.3: reactant molecules are adsorbed on the surface of catalyst, at the meantime dissociation might happen; the catalyst surface can facilitate to break bond(s) in adsorbed molecules; the adsorbate species then diffuse on the surface and collide with other species; reaction occurs and produces new products, which will eventually desorb from the surface of catalyst. The catalyst here plays a pivotal role to reduce the activation barrier and trigger a reaction with a high reaction rate [21]. From Figure 1.3, it can be found that the potential energy change is the same with or without the presence of the catalyst. However, the potential energy barrier is much higher without catalyst resulting in a low reaction rate and high energy consumption.

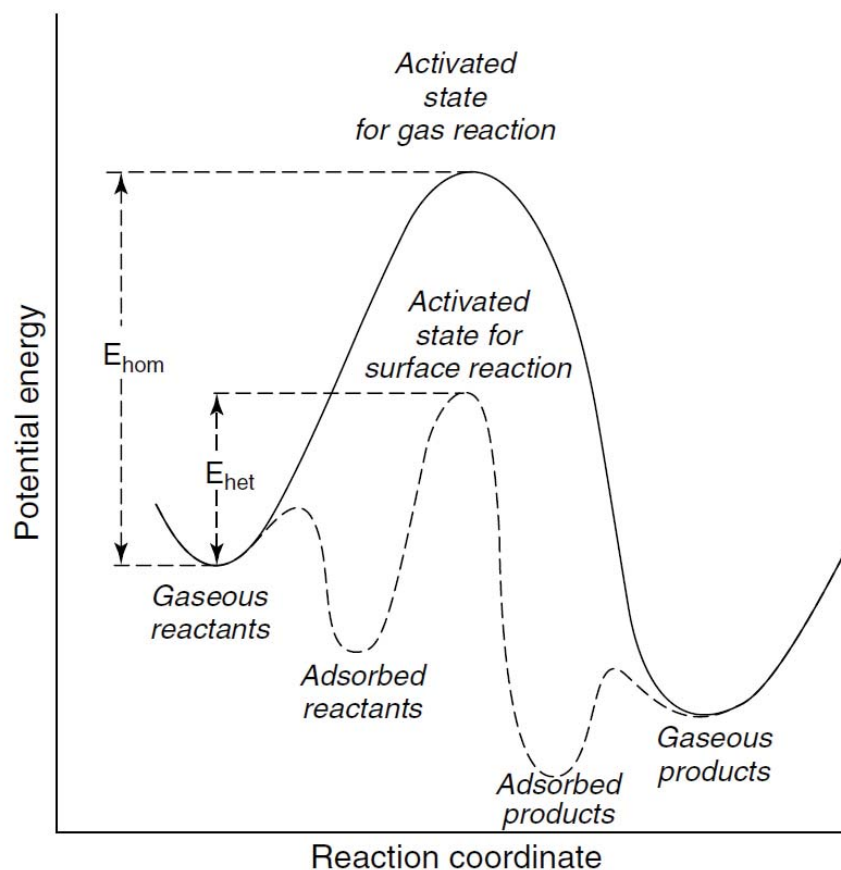


Figure 1.3 Illustration of the primary catalytic process, reproduced from reference [21]. The dotted curve shows the elementary steps for a reaction proceeding heterogeneously. It contains the adsorption of reactants, diffusion and reaction of surface species, and desorption of products; the solid curve corresponds to a homogeneous process without catalysis, in which a more significant energy barrier can be found.

During the early 20th century, the search for catalyst was mostly done by “trial and error” approach with different combinations of metals, sulfides and oxides [29]. Meanwhile, fundamental study also emerged initiated by Langmuir who proposed some basic ideas on surface science [30]. In 1925, another important concept of active site was brought up by Taylor, which suggests that under-coordinated surface atoms are more reactive than other surface

atoms [31]. Since then, the investigation of the elementary processes of heterogeneous catalysis has been the main motivation. Thus, rational design and synthesis of new catalysts with high activity have become the ultimate goal in the catalysis study.

Generally, the majority of industrial catalysts are particles in the sub-micron range supported on oxides (e.g. silica, alumina) [32]. Nanoparticles with dimensions less than 20 nm are gradually becoming attractive to catalysis since they can provide and expose as many active sites as possible. For example, supported Au nanoparticles with diameter below 2 nm are identified as the excellent catalyst to produce propene oxide which is a large-scale raw material in the polymer industry [33, 34]. Nanoparticles, especially for those with diameters of few nanometers or less, known as clusters, are attracting considerable interest in catalysis research due to an increased number of under-coordinated atoms [35]. Besides the catalytic property, clusters exhibit a vast range of fascinating properties like optical, magnetic and electronic properties, which cannot be found in bulk materials. This interesting behaviour is attributed to plenty of factors including electronic shell closing, geometric shell closing, superatomic character, quantum confinement, et al. [36-38]

Gas phase clusters are regarded as ideal candidates to model the catalytic reactions in early studies because of their well-defined composition and size. The initial studies on well-defined clusters used gas phase ions consisting of few atoms based on mass spectrometric techniques [39, 40]. These investigations gave fundamental insights into the reaction mechanisms in the oxidation of hydrocarbons, C-H bond cleavage, C-C bond scission and O₂ activation in the existence of clusters [41-44]. The emergence of supported clusters with selected composition and size gives a good connection between the fundamental gas phase study and the conventional applications of heterogeneous catalysis [45]. In addition, supported clusters make it possible to carefully investigate the support effects which are proved to be essential for many catalytic reactions [46]. Due to the small size of clusters and the considerable fraction of

interface atoms between clusters and support, support effects are more remarkable in the case of clusters than common nanoparticles, which makes it easier to study the details of these effects. Meanwhile, the research on supported clusters is also promoted by the characterization techniques for deposited clusters which includes scanning tunnelling microscopy (STM), transmission electron microscopy (TEM), X-ray photoelectron spectroscopy (XPS), atomic force microscopy (AFM), synchrotron techniques, etc. [47-51]

Controlling the size of clusters is becoming an essential way to increase the activity and tune the selectivity in a catalytic reaction. Additionally, multicomponent clusters with composition manipulated at the atomic level efficiently lead to study synergistic relationships. For instance, Pt/Cu alloys containing Pt atoms present both excellent selectivity and outstanding activity for hydrogenation of 1,3-butadiene to butenes [52]; Ag@Au core-shell nanoparticles show much higher catalytic activity to glucose oxidation than that of monometallic Au or Ag nanoparticles due to the electronic effect between the Au and Ag elements in one nanoparticle [53]. The research on cluster catalysis provides a fascinating opportunity to make a deep understanding of atomic-level interactions occurring in catalytic processes, which can potentially obtain significant improvements in many fields of catalysis. There are many research groups studying size-selected clusters for heterogeneous catalysis. Scott L. Anderson's group has done an intensive study on size-selected Pt clusters on different supports for many reactions [54-56]. For example (Figure 1.4), the catalytic activities of size-selected Pt_n (n = 1 to 14) clusters to ethanol oxidation reaction have been studied [56]. Wolfgang Harbich also did many studies on size-selected Pt clusters for CO oxidation [57, 58]. They found the activity for ethanol oxidation is strongly related to cluster size and anti-correlated with the Pt 4d binding energy. Ulrich Heiz's group is interested in size-selected clusters towards different applications. A thorough study on CO oxidation with different size selected clusters has been done by them [59-61]. Figure 1.5 shows the catalytic activities for CO oxidation on size-selected Au_n, Pt_n,

Pd_n and Rh_n ($n = 8, 13, 20$) clusters. For Au clusters, Au_8 shows the highest activity at both 140K and 240K while Au_{13} , the electronically closed shell cluster, shows the lowest activity; in the case of Pt clusters, the activity increases with the clusters size, and Pt_{20} presents two mechanisms at $\sim 350\text{K}$ and $\sim 500\text{K}$; for Pd and Rh clusters, even the smallest clusters (Pd_8 and Rh_8) can give a considerable activity. Stefan Vajda also has a strong interest on a broad range of size-selected clusters for many oxidation reactions (e.g. Pd_n for cyclohexene oxidation and water oxidation electrocatalysis) [62, 63]. Besides single metal clusters, Ib Chorkendorff's group has done many studies on alloy clusters [64, 65]. Figure 1.6 shows the catalytic activity and stability of mass-selected PtGd clusters for oxygen reduction reaction. The 8 nm clusters present the best activity and stability surpassing the highest activity reached so far with PtY clusters.

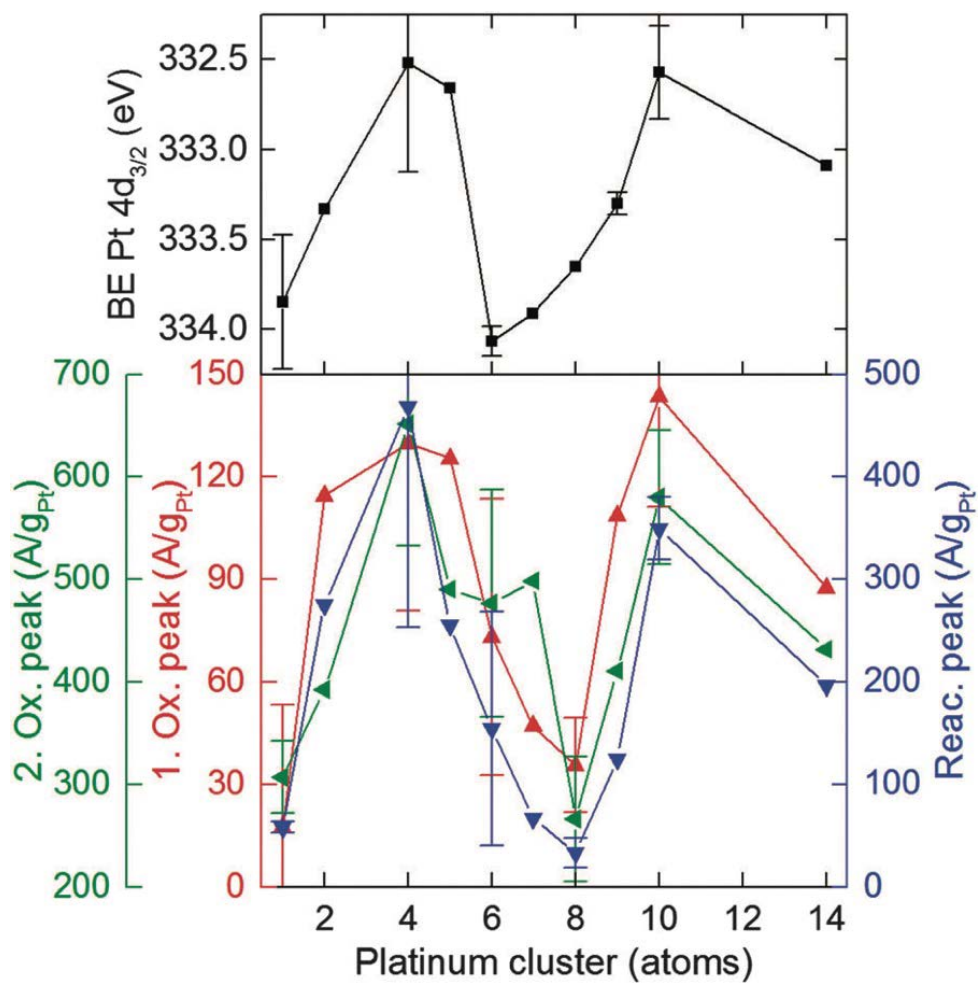


Figure 1.4 Catalytic activities of Pt_n ($n = 1$ to 14) clusters supported on indium tin oxide to ethanol oxidation reaction regarding first oxidation peak (red), second oxidation peak (green) and reactivation peak (blue), reproduced from reference [56]. An anti-correlation between the activity and the Pt $4d_{3/2}$ binding energy (note inverted scale in top graph) was revealed.

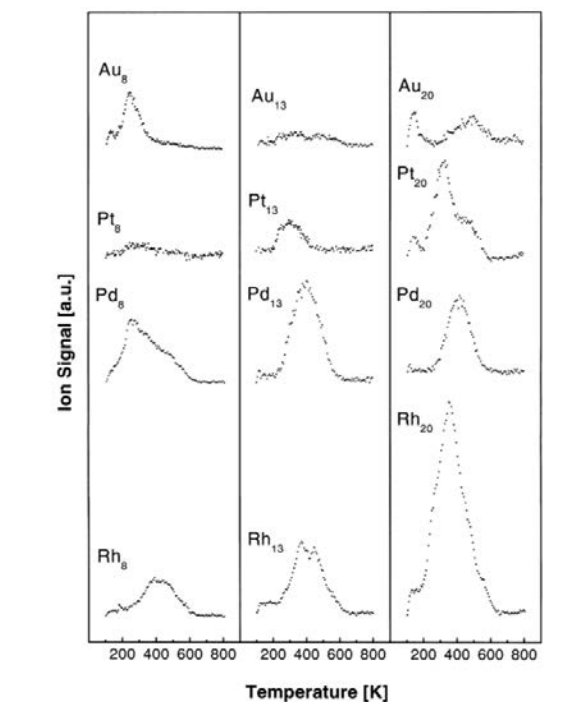


Figure 1.5 CO oxidation on size-selected Au, Pt, Pd and Rh clusters, reproduced from reference [60]. The catalytic activity is strongly size dependent.

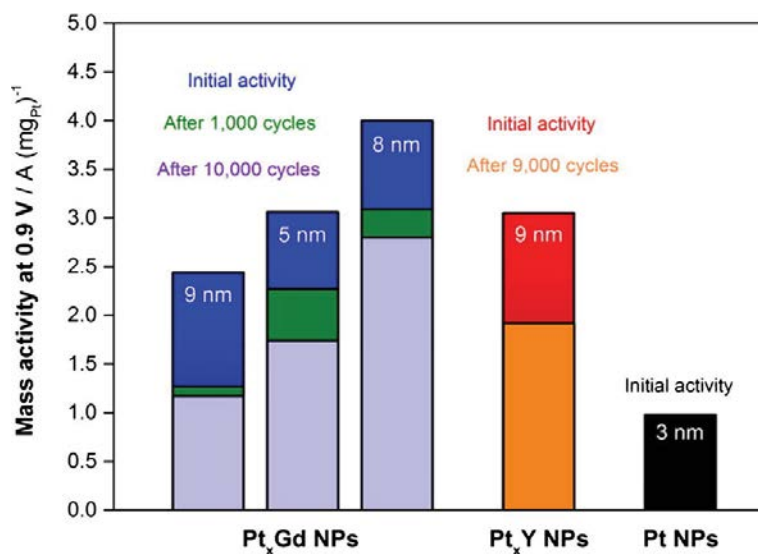


Figure 1.6 The catalytic activity and stability of mass-selected PtGd clusters for oxygen reduction reaction, reproduced from reference [65], which surpasses the highest activity reached so far with PtY clusters. The maximum activity of mass-selected Pt clusters was plotted as the comparison.

1.2.2 Cluster Beam Deposition Techniques

As a clean way of fabricating nanomaterials, cluster beam deposition plays an essential role in the development of nanotechnology in both academia and industry [66]. It has been demonstrated a powerful technique for fundamental studies in physics, material science, chemistry, etc. In addition, with the scale up the cluster production, it has already shown the potential for industry use. For example, the matrix assembly cluster beam source has demonstrated the ability to produce 1 g of catalyst in 1 h [67]. Generally, the cluster beam sources used for cluster beam deposition include seeded supersonic nozzle cluster source, laser ablation cluster source, magnetron sputtering cluster source, pulsed arc discharge cluster source, liquid metal ion source and matrix assembly cluster source.

The basic layout of seeded supersonic nozzle cluster source is shown in Figure 1.7. The metal stored in the high-temperature crucible is heated and forms the atomic vapour, the carrier gas (e.g. He) mixes into the chamber at a high pressure (several times of atmospheric pressure), then the gas-metal mixture goes through a pinhole nozzle into high vacuum via supersonic expansion [14]. Small metal clusters may form before the expansion. The small clusters or atoms will further condense into large clusters by the cooling from the supersonic expansion. The clusters will stop growing when the vapour pressure is not high enough to let collision happen.

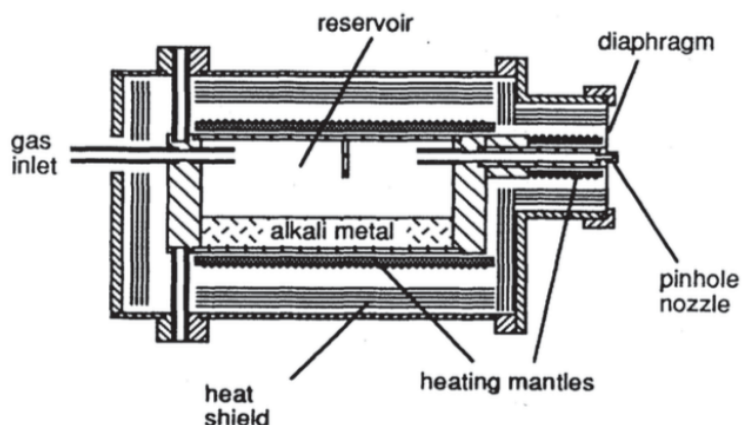


Figure 1.7 Schematic of seeded supersonic nozzle cluster source, reproduced from reference [14]. The atomic vapour formed from the liquid metal in the large crucible mixes with the inert carrier gas and goes through a pinhole nozzle into high vacuum via supersonic expansion.

The seeded supersonic nozzle source is suitable for low melting point materials (e.g. alkali metal), and can produce a cluster beam in order of 10^{18} atoms per second [68]. Normally the size of the cluster from this source is restricted up to several hundred atoms. The size can be moderately tuned by the crucible temperature, nozzle size, carrier gas mass and flow. The clusters generated from this source are neutral. Thus further ionisation device is needed for size-selected clusters.

The laser ablation cluster source, also known as Smalley source, was invented and developed by R. E. Smalley's group in 1980's [69]. Like the seeded supersonic nozzle cluster source, it also introduces atomic vapour and carrier gas shown in Figure 1.8. However, it produces atomic vapour via laser vaporisation and is designed for both metal materials and non-metal materials (e.g. silicon). In contrast with the seeded supersonic nozzle source, the atomic vapour forms from a rather local regime by the focused laser beam. Thus, the atomic vapour can be promptly cooled down by the carrier gas and condensed into clusters. In principle, large clusters

(more than 1000 atoms) can be formed if the vapour can be cooled down effectively. The gas mixture also goes through a supersonic expansion via a nozzle. The size of the clusters is affected by the gas pressure, the residence time in the growth channel, etc.

The laser ablation cluster source has the capability to produce a wide range of materials. Alloy clusters can be fabricated from alloy target or multi-laser ablation. Generally, due to the local vaporisation, the cluster beam flux is lower than that from seeded supersonic nozzle cluster source, but the material consumption is also much lower. An ionisation device is needed for further analysis on clusters.

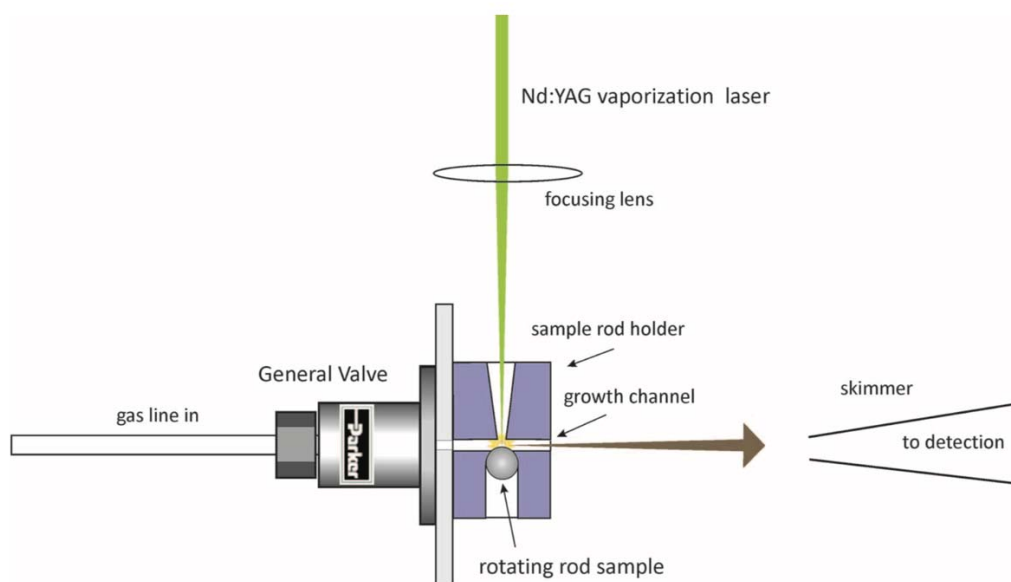


Figure 1.8 Schematic of laser ablation cluster source, reproduced from reference [70]. The atomic vapour is generated via laser vaporisation with high power pulsed laser, cooled down by the carrier gas and condensed into clusters.

Magnetron sputtering cluster source combines plasma sputtering technique and gas condensation technique, which is able to fabricate clusters from metals, semiconductors and insulators [71, 72]. Figure 1.9 illustrates a magnetron sputtering cluster source together with

ion optics and Time-of-Flight mass filter from our group (NPRL). The bulk material is mounted in front of a movable magnetron gun. The condensation length can be controlled by moving the magnetron gun forwards and backwards. During the sputtering, Ar gas is introduced into the chamber from the front of the target and ignited by either DC power or RF power. In the case of DC sputtering, which is designed for conductive materials, a substantial negative bias is applied to the target. The strong electrical field between the target and the Ar^+ plasma will force the Ar^+ ions to bombard the surface of the target. The RF sputtering is designed for all types of materials (conductive, semiconductive, insulating materials). The Ar^+ plasma is ignited by the RF bias and cyclically attracted and repulsed on the target. The atoms in the target will be sputtered out and form atomic vapour. The sputtering rate can be controlled by the sputtering power and Ar gas flow. High power and large Ar flux can generate dense atomic vapour, which is favourable for forming the large cluster. The gas condensation happens in the same chamber via three body collisions when the inert gas He is introduced. Meanwhile, the whole chamber is cooled by liquid nitrogen helping to efficiently remove the extra kinetic energies in the three body collisions. Since the sputtering discharge can ionise a large percentage (30% - 80%) of the clusters, no further ionisation device is needed [73]. The clusters leave the sputtering chamber via supersonic expansion into the next chamber. More details on ion optics and mass filter are discussed in Chapter 2.

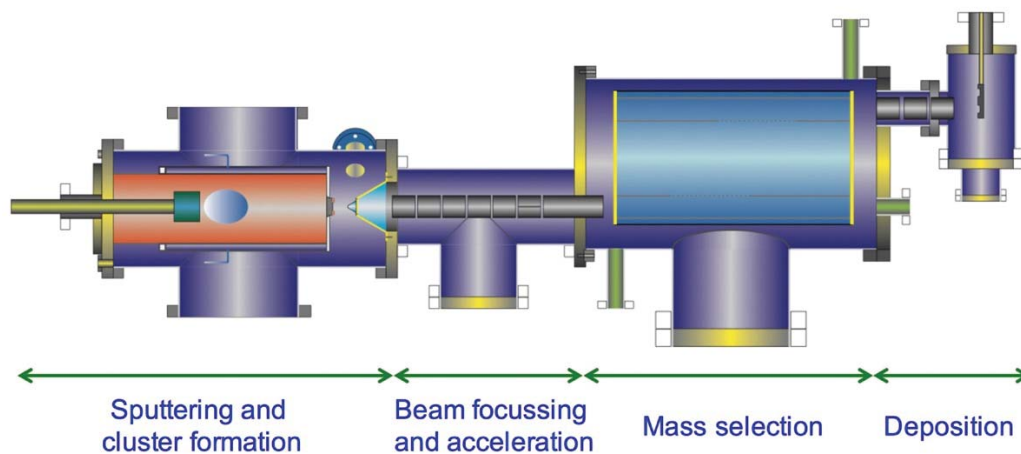


Figure 1.9 Schematic illustration of the size selected cluster beam source in NPRL, which combines the magnetron sputtering technique and gas condensation technique. Ar gas and He gas are introduced for plasma sputtering and gas condensation, respectively.

The magnetron sputtering cluster source can produce high-density cluster beam from a wide range of materials. The clusters can be formed with a size up to $\sim 10^5$ atoms, and their size can be tuned by many parameters (gas flow, sputtering power, condensation length, etc.). Like laser ablation cluster source, alloy clusters can be fabricated from alloy targets or multi-magnetron sputtering.

The pulsed arc discharge clusters source has been taken as a replacement of the laser ablation cluster source [74, 75]. The configuration of the pulsed arc discharged cluster source (Figure 1.10) is similar to the laser ablation cluster source. Instead of using a pulsed laser, a discharge between the cathode and anode with high discharging current up to 10^5 A is applied to generate metal plasma. The metal plasma is then cooled down by the carrier gas and aggregates into clusters with a high ionisation yield ($\sim 10\%$). A high cluster deposition rate (e.g. up to 2 Angstrom per pulse for lead) can be achieved [76].

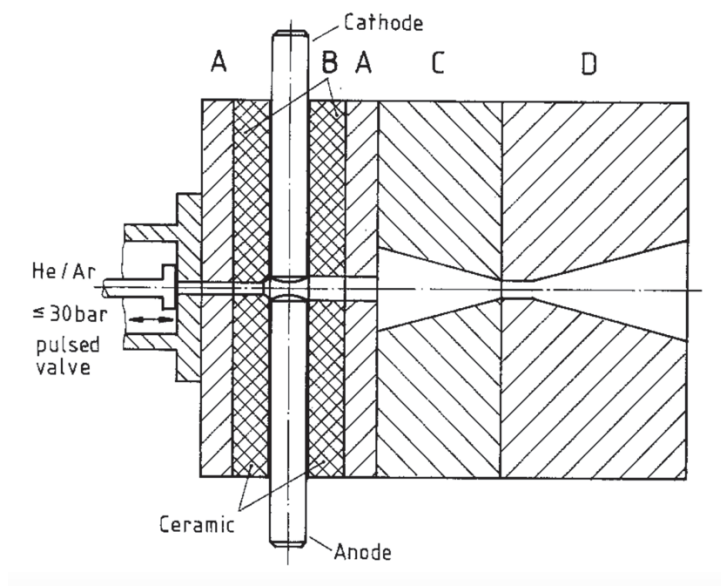


Figure 1.10 Schematic of the pulsed arc discharge cluster source, reproduced from reference [74]. A pulsed high-current arc is fired between the cathode and the anode in a stream of carrier gas, the metal plasma is then cooled down and aggregates into clusters.

The liquid metal ion source produces an ion beam from the apex of a liquid metal Taylor cone shown in Figure 1.11. A strong electrical field (normally few kV) is applied between the needle tip and the accelerator electrode. A low melting point metal is liquefied and introduced on to the needle tip by a liquid metal reservoir. As the liquid metal approaches the needle tip, the charge density becomes high enough to spray off the metal. Ionised clusters can be provided by this source, but the clusters have a comprehensive energy distribution due to the formation mechanism [77, 78]. Because of the absence of the cooling medium, the formed clusters contain incredibly high kinetic energy, which stops the clusters to grow into large ones. Although there are many limitations with the liquid metal ion source, it is still a useful method producing metal ions.

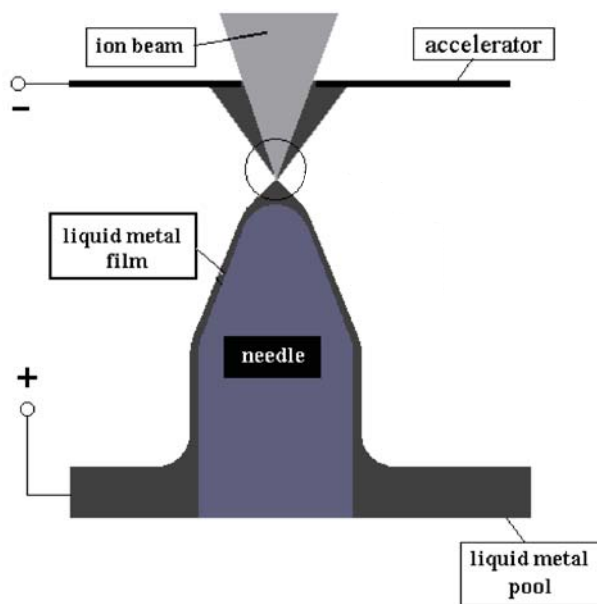


Figure 1.11 Schematic of the liquid metal cluster source, reproduced from reference [79]. The liquid metal under a strong electric field adopts a conical shape (Taylor cone) and emits ion beam.

The matrix assembly cluster source was recently developed in NPRL and aims to address the low flux problem with the conventional cluster sources discussed above. The principle of the matrix assembly cluster source is illustrated in Figure 1.12. Firstly, the metal vapour generated from the evaporator is condensed with the Ar gas onto a cryogenically cooled support (~ 20 K, with a continuous flow of liquid He). The metal atoms will be embedded into the solid Ar gas matrix. Subsequently, the matrix is sputtered with Ar ions. The released metal atoms will nucleate into clusters via collisions. Prior to the Ar ion sputtering, small clusters may also form in the matrix via diffusion. The production of size-controlled clusters from the conventional cluster sources is at $\mu\text{g/h}$ magnitude. The matrix assembly cluster source is able to increase the cluster production to mg/h magnitude, which can meet the industrial R&D scale.

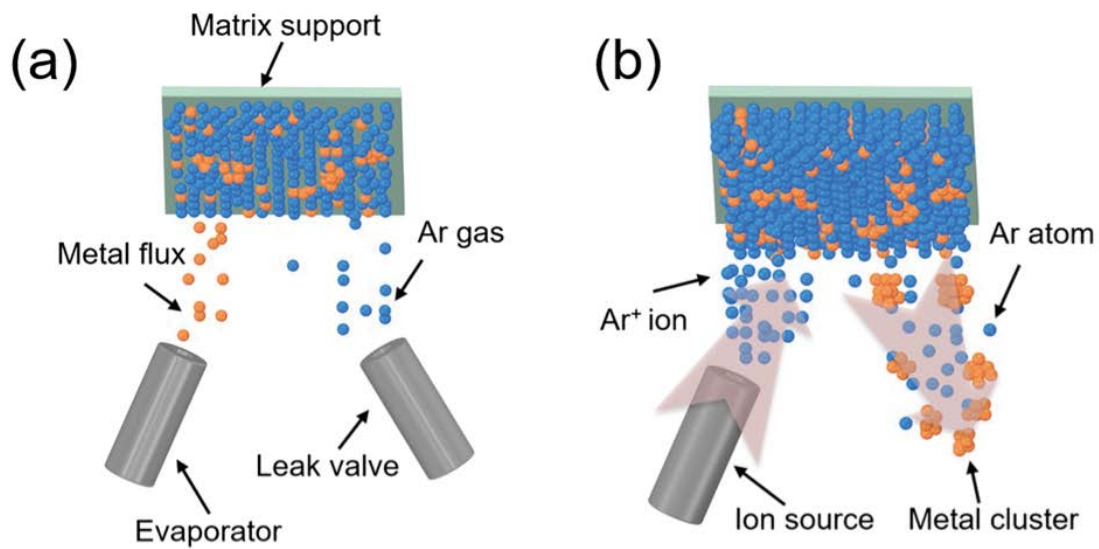


Figure 1.12 Schematic of the principle of the matrix assembly cluster source, reproduced from reference [80]. The vaporised metal and Ar gas are simultaneously condensed onto a cryogenically cooled surface to form a metal-Ar matrix (a), then the matrix is sputtered by an Ar ion beam to release the metal and form clusters.

There is already a pioneer in the field of high flux cluster source before the development of the matrix cluster source. The micro plasma cluster source, developed in Paolo Milani's group, combines the micro plasma sputtering and aerodynamic focusing [81]. A deposition rate of 5 nm/min can be reached by this source [82]. The typical cluster size, cluster beam flux and tuning parameters for cluster size for different cluster beam sources are summarised in Table 1.1.

Table 1.1 Summary of cluster beam sources.

Cluster beam source	Cluster size	Cluster beam flux	Affecting factors of cluster size
Seeded supersonic nozzle cluster source	Up to several hundred atoms	Up to 10^{18} atoms/s	Crucible temperature, nozzle size, carrier gas mass and flow
Laser ablation cluster source	Up to ~1000 atoms	Up to $\sim 10^{17}$ atoms/s	Pressure of the carrier gas, duration of the gas pulse, delay times between the gas valve opening and the ablation laser pulse
Magnetron sputtering cluster source	Up to 10^5 atoms	Maximum beam current of size selected cluster is up to several nano amps	Carrier gas pressure, carrier gas temperature, carrier gas flow, carrier gas mass, sputtering power and aggregation region length
Pulsed arc discharge cluster source	Up to ~1000 atoms	Deposition rate up to 2 Angstrom per pulse	Discharge power, carrier gas pulse length and carrier gas flow
Liquid metal ion source	Up to ~100 atoms	several tens of nano amps	Emission currents from the tip
Matrix assembly cluster source	Up to several thousand atoms	A cluster beam flux equivalent to 10 μ A	Metal concentration in the matrix

1.2.3 Catalysis in Energy and Environment

Due to the rocketing development of humanity, the global energy consumption keeps increasing and has no hint to turn down (Figure 1.13). Around 85% of the total energy consumption is based on oil, coal and natural gas (Figure 1.14), although the renewable energy has reached a record high (but still only 3.6%). Given that fossil fuel resources are being depleted at a much faster rate than they are formed, and there are great concerns regarding the influence of CO₂ emissions on the global climate [83, 84], hydrogen energy is listed as a top candidate to meet the already enormous and still increasing energy demand in the world. Hydrogen is the lightest element with an impressive energy yield around 122 kJ/g, which is ~3 times higher than hydrocarbon fuels [85]. As a clean fuel without toxic emissions, hydrogen can be used (i) to make conventional synthetic fuels (e.g. methane, methanol, gasoline), (ii) mixed with natural gas lines to dilute and increase the quality of the fossil fuel gas, or (iii) stored for use in fuel cells or power generators. However, the vast majority of the hydrogen production is produced from steam reforming of natural gas [86-88], eco-friendly technology

is needed to conduct a turnaround. Electrochemical water splitting has been regarded as the most promising technology to address this challenge and make “water as the coal of the future” [89-91].

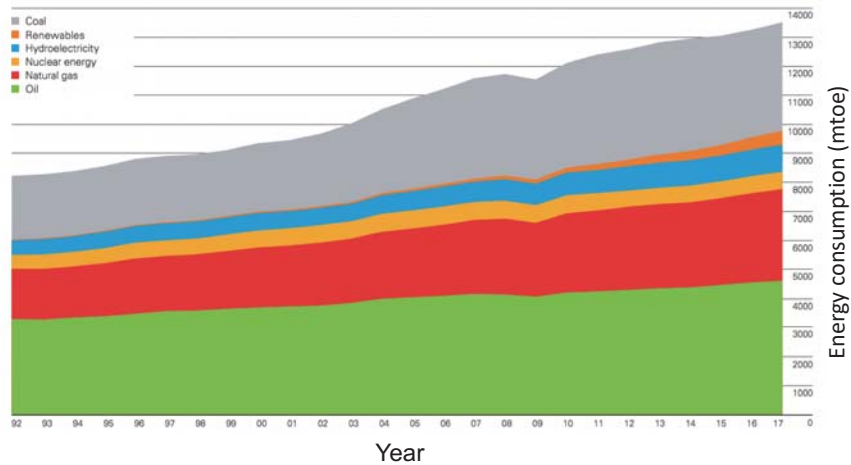


Figure 1.13 Global primary energy consumption from 1992 to 2017 in million tons oil equivalent (mtoe), reproduced from reference [92]. The total consumption keeps increasing and has no hint to turn down.

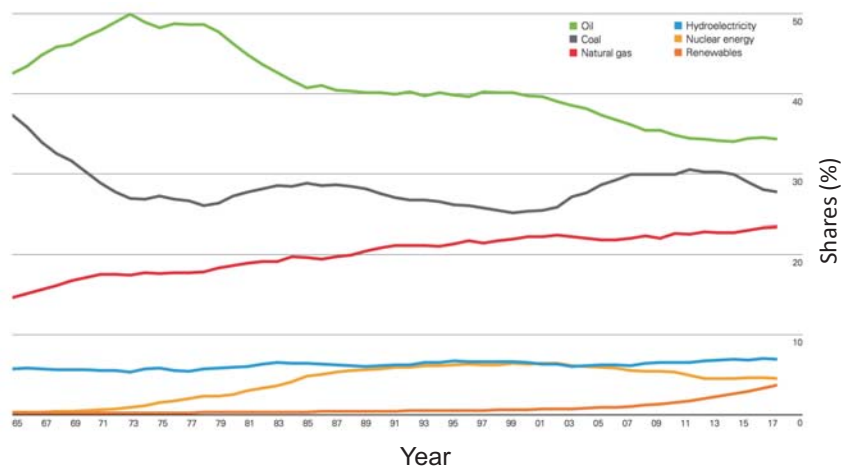


Figure 1.14 Shares of global primary energy consumption from 1965 to 2017, reproduced from reference [92]. In 2017, ~85% of the total energy is supplied by oil, coal and natural gas. The renewable energy reaches a new high but is only 3.6% of the total energy.

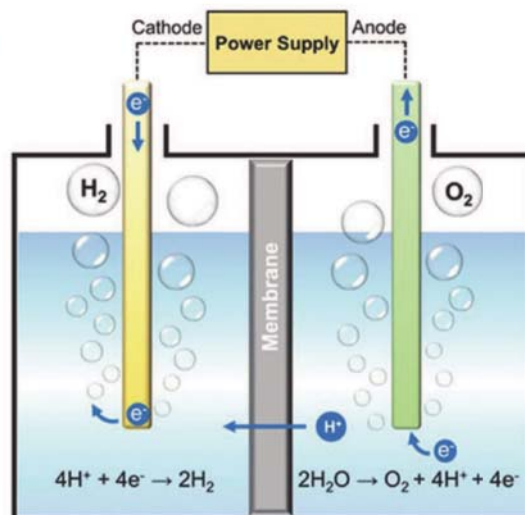


Figure 1.15 Schematic of electrochemical water splitting including hydrogen evolution reaction (HER) on the left and oxygen evolution reaction (OER) on the right, reproduced from reference [93].

The water splitting process (Figure 1.15) includes hydrogen evolution reaction (HER) and oxygen evolution reaction (OER), which can be considered as a reverse reaction of H_2 combustion [93]. The HER plays an important role responsible for hydrogen production in the presence of suitable catalysts. However, platinum group metals including Pt, Pd, Ir, Rh and Ru are essential components of these catalysts; these “critical metals” are expensive and scarce [94]. Recently, transition metal dichalcogenides (TMD), such as layered crystalline materials with interlayer van der Waals bonding, are once more attracting great attention both in academia and industry due to their unique physical and chemical properties [95-97]. Molybdenum disulphide (MoS_2), as a representative member of the TMD family, has been widely investigated with respect to its catalytic properties [98, 99]. MoS_2 layer has a sandwich structure (illustrated in Figure 1.16) with molybdenum atoms in a layer between two sulphur sheets [100, 101]. It has been proved the edge sites, rather than the basal atoms, that mainly contribute to the catalytic activity of nanostructured MoS_2 [102, 103]. More than that, there are

two types of edge site in crystalline MoS₂: Mo-edge and S-edge. It turned out that only the low coordinated sulphur atoms at Mo-edge sites are active, at which the free energy of atomic hydrogen adsorption is pretty close to zero, while the sulphur atoms at S-edge are catalytically inert [104-107]. Thus, nanostructured MoS₂ with an abundance of edges remains a highly rated prospect as a substitution of scarce and costly platinum in HER [102].

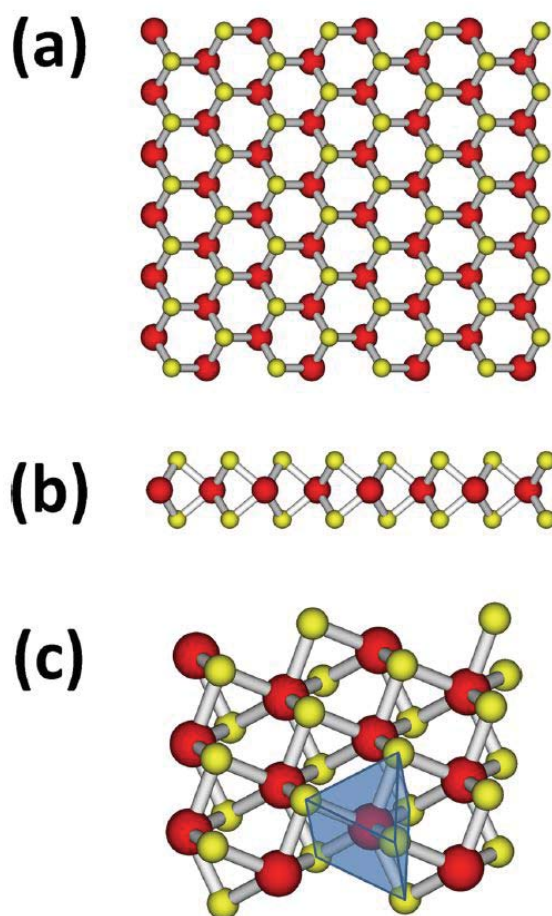


Figure 1.16 Top view (a), side view (b), and oblique view (c) the sandwich structure of MoS₂ monolayer with molybdenum atoms in a layer between two sulphur sheets. The Mo and S atoms are represented as red and yellow balls, respectively. The schematic is reproduced from reference [101].

Many methods (e.g. sulfidation of MoO₃ or Mo) have been utilised to produce nano MoS₂ [28,

108, 109]. The previous research on MoS₂ electrocatalysis has given an insight into the catalytic mechanism and active sites at the atomic scale. In this thesis, we explored the way to optimise and enhance the active sites of MoS₂ clusters for HER. Size-controlled and size-selected MoS₂ clusters are produced by the cluster beam deposition technique, which is a simple and clean manufacture method of nano MoS₂ fabrication.

1.2.4 Au Nanocatalysis and Sintering

Au nanoparticles represent the most remarkable example of a size effect in heterogeneous catalysis. However, A major issue hindering the use of Au nanoparticles in technological applications is their rapid sintering [110, 111]. Au is considered to be the noblest of all metals, long regarded as chemically inert [112], and thus (more or less) catalytically inactive. Nevertheless a report from as long ago as 1906 states that a hot Au mesh can facilitate the combination of O₂ and H₂ [113], while a paper from 1925 indicates that Au is capable of catalysing the oxidation of CO to CO₂ [114]. But since Au is relatively expensive, and the reported reaction rates were lower compared with other metals, Au was not considered as a viable catalyst until Sennewald et al. [115] found that a Pd-Au catalyst was active for the oxidative acetoxylation of ethylene to vinyl acetate in 1965 and then Bond and Sermon [116] demonstrated the activity of supported Au particles with diameters of 2-100 nm for the hydrogenation of 1-pentene at 100°C in 1973. Later, in the 1980's, Haruta et al. [117, 118] discovered that Au nanoparticles, with diameters of 3-5 nm hold up on reducible supports, were exceptionally active for CO oxidation even at -70°C, and Hutchings [119] demonstrated the catalytic activity of Au³⁺ in the hydrochlorination of acetylene to vinyl chloride. Since then, Au has attracted growing attention as a catalyst and become the preeminent example of a size effect in heterogeneous catalysis [17, 120, 121]. This short review on Au-based nanocatalysis is reproduced from the introduction of my published work of "Reduced sintering of mass-

selected Au clusters on SiO₂ by alloying with Ti: an aberration-corrected STEM and computational study” [122].

CO oxidation, as one of the best-known elementary reactions in heterogeneous catalysis, is one of the most straightforward reactions which Au nanoparticles can catalyse [123-125]. In addition, CO oxidation is frequently used as a probe reaction in surface science [126]. CO oxidation on TiO₂ supported Au nanoparticles has become a prototypical model system in Au catalysis [127-130]. Numerous studies have been reported regarding the reaction mechanisms [131-133], active sites [17, 134-136], and active species [137, 138]. Figure 1.17 illustrates the impact of Au particle size on catalytic activities for CO oxidation from experimental data [17]. It can be clearly seen that the catalytic activity has a strong dependence on the size of Au particle size, and only the Au particles with diameters below 5 nm are active. In addition, it can also be seen that support materials play an important role in the activities. For example, Au particle (< 5 nm) is highly active on TiO₂, but nearly non-active on SiO₂. The explanation behind this size effect has been the subject of extreme controversy. One generally agreed explanation is that the smaller size Au particle provides more low-coordinated Au atoms, and the catalytic activity is highly dependent on the fraction of low-coordinated Au atoms. This suggests that the active sites for CO oxidation are the atoms on the corners and edges of Au nanoparticles, which has been confirmed by density functional calculations [17]. Regarding the Au species, different researchers have different finds. It could be positively charged, negatively charged or metallic Au nanoparticles that contribute to the activity for CO oxidation, and there is no clear conclusion [137].

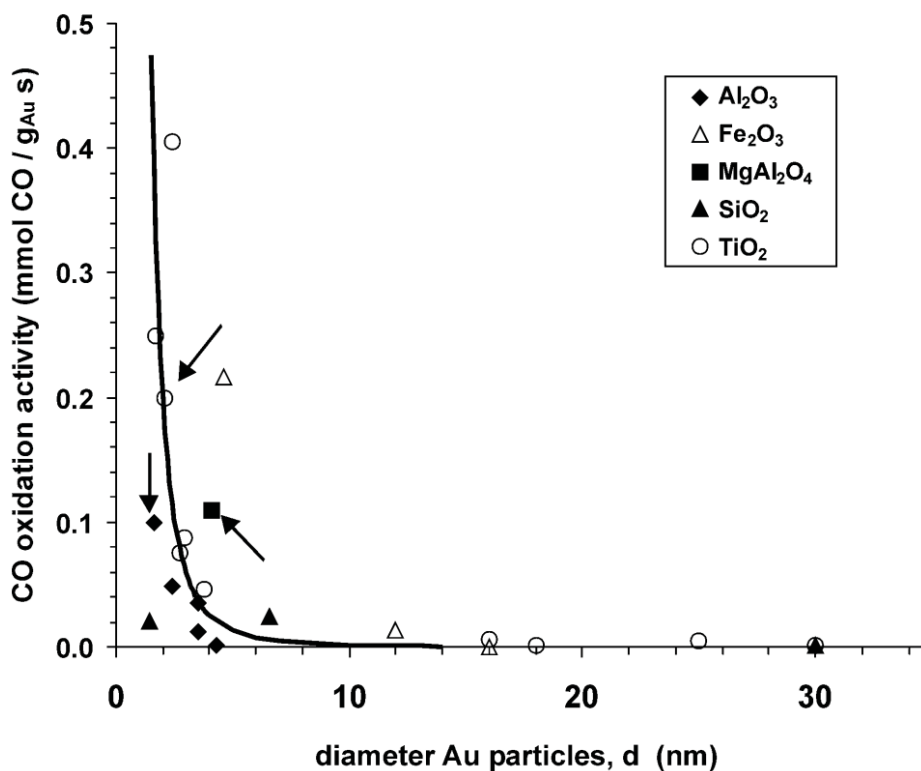


Figure 1.17 Catalytic activities of Au particle for CO oxidation as a function of Au particle size at 273K on different support materials, reproduced from reference [17, 139].

There is a general agreement that the elementary steps for CO oxidation include adsorption and desorption of CO and O₂, O₂ dissociation, surface migration of O_{ad} and CO_{ad}, and formation of possible transient intermediates like carbonates [140]. The formation of active oxygen from the dissociation of O₂ plays a vital role among these steps. It is the most energy consuming step due to a considerable binding energy of 498 kJ mol⁻¹ with O₂ [130]. It has been shown that adsorbed O₂ can be the active species for CO oxidation at low temperatures. However, adsorbed O₂ is not stable and there is much less clear for the nature of active oxygen species under standard conditions [141]. There are few proposed reaction mechanisms for CO oxidation over supported Au nanoparticles illustrated in Figure 1.18 [131]. All these mechanisms assume that CO pre-adsorbs on the surface of Au nanoparticles, while the active

oxygen sites originate from different places. Figure 1.18A is “Au only mechanism” with either molecularly or atomically adsorbed oxygen as active oxygen species [142]. Figure 1.18B and 1.18C show the “interface mechanism” active oxygen located at perimeter sites or surface vacancies close to perimeter sites [141, 143]. In Figure 1.18D, the surface lattice oxygen from support acts as active oxygen [144]. The first three mechanisms belong to Langmuir-Hinshelwood type mechanism, while the last one corresponds to a Mars-van Krevelen type mechanism, in which the surface lattice oxygen reacts with CO first, and then the reduced support surface is reoxidised by gas-phase oxygen.

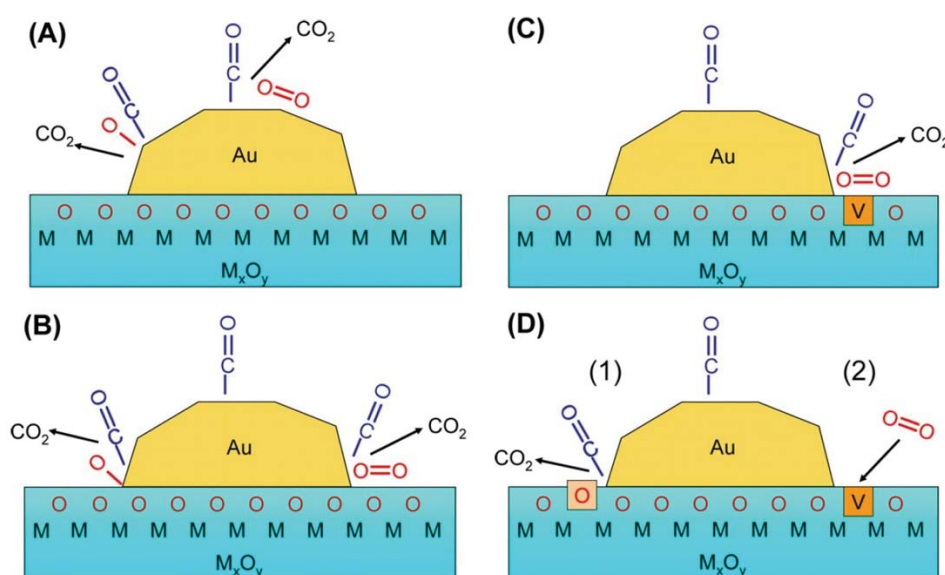


Figure 1.18 Schematic illustrations of the possible reaction mechanisms for CO oxidation on supported Au nanoparticles, reproduced from reference [131].

Although Au nanoparticles have been proved to be excellent catalysts for CO oxidation, they suffer from deactivation attributed to either sintering of Au nanoparticles or poisoning of active sites by the accumulation of byproducts. The latter cause for deactivation is reversible, and Au

nanoparticles can liberate their surfaces by CO₂ evolution with heating, while sintering is irreversible and the Au nanoparticles will lose their catalytic activities once sintering happens. In this thesis, we utilise the size-selected Au cluster and Au/Ti alloy cluster to demonstrate a method against sintering.

1.3 Thesis Overview

This thesis demonstrates the capability of nanocluster beam deposition technique in the production of binary clusters and explores the catalytic activities of those nanoclusters for electrochemistry and heterogeneous catalysis. The cluster beam deposition utilised in the research is based on the magnetron sputtering, gas condensation technique. MoS₂-based clusters and Au-based clusters have been demonstrated for electrochemistry (HER) and gas phase heterogeneous catalysis (CO oxidation), respectively.

Theoretical calculations have predicted a promising way to dramatically improve the catalytic activity of nano MoS₂ to HER by doping the S-edge sites of MoS₂ with transition metal (TM) (Fe, Co, Ni). In order to validate this hypothesis, we explore the catalytic activity of Ni-MoS₂ in chapter 3 as a representation of TM-doped MoS₂ clusters prepared via a dual-magnetron sputtering cluster beam source. In this chapter, pristine MoS₂ clusters, Ni clusters and Ni-MoS₂ hybrid clusters are prepared to evaluate their electrocatalytic activity to HER. All the MoS₂ clusters produced from cluster beam deposition have a sulphur-deficient nature with stoichiometry MoS_{2-x}. Chapter 4 provides an in vacuum processing approach to increase the sulphur content of the clusters. The atomic structure modification and catalytic activities of the sulphur-enriched MoS₂ clusters have been studied.

Au nanoparticles have proved to be good catalysts with genuine potential in technological applications, however, a major issue hindering their implementation is their rapid sintering. Chapter 5 demonstrates a method of reducing the sintering of Au clusters in Au-based catalysis

by exploring the stabilisation of supported Au clusters against sintering by alloying with Ti. The sintering behaviours of size-selected Au clusters and Au/Ti nanoalloy clusters have been studied by aberration-corrected scanning transmission electron microscope imaging in real space and real time. The strong anchoring effect found in the case of Au/Ti clusters may open up new possibilities in Au-based nanocatalysis.

References

- [1] Echt O, Sattler K, Recknagel E. Magic numbers for sphere packings: experimental verification in free xenon clusters. *Phys. Rev. Lett.* **1981**, 47(16): 1121-1124.
- [2] Knight WD, Clemenger K, Deheer WA, Saunders WA, Chou MY, Cohen ML. Electronic shell structure and abundances of sodium clusters. *Phys. Rev. Lett.* **1984**, 52(24): 2141-2143.
- [3] Sakurai M, Watanabe K, Sumiyama K, Suzuki K. Magic numbers in transition metal (Fe, Ti, Zr, Nb, and Ta) clusters observed by time-of-flight mass spectrometry. *The Journal of Chemical Physics* **1999**, 111(1): 235-238.
- [4] Li ZY, Young NP, Di Vece M, Palomba S, Palmer RE, Bleloch AL, *et al.* Three-dimensional atomic-scale structure of size-selected gold nanoclusters. *Nature* **2008**, 451(7174): 46-48.
- [5] Pyykko P. Structural properties - magic nanoclusters of gold. *Nature Nanotechnology* **2007**, 2(5): 273-274.
- [6] Gruene P, Rayner DM, Redlich B, van der Meer AFG, Lyon JT, Meijer G, *et al.* Structures of neutral Au₇, Au₁₉, and Au₂₀ clusters in the gas phase. *Science* **2008**, 321(5889): 674-676.
- [7] Binnig G, Rohrer H, Gerber C, Weibel E. Surface studies by scanning tunneling microscopy. *Phys. Rev. Lett.* **1982**, 49(1): 57-61.
- [8] Liu HY, Fan FRF, Lin CW, Bard AJ. Scanning electrochemical and tunneling ultramicroelectrode microscope for high-resolution examination of electrode surfaces in solution. *J. Am. Chem. Soc.* **1986**, 108(13): 3838-3839.
- [9] Reetz MT, Helbig W, Quaiser SA, Stimming U, Breuer N, Vogel R. Visualization of surfactants on nanostructured palladium clusters by a combination of STM and high-resolution TEM. *Science* **1995**, 267(5196): 367-369.

- [10] Pfisterer JHK, Liang YC, Schneider O, Bandarenka AS. Direct instrumental identification of catalytically active surface sites. *Nature* **2017**, 549(7670): 74.
- [11] Ekardt W. Dynamical polarizability of small metal particles: self-consistent spherical jellium background model. *Phys. Rev. Lett.* **1984**, 52(21): 1925-1928.
- [12] Jarrold MF. Nanosurface chemistry on size-selected silicon clusters. *Science* **1991**, 252(5009): 1085-1092.
- [13] Johnston RL. Atomic and molecular clusters. *CRC Press, London* **2002**.
- [14] Deheer WA. The physics of simple metal clusters: experimental aspects and simple models. *Reviews of Modern Physics* **1993**, 65(3): 611-676.
- [15] Haruta M. When gold is not noble: Catalysis by nanoparticles. *Chem Rec* **2003**, 3(2): 75-87.
- [16] Johnston RL. Metal nanoparticles and nanoalloys. *Frontiers of Nanoscience (Elsevier)* **2012**, 3: 1-42.
- [17] Hvolbæk B, Janssens TVW, Clausen BS, Falsig H, Christensen CH, Nørskov JK. Catalytic activity of au nanoparticles. *Nano Today* **2007**, 2(4): 14-18.
- [18] Fenwick O, Coutino-Gonzalez E, Grandjean D, Baekelant W, Richard F, Bonacchi S, *et al.* Tuning the energetics and tailoring the optical properties of silver clusters confined in zeolites. *Nature Materials* **2016**, 15(9): 1017-1022.
- [19] Alonso JA. Structure and properties of atomic nanoclusters. *World Scientific, London* **2012**.
- [20] Qian HF, Zhu MZ, Wu ZK, Jin RC. Quantum sized gold nanoclusters with atomic precision. *Acc. Chem. Res.* **2012**, 45(9): 1470-1479.
- [21] Ertl G, Knözinger H, Schüth F, Weitkamp J. Handbook of heterogeneous catalysis. *Weinheim: Wiley-VCH* **1997**.

- [22] Yang F, Deng DH, Pan XL, Fu Q, Bao XH. Understanding nano effects in catalysis. *National Science Review* **2015**, 2(2): 183-201.
- [23] Chorkendorff I NJ. Concepts of modern catalysis and kinetics. *John Wiley & Sons* **2017**.
- [24] Polshettiwar V, Varma RS. Green chemistry by nano-catalysis. *Green Chemistry* **2010**, 12(5): 743.
- [25] Zhang XY, Fevre M, Jones GO, Waymouth RM. Catalysis as an enabling science for sustainable polymers. *Chem. Rev.* **2018**, 118(2): 839-885.
- [26] Liu YX, Zhao GF, Wang DS, Li YD. Heterogeneous catalysis for green chemistry based on nanocrystals. *National Science Review* **2015**, 2(2): 150-166.
- [27] McNaught AD WA. Compendium of chemical terminology. *Oxford: Blackwell Science* **1997**.
- [28] Coperet C, Chabanas M, Saint-Arroman RP, Basset JM. Homogeneous and heterogeneous catalysis: Bridging the gap through surface organometallic chemistry. *Angewandte Chemie-International Edition* **2003**, 42(2): 156-181.
- [29] Falivene L, Kozlov SM, Cavallo L. Constructing bridges between computational tools in heterogeneous and homogeneous catalysis. *Acs Catalysis* **2018**, 8(6): 5637-5656.
- [30] Ertl G. Reactions at well-defined surfaces. *Surf. Sci.* **1994**, 299(1-3): 742-754.
- [31] Taylor HS. A theory of the catalytic surface. *Proceedings of the Royal Society A: Mathematical, Physical and Engineering Sciences* **1925**, 108(745): 105-111.
- [32] Bell AT. The impact of nanoscience on heterogeneous catalysis. *Science* **2003**, 299(5613): 1688-1691.
- [33] Lee S, Molina LM, Lopez MJ, Alonso JA, Hammer B, Lee B, *et al.* Selective propene epoxidation on immobilized Au₆₋₁₀ clusters: The effect of hydrogen and water on activity and selectivity. *Angewandte Chemie-International Edition* **2009**, 48(8): 1467-1471.

- [34] Hayashi T, Tanaka K, Haruta M. Selective vapor-phase epoxidation of propylene over Au/TiO₂ catalysts in the presence of oxygen and hydrogen. *J. Catal.* **1998**, 178(2): 566-575.
- [35] Tyo EC, Vajda S. Catalysis by clusters with precise numbers of atoms. *Nat Nanotechnol* **2015**, 10(7): 577-588.
- [36] Kappes MM, Kunz RW, Schumacher E. Production of large sodium clusters (Na_x, x < 65) by seeded beam expansions. *Chem. Phys. Lett.* **1982**, 91(6): 413-418.
- [37] Kappes MM, Radi P, Schar M, Schumacher E. Probes for electronic and geometrical shell structure effects in alkali-metal clusters - photoionization measurements on K_xLi, K_xMg and K_xZn (x < 25). *Chem. Phys. Lett.* **1985**, 119(1): 11-16.
- [38] Bergeron DE, Castleman AW, Morisato T, Khanna SN. Formation of Al₁₃I⁻: evidence for the superhalogen character of Al₁₃. *Science* **2004**, 304(5667): 84-87.
- [39] Smolanoff J, Lapicki A, Anderson SL. Use of a quadrupole mass filter for high energy resolution ion beam production. *Rev. Sci. Instrum.* **1995**, 66(6): 3706-3708.
- [40] Bohme DK, Schwarz H. Gas phase catalysis by atomic and cluster metal ions: the ultimate single-site catalysts. *Angewandte Chemie-International Edition* **2005**, 44(16): 2336-2354.
- [41] Schroder D, Schwarz H. C-H and C-C bond activation by bare transition-metal oxide cations in the gas phase. *Angewandte Chemie-International Edition in English* **1995**, 34(18): 1973-1995.
- [42] Lang SM, Bernhardt TM, Barnett RN, Yoon B, Landman U. Hydrogen-promoted oxygen activation by free gold cluster cations. *J. Am. Chem. Soc.* **2009**, 131(25): 8939-8951.
- [43] Castleman AW, Jr. Cluster structure and reactions: gaining insights into catalytic processes. *Catal. Lett.* **2011**, 141(9): 1243-1253.

- [44] Schwarz H. Chemistry with methane: concepts rather than recipes. *Angewandte Chemie-International Edition* **2011**, 50(43): 10096-10115.
- [45] Tyo EC, Vajda S. Catalysis by clusters with precise numbers of atoms. *Nature Nanotechnology* **2015**, 10(7): 577-588.
- [46] Liu LC, Corma A. Metal catalysts for heterogeneous catalysis: from single atoms to nanoclusters and nanoparticles. *Chem. Rev.* **2018**, 118(10): 4981-5079.
- [47] Palmer RE, Pratontep S, Boyen HG. Nanostructured surfaces from size-selected clusters. *Nature Materials* **2003**, 2(7): 443-448.
- [48] Peters S, Peredkov S, Balkaya B, Ferretti N, Savci A, Vollmer A, *et al.* Inner-shell photoionization spectroscopy on deposited metal clusters using soft X-ray synchrotron radiation: an experimental setup. *Rev. Sci. Instrum.* **2009**, 80(12).
- [49] Lim DC, Hwang CC, Gantfoer G, Kim YD. Model catalysts of supported Au nanoparticles and mass-selected clusters. *Phys. Chem. Chem. Phys.* **2010**, 12(46): 15172-15180.
- [50] Popok VN, Barke I, Campbell EEB, Meiwes-Broer KH. Cluster-surface interaction: from soft landing to implantation. *Surf. Sci. Rep.* **2011**, 66(10): 347-377.
- [51] Pearmain D, Park SJ, Wang ZW, Abdela A, Palmer RE, Li ZY. Size and shape of industrial Pd catalyst particles using size-selected clusters as mass standards. *Appl. Phys. Lett.* **2013**, 102(16).
- [52] Lucci FR, Liu JL, Marcinkowski MD, Yang M, Allard LF, Flytzani-Stephanopoulos M, *et al.* Selective hydrogenation of 1,3-butadiene on platinum-copper alloys at the single-atom limit. *Nat. Commun.* **2015**, 6.
- [53] Tokonami S, Morita N, Takasaki K, Toshima N. Novel synthesis, structure, and oxidation catalysis of Ag/Au bimetallic nanoparticles. *Journal of Physical Chemistry C* **2010**, 114(23): 10336-10341.

- [54] Von Weber A, Baxter ET, White HS, Anderson SL. Cluster size controls branching between water and hydrogen peroxide production in electrochemical oxygen reduction at Pt_n/ITO. *Journal of Physical Chemistry C* **2015**, 119(20): 11160-11170.
- [55] Roberts FS, Kane MD, Baxter ET, Anderson SL. Oxygen activation and co oxidation over size-selected Pt_n/alumina/Re(0001) model catalysts: correlations with valence electronic structure, physical structure, and binding sites. *Phys. Chem. Chem. Phys.* **2014**, 16(48): 26443-26457.
- [56] Von Weber A, Baxter ET, Proch S, Kane MD, Rosenfelder M, White HS, *et al.* Size-dependent electronic structure controls activity for ethanol electro-oxidation at Pt_n/indium tin oxide (n = 1 to 14). *Phys. Chem. Chem. Phys.* **2015**, 17(27): 17601-17610.
- [57] Bonanni S, Ait-Mansour K, Harbich W, Brune H. Reaction-induced cluster ripening and initial size-dependent reaction rates for CO oxidation on Pt_n/TiO₂(110)-(1x1). *J. Am. Chem. Soc.* **2014**, 136(24): 8702-8707.
- [58] Bonanni S, Ait-Mansour K, Harbich W, Brune H. Effect of the TiO₂ reduction state on the catalytic CO oxidation on deposited size-selected Pt clusters. *J. Am. Chem. Soc.* **2012**, 134(7): 3445-3450.
- [59] Tang X, Schneider J, Dollinger A, Luo Y, Worz AS, Judai K, *et al.* Very small "window of opportunity" for generating co oxidation-active Au_n on TiO₂. *Phys. Chem. Chem. Phys.* **2014**, 16(14): 6735-6742.
- [60] Heiz U, Sanchez A, Abbet S, Schneider WD. Tuning the oxidation of carbon monoxide using nanoassembled model catalysts. *Chem. Phys.* **2000**, 262(1): 189-200.
- [61] Heiz U, Sanchez A, Abbet S, Schneider WD. Catalytic oxidation of carbon monoxide on monodispersed platinum clusters: each atom counts. *J. Am. Chem. Soc.* **1999**, 121(13): 3214-3217.

- [62] Kwon G, Ferguson GA, Heard CJ, Tyo EC, Yin CR, DeBartolo J, *et al.* Size-dependent subnanometer pd cluster (Pd₄, Pd₆, and Pd₁₇) water oxidation electrocatalysis. *Acs Nano* **2013**, 7(7): 5808-5817.
- [63] Habibpour V, Yin CR, Kwon G, Vajda S, Palmer RE. Catalytic oxidation of cyclohexane by size-selected palladium clusters pinned on graphite. *J. Exp. Nanosci.* **2013**, 8(7-8): 993-1003.
- [64] Holse C, Elkjaer CF, Nierhoff A, Sehested J, Chorkendorff I, Helveg S, *et al.* Dynamic behavior of cuzn nanoparticles under oxidizing and reducing conditions. *Journal of Physical Chemistry C* **2015**, 119(5): 2804-2812.
- [65] Velazquez-Palenzuela A, Masini F, Pedersen AF, Escudero-Escribano M, Deiana D, Malacrida P, *et al.* The enhanced activity of mass-selected ptxgd nanoparticles for oxygen electroreduction. *J. Catal.* **2015**, 328: 297-307.
- [66] Palmer RE, Cai RS, Vernieres J. Synthesis without solvents: the cluster (nanoparticle) beam route to catalysts and sensors. *Acc. Chem. Res.* **2018**, 51(9): 2296-2304.
- [67] Palmer RE, Cao L, Yin F. Note: proof of principle of a new type of cluster beam source with potential for scale-up. *Rev. Sci. Instrum.* **2016**, 87(4).
- [68] Bewig L, Buck U, Mehlmann C, Winter M. Seeded supersonic alkali cluster beam source with refilling system. *Rev. Sci. Instrum.* **1992**, 63(8): 3936-3938.
- [69] Dietz TG, Duncan MA, Powers DE, Smalley RE. Laser production of supersonic metal cluster beams. *J. Chem. Phys.* **1981**, 74(11): 6511-6512.
- [70] Duncan MA. Invited review article: laser vaporization cluster sources. *Rev. Sci. Instrum.* **2012**, 83(4): 041101.
- [71] Pratontep S, Carroll SJ, Xirouchaki C, Streun M, Palmer RE. Size-selected cluster beam source based on radio frequency magnetron plasma sputtering and gas condensation. *Rev. Sci. Instrum.* **2005**, 76(4).

- [72] Haberland H, Karrais M, Mall M. A new type of cluster and cluster ion-source. *Zeitschrift Fur Physik D-Atoms Molecules and Clusters* **1991**, 20(1-4): 413-415.
- [73] Haberland H, Karrais M, Mall M, Thurner Y. Thin films from energetic cluster impact: a feasibility study. *Journal of Vacuum Science & Technology A: Vacuum, Surfaces, and Films* **1992**, 10(5): 3266-3271.
- [74] Siekmann HR, Luder C, Faehrmann J, Lutz HO, Meiwesbroer KH. The pulsed-arc cluster ion-source (pacis). *Zeitschrift Fur Physik D-Atoms Molecules and Clusters* **1991**, 20(1-4): 417-420.
- [75] Gantefor G, Siekmann HR, Lutz HO, Meiwesbroer KH. Pure metal and metal-doped rare-gas clusters grown in a pulsed arc cluster ion source. *Chem. Phys. Lett.* **1990**, 165(4): 293-296.
- [76] Lu WY, Huang RB, Ding JQ, Yang SH. Generation of fullerenes and metal-carbon clusters in a pulsed arc cluster ion source (PACIS). *J. Chem. Phys.* **1996**, 104(17): 6577-6581.
- [77] Forbes RG. Understanding how the liquid-metal ion source works. *Vacuum* **1997**, 48(1): 85-97.
- [78] Swanson LW. Liquid-metal ion sources: mechanism and applications. *Nuclear Instruments & Methods in Physics Research* **1983**, 218(1-3): 347-353.
- [79] Torkar K, Riedler W, Escoubet CP, Fehringer M, Schmidt R, Grard RJL, *et al.* Active spacecraft potential control for cluster: implementation and first results. *Ann. Geophys.* **2001**, 19(10-12): 1289-1302.
- [80] Cai R, Jian N, Murphy S, Bauer K, Palmer RE. A new method to prepare colloids of size-controlled clusters from a matrix assembly cluster source. *APL Materials* **2017**, 5(5): 053405.

- [81] Tafreshi HV, Benedek G, Piseri P, Vinati S, Barborini E, Milani P. A simple nozzle configuration for the production of low divergence supersonic cluster beam by aerodynamic focusing. *Aerosol Sci. Technol.* **2002**, 36(5): 593-606.
- [82] Milani P, Podesta A, Piseri P, Barborini E, Lenardi C, Castelnovo C. Cluster assembling of nanostructured carbon films. *Diamond Relat. Mater.* **2001**, 10(2): 240-247.
- [83] Shafiee S, Topal E. When will fossil fuel reserves be diminished? *Energy Policy* **2009**, 37(1): 181-189.
- [84] Pacala S, Socolow R. Stabilization wedges: solving the climate problem for the next 50 years with current technologies. *Science* **2004**, 305(5686): 968-972.
- [85] Kapdan IK, Kargi F. Bio-hydrogen production from waste materials. *Enzyme Microb. Technol.* **2006**, 38(5): 569-582.
- [86] Turner JA. Sustainable hydrogen production. *Science* **2004**, 305(5686): 972-974.
- [87] Conte M, Iacobazzi A, Ronchetti M, Vellone R. Hydrogen economy for a sustainable development: state-of-the-art and technological perspectives. *J. Power Sources* **2001**, 100(1-2): 171-187.
- [88] Hosseini SE, Wahid MA. Hydrogen production from renewable and sustainable energy resources: promising green energy carrier for clean development. *Renewable & Sustainable Energy Reviews* **2016**, 57: 850-866.
- [89] Ryabchuk VK, Kuznetsov VN, Emeline AV, Artem'ev YM, Kataeva GV, Horikoshi S, *et al.* Water will be the coal of the future-the untamed dream of Jules Verne for a solar fuel. *Molecules* **2016**, 21(12).
- [90] Anantharaj S, Ede SR, Sakthikumar K, Karthick K, Mishra S, Kundu S. Recent trends and perspectives in electrochemical water splitting with an emphasis on sulfide,

- selenide, and phosphide catalysts of Fe, Co, and Ni: a review. *Acs Catalysis* **2016**, 6(12): 8069-8097.
- [91] Tee SY, Win KY, Teo WS, Koh LD, Liu SH, Teng CP, *et al.* Recent progress in energy driven water splitting. *Advanced Science* **2017**, 4(5).
- [92] BP statistical review of world energy **2018**.
- [93] Yang MQ, Wang J, Wu H, Ho GW. Noble metal-free nanocatalysts with vacancies for electrochemical water splitting. *Small* **2018**, 14(15).
- [94] Yang C-J. An impending platinum crisis and its implications for the future of the automobile. *Energy Policy* **2009**, 37(5): 1805-1808.
- [95] Novoselov KS, Jiang D, Schedin F, Booth TJ, Khotkevich VV, Morozov SV, *et al.* Two-dimensional atomic crystals. *Proc. Natl. Acad. Sci. U. S. A.* **2005**, 102(30): 10451-10453.
- [96] Chhowalla M, Shin HS, Eda G, Li LJ, Loh KP, Zhang H. The chemistry of two-dimensional layered transition metal dichalcogenide nanosheets. *Nat. Chem.* **2013**, 5(4): 263-275.
- [97] Akinwande D, Petrone N, Hone J. Two-dimensional flexible nanoelectronics. *Nat. Commun.* **2014**, 5: 5678.
- [98] Gemming S, Seifert G. Nanocrystals: catalysts on the edge. *Nat Nanotechnol* **2007**, 2(1): 21-22.
- [99] Cuddy MJ, Arkill KP, Wang ZW, Komsa HP, Krasheninnikov AV, Palmer RE. Fabrication and atomic structure of size-selected, layered mos clusters for catalysis. *Nanoscale* **2014**.
- [100] Yang D, Sandoval S, Divigalpitiya W, Irwin J, Frindt R. Structure of single molecular layer MoS₂. *Physical Review B* **1991**, 43(14): 12053-12056.

- [101] Joswig JO, Lorenz T, Wendumu TB, Gemming S, Seifert G. Optics, mechanics, and energetics of two-dimensional MoS₂ nanostructures from a theoretical perspective. *Acc. Chem. Res.* **2015**, 48(1): 48-55.
- [102] Jaramillo TF, Jorgensen KP, Bonde J, Nielsen JH, Horch S, Chorkendorff I. Identification of active edge sites for electrochemical H₂ evolution from MoS₂ nanocatalysts. *Science* **2007**, 317(5834): 100-102.
- [103] Kibsgaard J, Jaramillo TF, Besenbacher F. Building an appropriate active-site motif into a hydrogen evolution catalyst with thiomolybdate [Mo₃S₁₃]²⁻ clusters. *Nat. Chem.* **2014**, 6(3): 248-253.
- [104] Hinnemann B, Moses PG, Bonde J, Jorgensen KP, Nielsen JH, Horch S, *et al.* Biomimetic hydrogen evolution: MoS₂ nanoparticles as catalyst for hydrogen evolution. *J. Am. Chem. Soc.* **2005**, 127(15): 5308-5309.
- [105] Bonde J, Moses PG, Jaramillo TF, Norskov JK, Chorkendorff I. Hydrogen evolution on nano-particulate transition metal sulfides. *Faraday Discuss.* **2008**, 140: 219-231.
- [106] Escalera-López D, Niu Y, Yin J, Cooke K, Rees NV, Palmer RE. Enhancement of the hydrogen evolution reaction from Ni-MoS₂ hybrid nanoclusters. *ACS Catalysis* **2016**, 6(9): 6008-6017.
- [107] Niu Y, Park S, Palmer R. Modification of deposited, size-selected MoS₂ nanoclusters by sulphur addition: an aberration-corrected stem study. *Inorganics* **2016**, 5(1): 1.
- [108] Castro-Guerrero CF, Deepak FL, Ponce A, Cruz-Reyes J, Valle-Granados MD, Fuentes-Moyado S, *et al.* Structure and catalytic properties of hexagonal molybdenum disulfide nanoplates. *Catalysis Science & Technology* **2011**, 1(6): 1024.
- [109] Chretien S, Buratto S, Metiu H. Catalysis by very small Au clusters. *Curr. Opin. Solid State Mater. Sci.* **2007**, 11(5-6): 62-75.

- [110] Han CW, Majumdar P, Marinero EE, Aguilar-Tapia A, Zanella R, Greeley J, *et al.* Highly stable bimetallic AuIr/TiO₂ catalyst: physical origins of the intrinsic high stability against sintering. *Nano Lett.* **2015**, 15(12): 8141-8147.
- [111] Hansen TW, Delariva AT, Challa SR, Datye AK. Sintering of catalytic nanoparticles: particle migration or ostwald ripening? *Acc. Chem. Res.* **2013**, 46(8): 1720-1730.
- [112] Hammer B, Norskov JK. Why gold is the noblest of all the metals. *Nature* **1995**, 376(6537): 238-240.
- [113] Bone WA, Wheeler RV. The combination of hydrogen and oxygen in contact with hot surfaces. *Proceedings of the Royal Society A: Mathematical, Physical and Engineering Sciences* **1906**, 77(515): 146-147.
- [114] Bone WA, Andrew GW. Studies upon catalytic combustion-Part I. The union of carbon monoxide and oxygen in contact with a gold surface. *Proceedings of the Royal Society A: Mathematical, Physical and Engineering Sciences* **1925**, 109(751): 459-476.
- [115] Sennewald K, Vogt W, Glaser H. Verfahren zur herstellung von vinylacetat. *Patent DE1244766B* **1967**.
- [116] Bond GC, Sermon PA. Gold catalysts for olefin hydrogenation. *Gold Bulletin* **1973**, 6(4): 102-105.
- [117] Haruta M, Kobayashi T, Sano H, Yamada N. Novel gold catalysts for the oxidation of carbon-monoxide at a temperature far below 0-degrees-C. *Chem. Lett.* **1987**(2): 405-408.
- [118] Haruta M, Yamada N, Kobayashi T, Iijima S. Gold catalysts prepared by coprecipitation for low-temperature oxidation of hydrogen and of carbon-monoxide. *J. Catal.* **1989**, 115(2): 301-309.
- [119] Hutchings G. Vapor phase hydrochlorination of acetylene: correlation of catalytic activity of supported metal chloride catalysts. *J. Catal.* **1985**, 96(1): 292-295.

- [120] Haruta M. Chance and necessity: My encounter with gold catalysts. *Angew. Chem. Int. Ed. Engl.* **2014**, 53(1): 52-56.
- [121] Taketoshi A, Haruta M. Size- and structure-specificity in catalysis by gold clusters. *Chem. Lett.* **2014**, 43(4): 380-387.
- [122] Niu Y, Schlexer P, Sebok B, Chorkendorff I, Pacchioni G, Palmer RE. Reduced sintering of mass-selected Au clusters on SiO₂ by alloying with Ti: an aberration-corrected STEM and computational study. *Nanoscale* **2018**, 10(5): 2363-2370.
- [123] Freund HJ, Meijer G, Scheffler M, Schlögl R, Wolf M. CO oxidation as a prototypical reaction for heterogeneous processes. *Angew. Chem. Int. Ed. Engl.* **2011**, 50(43): 10064-10094.
- [124] Christmann K, Schwede S, Schubert S, Kudernatsch W. Model studies on CO oxidation catalyst systems: titania and gold nanoparticles. *Chemphyschem* **2010**, 11(7): 1344-1363.
- [125] Van Spronsen MA, Frenken JWM, Groot IMN. Surface science under reaction conditions: CO oxidation on Pt and Pd model catalysts. *Chem. Soc. Rev.* **2017**, 46(14): 4347-4374.
- [126] Ertl G. *Reactions at solid surfaces*, vol. 14. John Wiley & Sons, **2010**.
- [127] Wang YG, Cantu DC, Lee MS, Li J, Glezakou VA, Rousseau R. CO oxidation on Au/TiO₂: condition-dependent active sites and mechanistic pathways. *J. Am. Chem. Soc.* **2016**, 138(33): 10467-10476.
- [128] Saavedra J, Powell C, Panthi B, Pursell CJ, Chandler BD. CO oxidation over Au/TiO₂ catalyst: pretreatment effects, catalyst deactivation, and carbonates production. *J. Catal.* **2013**, 307: 37-47.
- [129] Min BK, Friend CM. Heterogeneous gold-based catalysis for green chemistry: low temperature CO oxidation and propene oxidation. *Chem. Rev.* **2007**, 107(6): 2709-2724.

- [130] Christmann K, Schwede S, Schubert S, Kudernatsch W. Model studies on CO oxidation catalyst systems: titania and gold nanoparticles. *Chemphyschem* **2010**, 11(7): 1344-1363.
- [131] Widmann D, Behm RJ. Activation of molecular oxygen and the nature of the active oxygen species for CO oxidation on oxide supported Au catalysts. *Acc. Chem. Res.* **2014**, 47(3): 740-749.
- [132] Fujitani T, Nakamura I. Mechanism and active sites of the oxidation of CO over Au/TiO₂. *Angew. Chem. Int. Ed. Engl.* **2011**, 50(43): 10144-10147.
- [133] Remediakis IN, Lopez N, Nørskov JK. CO oxidation on rutile-supported Au nanoparticles. *Angew. Chem.* **2005**, 117(12): 1858-1860.
- [134] Duan Z, Henkelman G. CO oxidation at the Au/TiO₂ boundary: The role of the Au/Ti_{5c} site. *ACS Catalysis* **2015**, 5(3): 1589-1595.
- [135] Green IX, Tang W, Neurock M, Yates JT, Jr. Supporting information-spectroscopic observation of dual catalytic sites during oxidation of CO on a Au/TiO₂ catalyst. *Science* **2011**, 333(6043): 736-739.
- [136] Green IX, Tang WJ, Neurock M, Yates JT. Insights into catalytic oxidation at the Au/TiO₂ dual perimeter sites. *Acc. Chem. Res.* **2014**, 47(3): 805-815.
- [137] Kast P, Kučerová G, Behm RJ. On the nature of the active Au species: CO oxidation on cyanide leached Au/TiO₂ catalysts. *Catal. Today* **2015**, 244: 146-160.
- [138] Widmann D, Behm RJ. Active oxygen on a Au/TiO₂ catalyst: formation, stability, and CO oxidation activity. *Angew. Chem. Int. Ed. Engl.* **2011**, 50(43): 10241-10245.
- [139] Janssens TVW, Clausen BS, Hvolbaek B, Falsig H, Christensen CH, Bligaard T, *et al.* Insights into the reactivity of supported Au nanoparticles: combining theory and experiments. *Top. Catal.* **2007**, 44(1-2): 15-26.

- [140] Bollinger MA, Vannice MA. A kinetic and drifts study of low-temperature carbon monoxide oxidation over Au/TiO₂ catalysts. *Applied Catalysis B-Environmental* **1996**, 8(4): 417-443.
- [141] Liu H, Kozlov AI, Kozlova AP, Shido T, Asakura K, Iwasawa Y. Active oxygen species and mechanism for low-temperature CO oxidation reaction on a TiO₂-supported Au catalyst prepared from Au(PPh₃)(NO₃) and as-precipitated titanium hydroxide. *J. Catal.* **1999**, 185(2): 252-264.
- [142] Remediakis IN, Lopez N, Norskov JK. CO oxidation on rutile-supported Au nanoparticles. *Angewandte Chemie-International Edition* **2005**, 44(12): 1824-1826.
- [143] Laursen S, Linic S. Geometric and electronic characteristics of active sites on TiO₂-supported au nano-catalysts: insights from first principles. *Phys. Chem. Chem. Phys.* **2009**, 11(46): 11006-11012.
- [144] Grisel RJH, Nieuwenhuys BE. Selective oxidation of CO over supported Au catalysts. *J. Catal.* **2001**, 199(1): 48-59.

Chapter 2

Experimental Methods

In this chapter, we discuss the general working principles of the main experimental techniques used in this thesis. The detailed parameters for each project are addressed in the according chapter. All the projects involved in this thesis are joint research with different collaborators. The cluster fabrication and STEM study work were conducted by me, and the catalytic measurements and theoretical calculation were done by collaborators. In the Ni-MoS₂ research (chapter 3), the clusters were produced by the dual-magnetron cluster beam source in Teer Coatings Ltd with the help of Dr Jinlong Yin. In the research of sulphur-enrichment of MoS₂, the clusters were produced by me with the cluster beam source in NPRL. All the HER measurements on Ni-MoS₂ and sulphur-enriched MoS₂ were conducted by Daniel Escalera Lopez (PhD student from Chemical Engineering, UoB), and the XPS measurements were conducted at Aston University. In the Au/Ti project (chapter 5), the clusters were made in NPRL; the CO oxidation measurements, XPS and LEIS were conducted together with Bela Sebok at DTU; and the DFT calculation was done by Philomena Schlexer from University of Milano-Bicocca.

2.1 Cluster Beam Deposition

2.1.1 Cluster beam source

The size-selected cluster beam source in our group shown in Figure 2.1 belongs to magnetron sputtering source, which can continuously produce high-density cluster beam with plasma sputtering and gas condensation techniques. It consists of four high vacuum chambers respectively for cluster generation, ion optics, mass selection, and deposition. Soft copper gaskets are used to bolt together those chambers to create semi-permanent seals, while a Viton gasket is used in the load lock section since it is frequently opened to load or unload samples. Each chamber is equipped with the backing pump and turbo-molecular pump to ensure the whole system is running under a high-vacuum (HV) environment. The oil-based rotary pumps and dry scroll pumps can provide a backing vacuum of 10^{-2} mbar, and then the turbo-molecular pumps can pump down the system to a pressure around 10^{-7} mbar.

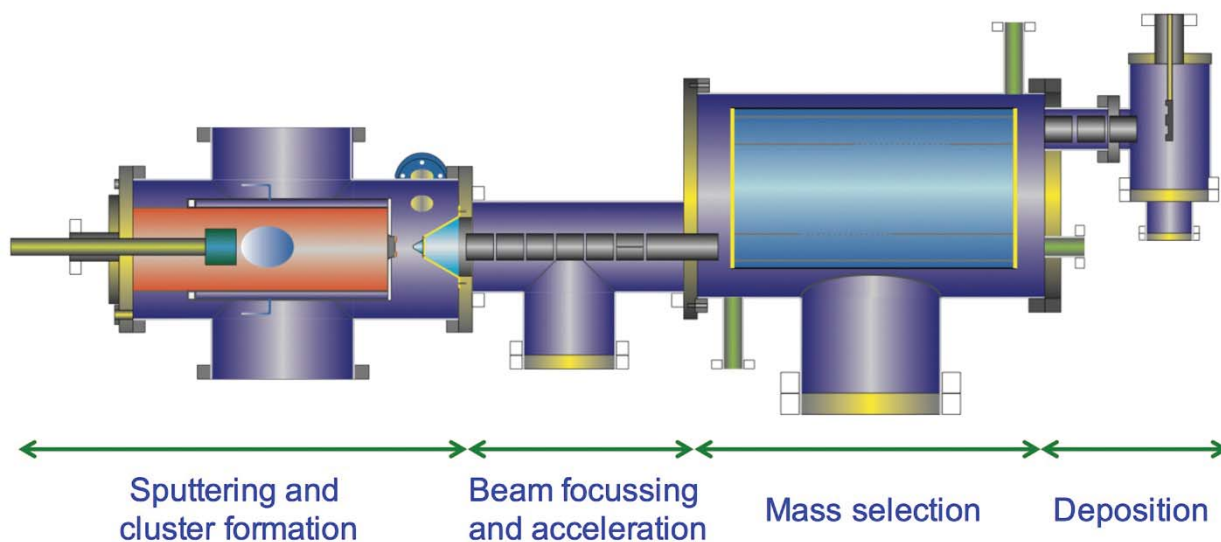


Figure 2.1 Schematic illustration of the size selected cluster beam source in our group. The cluster form in the first (from left) chamber by magnetron sputtering and gas condensation; a focused cluster beam is produced by supersonic expansion and ion optics; then the cluster beam is mass-selected by a time-of-flight mass filter and inducted into the deposition chamber.

The single-element clusters can be fabricated from the cluster beam source shown above with a single-element target. In order to prepare binary or hybrid clusters, two methods can be implemented. One method is employing single-magnetron cluster beam source with an alloy target to make alloy clusters. However, the composition of the clusters made from this method is hardly tuned. The other method is using multi-magnetron cluster beam source (described in Chapter 3) to produce binary or hybrid clusters. With this method, the composition of the clusters can be moderately controlled by tuning the power on each magnetron.

2.1.2 Cluster Formation

A bulk target can be mounted on top of a water-cooled copper plate at the front of the magnetron gun inside the cluster generation chamber. The cluster generation chamber is cooled down by a continuous liquid nitrogen flow.

Argon (Ar) gas flows into the generation chamber from the magnetron gun and is ionised to a plasma state by a high potential between the target (cathode) and the shield (anode, ground) generated by a DC power supplier. Then the target is sputtered by the Ar^+ ions. The atoms in the target will be sputtered out if the energy of the Ar^+ is higher than the binding energy of the atoms in the target. Meanwhile, secondary electrons are ejected out, which further ionise more Ar atoms. The secondary electrons are confined in helical orbits by the magnets behind the copper plate in the magnetron head, which can enhance the ionisation process to produce more Ar^+ ions and free electrons. The magnets can also confine the plasma to the region above the target to avoid the damage of other parts from the plasma. Besides this advantage of magnetron sputtering method, the other advantage is that a cluster beam can be directly obtained by

focusing the sputtered materials without further ionisation step due to a high ionisation rate (at least 30%) of the sputtered materials [1].

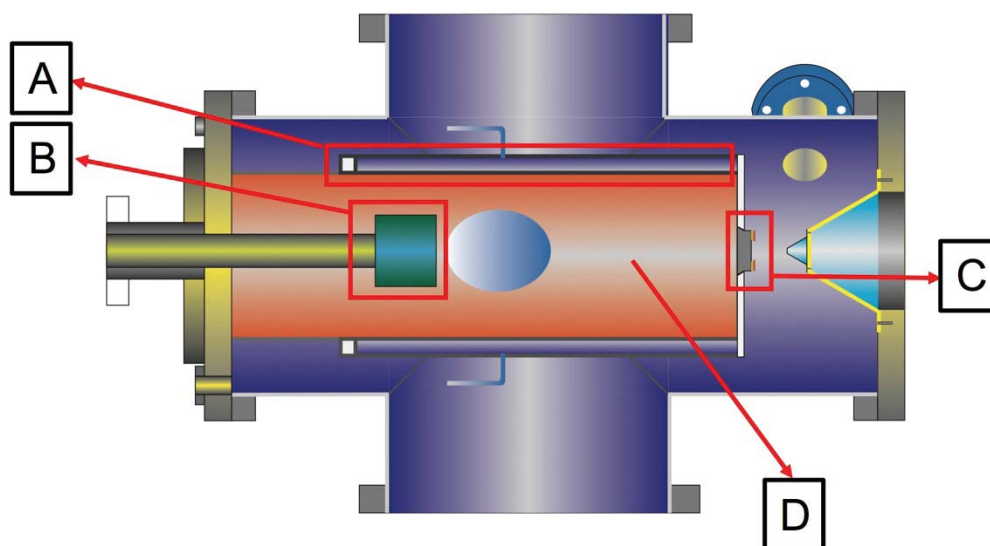


Figure 2.2 Schematic illustration of the cluster generation chamber. (A) Liquid nitrogen jacket, (B) movable magnetron, (C) adjustable nozzle, (D) nucleation region.

During the sputtering, Helium (He) gas is introduced into the cluster generation chamber. The “hot” sputtered atoms and cluster seeds will be cooled down, nucleate and grow into clusters by three-body collisions. The nucleation time and the pressure in the chamber are the two main parameters to tune the size of the clusters. The nucleation distance can be controlled by moving the magnetron forwards or backwards along the axis of the cluster beam, while the pressure can be controlled by the gas flows and an adjustable nozzle located at the exit of the cluster generation chamber (Figure 2.2).

2.1.3 Cluster Beam Optics

The cluster beam exits the cluster generation chamber from the nozzle in a supersonic gas expansion. To realise the size selection with a high resolution, a well-focused cluster beam

with a spot size of around 10 mm is needed. The central proportion of the cluster beam is extracted by a skimmer (Figure 2.3) before ion optics, and the off-axis part is removed and pumped away. The beam is then focused by electrical fields generated by sets of optics lens including extraction lens and a set of einzel lens. In order to correct the misalignment of the beam in the axial direction, split deflector lenses are introduced to tune the cluster beam in the horizontal axis (X) and vertical axis (Y) directions.

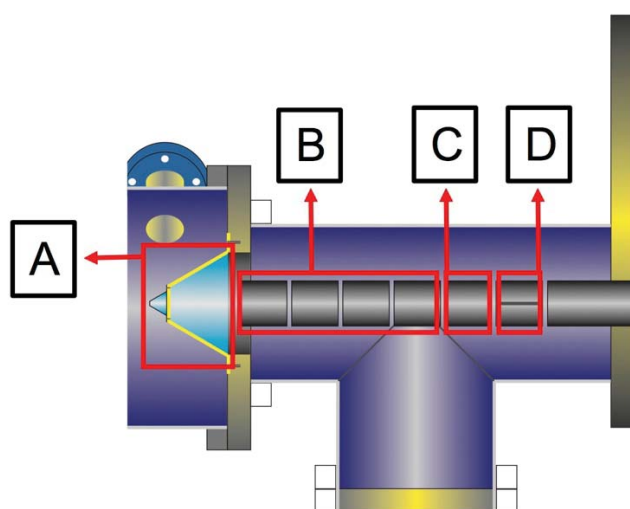


Figure 2.3 Schematic illustration of the ion optics chamber. (A) Skimmer, (B) extraction and einzel lenses, (C) horizontal axis (X) deflector, (D) vertical axis (Y) deflector.

2.1.4 Time-of-Flight Mass Filter

The schematic of the linear Time-of-Flight mass filter is shown in Figure 2.4. The mass filter consists of three regions including the acceleration region, the flight region and the deceleration region. The accelerated and focused cluster beam enters the mass filter via an adjustable aperture (1-8 mm in height) at bottom. There are four isolated plates in the mass filter, two

plates at the top and the bottom perform as electrostatic pulse suppliers and two more central mesh plates in between form a field-free drift zone. The selected beam can pass through the field-free drift zone and go to the deposition chamber via the other adjustable aperture at the top.

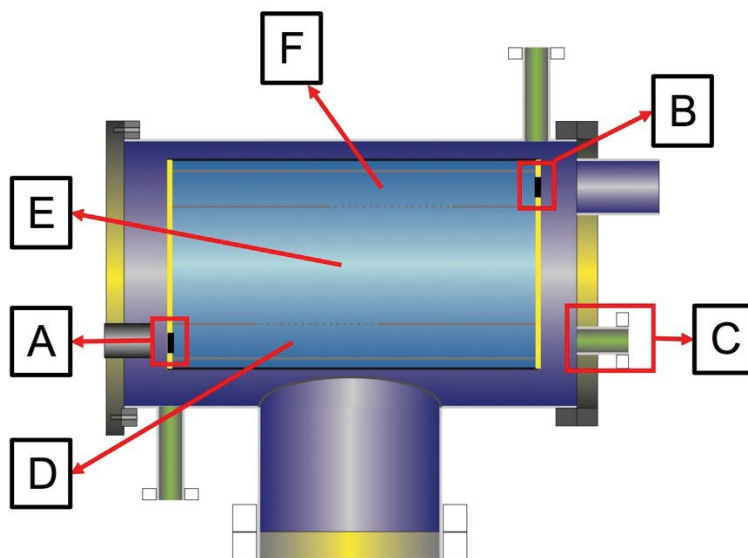


Figure 2.4 Schematic illustration of the Time-of-Flight chamber. (A) Adjustable height entrance slit, (B) adjustable height exit slit, (C) Faraday cup, (D) entrance pulse region, (E) field-free drift region, (F) exit pulse region.

The basic principle of this Time-of-Flight mass filter is to provide the cluster beam with a momentum perpendicular to the beam direction via an electrostatic pulse. The vertical velocity of the cluster is corresponding with its mass. The clusters with different masses will travel different distances in a particular time. Then the perpendicular momentum of the cluster is removed by an opposite electrostatic pulse. Clusters with different masses are successfully separated due to their different perpendicular movement.

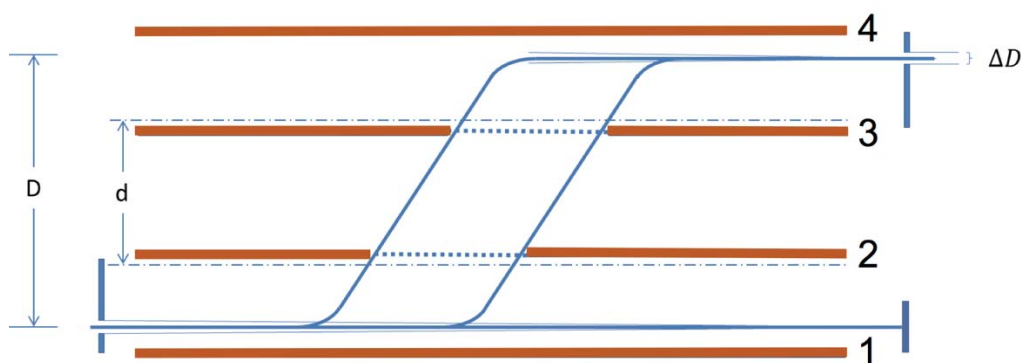


Figure 2.5 Schematic of the principle of the lateral Time-of-Flight mass filter [2].

Figure 2.5 is the schematic of the principle of the mass filter. The cluster beam enters the mass filter via the bottom aperture and gains a perpendicular momentum from the short high voltage pulse applied on plate 1. In order to ensure all the clusters gain the same perpendicular momentum, the pulse length is designed to be short enough to make sure there is no cluster leaving the acceleration region (between plate 1 and 2). The permitted clusters can travel into and out of the field-free region between plate 2 and 3 via the central mesh. An equal but opposite pulse is then added onto plate 4 to offset the perpendicular momentum of the clusters. Since the pulses added on plate 1 and 4 have no effect on the horizontal velocity of the cluster, the permitted clusters will travel into the deposition chamber via the exit aperture.

The mass resolution of the mass filter can be deduced from the mass dependence of the perpendicular movement distance. If m_0 is the mass of a cluster which is transmitted by the mass filter, and v_{m_0} is its perpendicular velocity. Since all clusters obtain the same perpendicular momentum in a given pulse length, a cluster with a mass of m will acquire the velocity [2]:

$$v_m = v_{m_0} \frac{m_0}{m}. \quad (2.1)$$

Its perpendicular movement distance is [2]:

$$D_m = \frac{1}{2} v_m t_p + v_m t_d + \frac{1}{2} v_m t_p = \frac{m_0}{m} D, \quad (2.2)$$

where D is the total perpendicular movement distance of the transmitted clusters, t_p is the pulse length, and t_d is the field-free flight time. Then the derivative of the perpendicular movement distance with respect to the mass is [2]:

$$\frac{dD_m}{dm} \Big|_{m=m_0} = -\frac{m_0 D}{m^2} \Big|_{m=m_0} = -\frac{D}{m_0}. \quad (2.3)$$

The exit aperture allows the clusters with a certain range of masses to go through. This certain range of masses is given by [2]:

$$\Delta m = \frac{dm}{dD_m} \Delta D = -\frac{m_0}{D} \Delta D. \quad (2.4)$$

Then the mass resolution is given by:

$$R = \frac{m}{\Delta m} = \frac{D}{\Delta D}. \quad (2.5)$$

This implies that the maximum mass resolution is determined by the ratio of the perpendicular movement distance and the exit aperture height [2].

2.1.5 Cluster Deposition

After the size selection from the mass filter, the size-selected clusters are focused to a beam with a diameter of ~1 mm by a set of lens located before the deposition chamber. The clusters are then deposited onto the substrates held on a sample holder suspended in the deposition chamber. During deposition, a bias with a range of 0-1500 V will be applied on the substrate, which determines the impact energy of the clusters landed on the support.

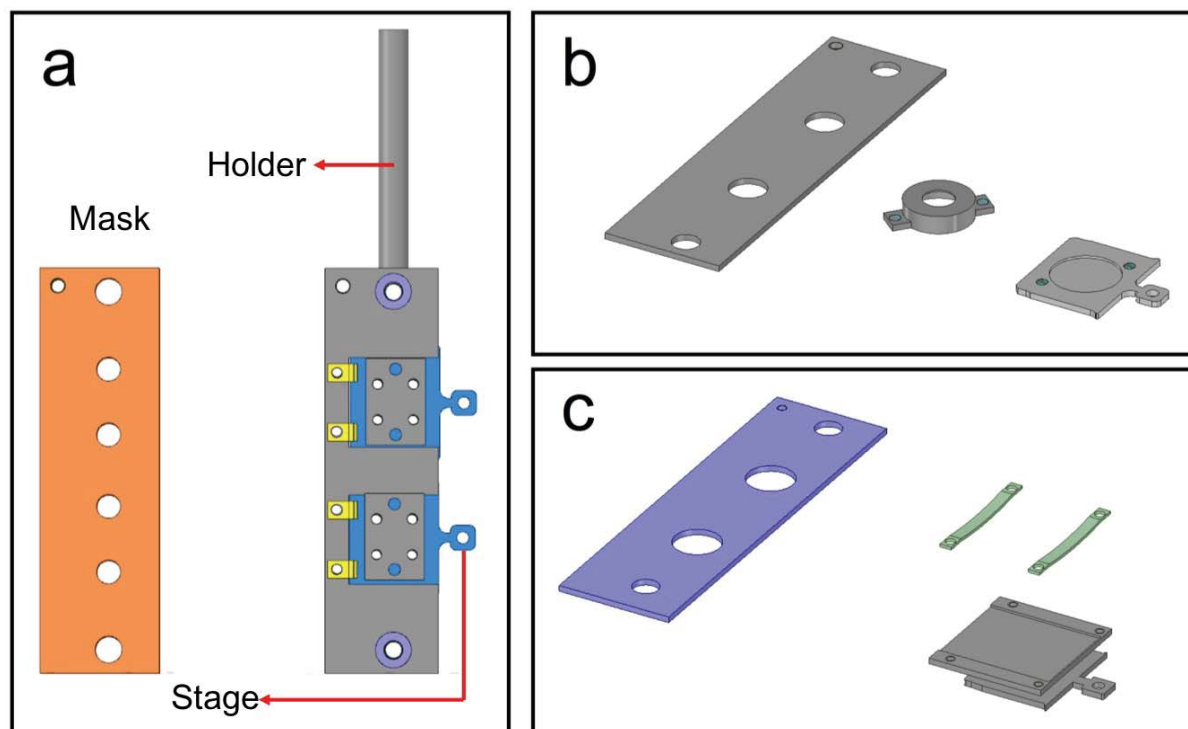


Figure 2.6 Sample holder schematics. (a) Sample holder, stage and mask for cluster deposition on TEM grids, (b) sample stage and mask for cluster deposition on glassy carbon stubs, and (c) sample stage and mask for cluster deposition on micro-reactor and for large area.

The sample stages for different substrates are shown in Figure 2.6. Figure 2.6a shows the sample holder with two TEM grid stages on and the mask for the deposition on TEM grid. The mask has 4 mm diameter apertures to let the cluster beam go through, and is separated from the sample holder by Teflon spacer. The cluster beam current is measured from the sample holder by a picoammeter to monitor the cluster flux. Figure 2.6b is the schematic of the sample stage and mask for the deposition on glassy carbon. The glassy carbon is used for electrochemical measurement, which is a cylinder with 5 mm diameter and 3 mm in height. Figure 2.6c illustrates the stage and mask for the deposition on micro-reactor, which can also be used for large area deposition. The micro-reactor is used for gas catalysis with dimensions of 20 mm × 16 mm.

2.2 Scanning Transmission Electron Microscopy (STEM)

Scanning transmission electron microscope (STEM) is regarded as one of the greatest inventions of last century and has been a powerful tool in the field of nanoscience. STEM, especially aberration-corrected STEM, becomes a crucial characterisation technique with extremely high analytical and spatial resolution. The STEM in our group is JEOL 2100F which is aberration-corrected, and a schematic is shown in Figure 2.7. It mainly consists of electron source, lens and aberration corrector, imaging system and element analysis system [3, 4].

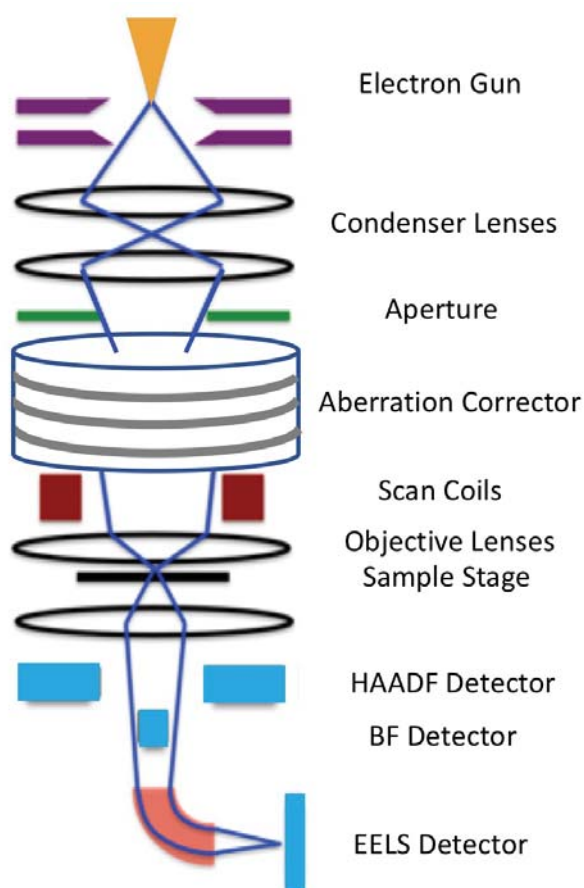


Figure 2.7 Schematic of an aberration-corrected STEM and a photograph of the JEOL 2100F STEM in our group.

The electron beam is generated and accelerated from electron gun, then focused by the condenser lenses. An aperture with a set of selectable sizes is located under the condenser lenses and used to remove the wide scattered electrons. Since the lenses are not perfect, there is an aberration. The Cs-corrector (Cs means spherical aberration) is used to compensate the spherical aberration of the electron beam. An electron probe is then formed from the Cs-corrected electron beam by the objective lens and scans over the selected area of the sample controlled by the scan coil. The electron is scattered by the sample and collected by the high angle annular dark field (HAADF) detector or bright field (BF) detector. Then the signals collected by the detector are processed into images.

2.2.1 Electron Source

STEM uses electrons as a probe to get a much higher resolution than visible light microscopy. Thermionic electron sources and field emission electron sources (also known as field emission gun, FEG) are the two typical electron sources for the electron microscope. Thermionic electron sources provide electrons with enough energy by applying high temperature to overcome the potential barrier and form an electron flow. Compared with FEGs, thermionic electron sources are cheap and easy to maintain, but they are less monochromatic.

Unlike thermionic sources, FEGs use a strong electric field to let the electrons cross the potential barrier. A FEG consists of a very sharp tip and two anodes, its basic principle is illustrated in Figure 2.8. The electrons are extracted out of the tip through the electric field formed by the first anode, and then can be accelerated to a high energy (200 kV or more) by the second electrode. In our STEM, the electron source is a Schottky FEG which combines both heat and field emissions and is made of Lanthanum hexaboride (LaB_6). The advantage of

Schottky FEG is its lower vacuum requirement than that of the cold FEG and better brightness than that of the thermionic source.

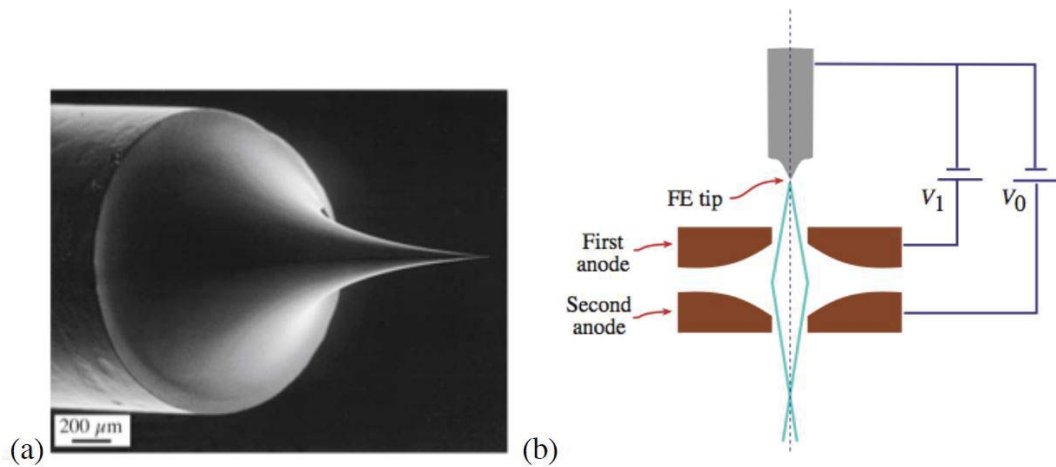


Figure 2.8 (a) A very fine field emission gun tip and (b) a schematic of the configuration in a FEG. The schematics are reproduced from reference [5].

2.2.2 Lens and Aberration

The electron beam from the electron source is controlled by the magnetic electron lens in TEM. The configuration of a magnetic lens is shown in Figure 2.9. It consists of two main parts: cylindrically symmetrical polepieces and coils. The polepieces are made of magnetic materials like soft iron and are surrounded by copper coils. A magnetic field is formed when current is applied to the coils, and the electron beam is refracted in a controllable manner by this magnetic field when passing through the lens.

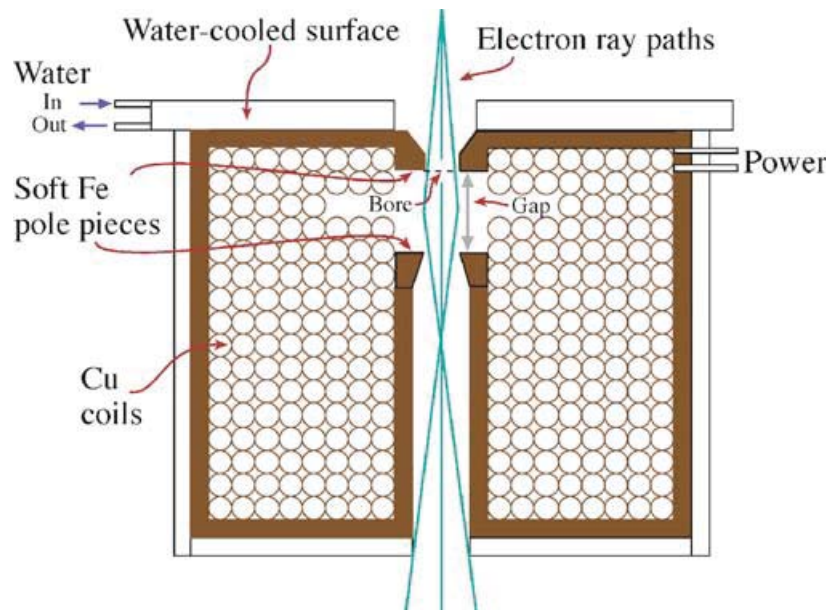


Figure 2.9 Schematic diagram of magnetic lens used in the TEM, reproduced from reference [5].

Given that the accelerating voltage in our STEM is 200 kV, the wavelength of the electron beam is 0.00251 nm. If the wavelength of the electron beam is the only factor of the spatial resolution of STEM, the maximum spatial resolution can be 0.003 nm. However, the spatial resolution of the most advanced STEM in practice is 0.035 nm. The gap between the theoretical value and practical value comes from the imperfections of the electromagnetic lenses.

Spherical aberration and chromatic aberration are the two major types of aberration in STEM. Spherical aberration (Figure 2.10) results from the imperfection of the magnetic field. The strength of the magnetic field depends on the distance to the axis, the further it is off the axis, the stronger it is. When the electron beam passes through the magnetic lens, the further the beam is off the axis, the stronger it is condensed. Therefore, the electron beam is converged to an area with a small radius from one point. Chromatic aberration occurs since the electron beam extracted from the electron gun is with a certain energy spread. The energy spread is in

a range from ~0.3 eV to ~1 eV. Due to the energy difference of the electrons, they cannot be converged to the same focal point. The energy spread range is so small that the influence of the chromatic aberration on the resolution is limited. Chromatic aberration will get worse if the specimen is thick since energy loss is caused during the interaction between the specimen and the electron beam. A thin specimen is a crucial requirement for STEM study.

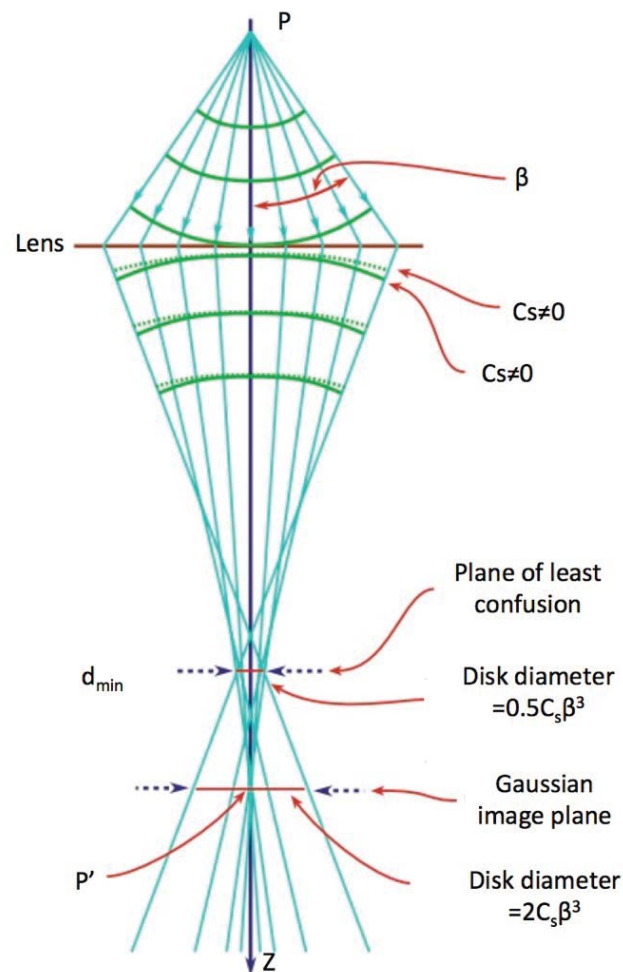


Figure 2.10 Schematic of spherical aberration. C_s is the spherical aberration coefficient, β is the maximum collection angle of objective-lens aperture, reproduced from reference [5].

There are two main ways to compensate the spherical aberration, Nion corrector and CEOS system. The Nion corrector is a quadrupole-octupole corrector proposed by O.L. Krivanek et al.[6, 7] The CEOS system is a double-hexapole corrector designed by M. Haider et al.[8] The spherical aberration corrector in our STEM is a double-hexapole corrector. The main idea of the corrector is to spread the off-axis beams with a diverging lens, so that they can be refocused to the focal point on Gaussian-image plane.

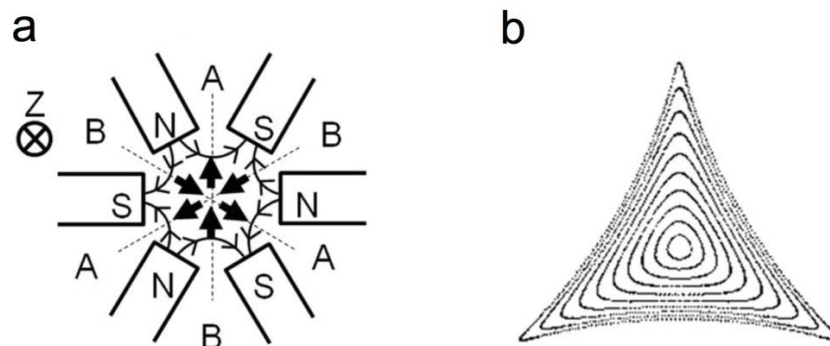


Figure 2.11 Schematic of (a) hexapole and (b) electron beam shape after passing through the hexapole, reproduced from reference [9].

Figure 2.11a illustrates the configuration of the hexapole. When the electron beam travels through the hexapole field with a direction into the plane of the paper, the electrons experience Lorentz force shown with arrows in Figure 2.11a. The electrons converge or diverge in three-fold symmetry shown in Figure 2.11b. In the divergence part, the further the electron is away from the axis, the stronger force it experiences, then the more it diverges. On the other hand, the closer the electron is to the axis in the convergence part, the less it converges. This gives the electron beam a divergence effect for all azimuths and introduces a “negative” spherical aberration corresponding to the “positive” spherical aberration discussed above. However, this

also introduces a three-fold astigmatism. The transfer lenses shown in Figure 2.12 transfer the electron beam from the first hexapole to the second one with a point inversion for the beam. After the second hexapole, the three-fold astigmatism can be eliminated (Figure 2.12), but a further “negative” spherical aberration is introduced.

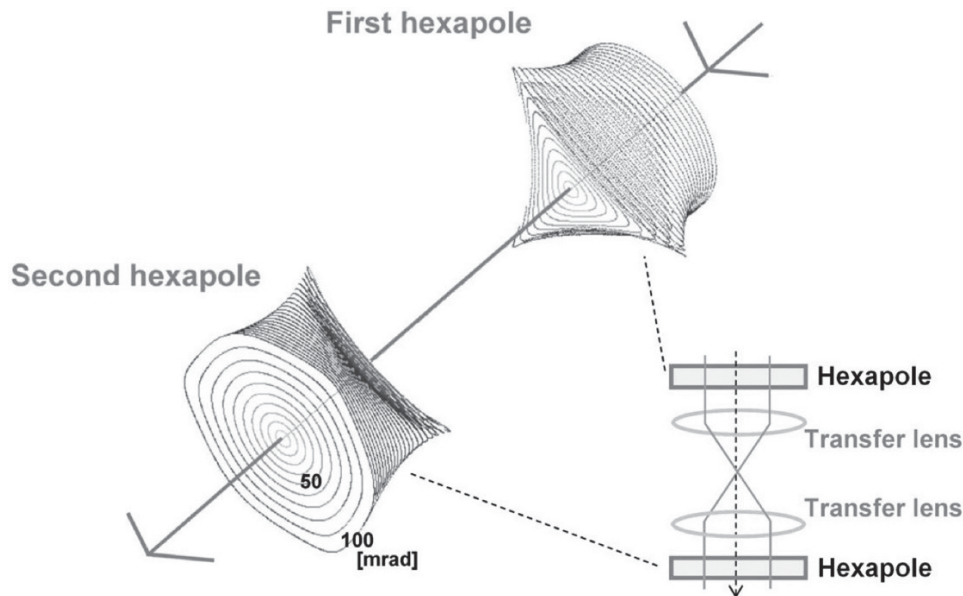


Figure 2.12 Configuration of the double-hexapole corrector and the beam shapes at first and second hexapole, reproduced from reference [9].

2.2.3 Imaging System and Z-Contrast Images

Electrons will interact with the nucleus and electron cloud when they travel through the specimen. Figure 2.13 shows the trajectories of the electrons interacting with the specimen. Inelastic and elastic scattering can happen during the interaction. Electrons usually lose a certain amount of energy in the inelastic process and generate X-rays or secondary electrons. In contrast, in the elastic process, electrons retain their kinetic energy and change their trajectory with an angle.

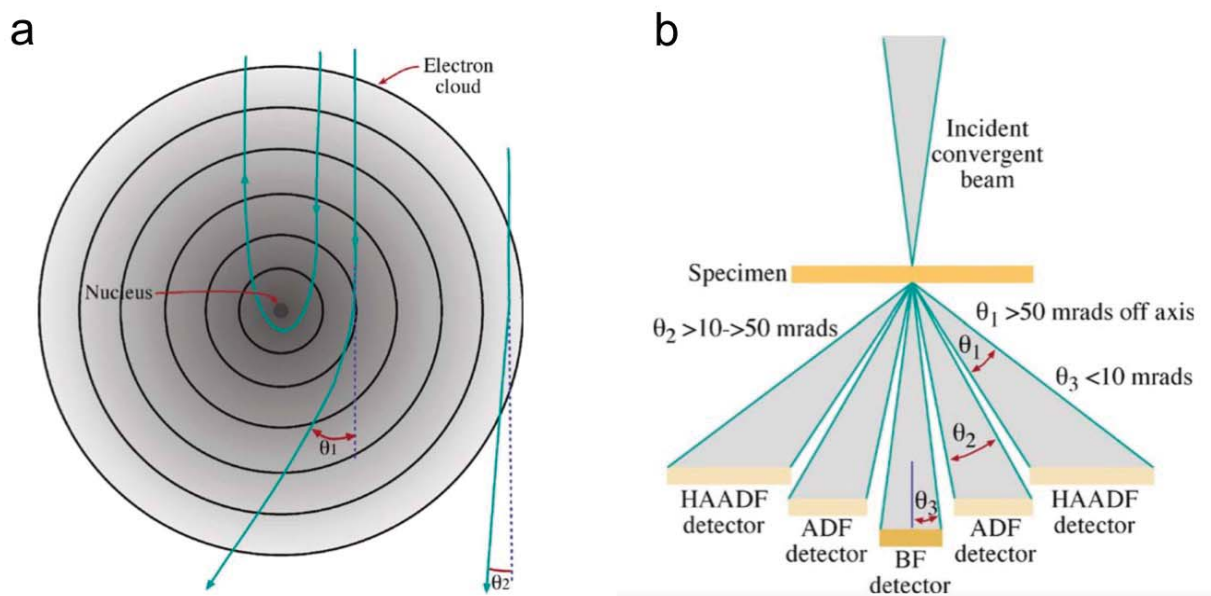


Figure 2.13 Schematic diagram of (a) high angle (θ_1) and low angle (θ_2) elastic scattering, and (b) detector setup in STEM, reproduced from reference [5].

In STEM, there are bright field (BF) detector and dark field (DF) detector corresponding to BF image and DF image (Figure 2.13b). The BF detector only collects the electrons directly passing through the specimen, while the annual DF detector collects scattered electrons. In our STEM, a high angle annular dark field (HAADF) detector is used to collect the high angular incoherent elastically scattered electrons to form HAADF image. In HAADF image which is also known as Z-contrast image, the intensity is proportional to Z^n ($n < 2$), where Z is the atomic number and n is an index determined by each STEM.

The “Z-contrast” is derived from the Rutherford scattering model. If the high-angle scattering comes from the electron-nucleus interaction alone, also known as Rutherford scattering, the differential cross section of the scattering can be written as:

$$\sigma_R(\theta) = \frac{e^4 Z^2}{16(4\pi\epsilon_0 E_0)^2 \sin^4 \frac{\theta}{2}} d\Omega, \quad (2.6)$$

in which, θ is the scattering angle, Z is the atomic number of the nucleus, Ω is the solid angle of scattering, E_0 is the energy of the electron, and ε_0 is the dielectric constant. Here the electron-electron cloud interaction (the screening effect) is not taken into consideration. If we consider the screening effect, equation 2.6 can be modified as:

$$\sigma_R(\theta) = \frac{Z^2 \lambda_R^4}{64\pi^4 a_0^2 \left[\sin^2 \frac{\theta}{2} + \left(\frac{\theta_0}{2} \right)^2 \right]^2} d\Omega, \quad (2.7)$$

here, λ_R , a_0 and θ_0 are the relativistically corrected electron wavelength, Bohr radius, and screening effect parameter, respectively, which are as below:

$$\lambda = \frac{h}{p} = \frac{h}{\left[2m_0 eV \left(1 + \frac{eV}{2m_0 c^2} \right) \right]^{1/2}}, \quad (2.8)$$

where m_0 is the rest mass of the electron, V is the acceleration voltage, h is the Plank constant, and c is the speed of light,

$$a_0 = \frac{h^2 \varepsilon_0}{\pi m_0 e^2}, \quad (2.9)$$

$$\theta_0 = \frac{0.117Z^{1/3}}{E_0^{1/2}}. \quad (2.10)$$

If we combine equation 2.7 and equation 2.10, it can be seen that $\sigma_R(\theta)$ is proportional to Z^α , where α is less than 2.

The HAADF detector is designed to collect the electrons with a scattering angle > 50 mrad ($\sim 3^\circ$). In our STEM, the inner and outer collection angles of the HAADF detector are 62 mrad and 164 mrad, respectively.

Due to the incoherent nature of Rutherford scattered electrons, there is no phase relationship in between, and the contrast of HAADF image solely depends on Z . According to equation 2.7,

the HAADF intensity relationship of two clusters composed of two different elements (a and b) can be written as:

$$\frac{I_a}{I_b} = \frac{n_a}{n_b} * \left(\frac{Z_a}{Z_b}\right)^\alpha, \quad (2.11)$$

where I represents the integrated HAADF intensity, n is the number of the atoms in a cluster, and α is the parameter determined by the collection angle of HAADF detector. The α in our STEM is 1.46 ± 0.18 calculated from experimental measurement [10].

2.3 Electrochemical Measurement

Full cyclic voltammograms (CV) or linear sweep voltammograms (LSV) are the standard techniques to evaluate the performance of an electrochemical catalyst. In CV or LSV measurement, a varying amount of energy is supplied by circulating a range of potential to drive the reaction, meanwhile, the reaction current is measured. The standard for a good catalyst is that a high reaction current can be produced with a small potential over the thermodynamic minimum. The electrochemical measurements were conducted by Daniel Escalera Lopez (PhD student from Chemical Engineering, UoB) and were carried out with a three-electrode set-up. It consists of a reference electrode (Saturated Calomel Electrode, SCE), a Pt mesh counter electrode and a working electrode terminated by a 5 mm wide, 2-3 mm thick glassy carbon.

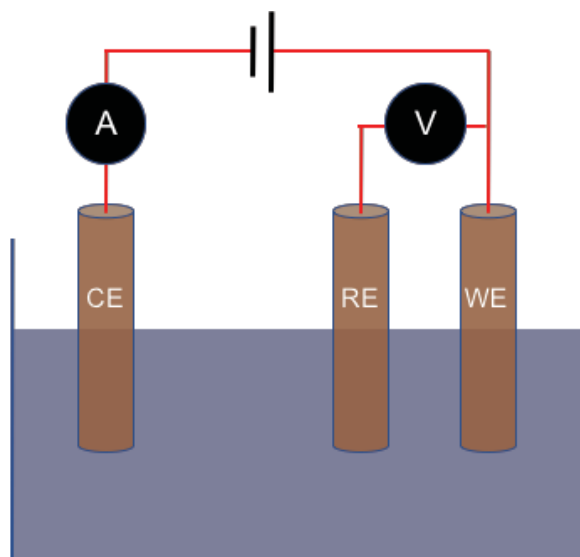


Figure 2.14 Schematic of a standard three-electrode set-up. It consists of a working electrode (WE), a reference electrode (RE) and a counter electrode (CE).

A schematic of three-electrode set-up for electrochemical measurements is shown in Figure 2.14. The working electrode is the support of the clusters and normally made of inert but conductive material (e.g. glassy carbon) to minimise the background reactivity. In order to accurately measure calculate the potential of the working electrode, a reference electrode with stable redox potential is necessary. Several kinds of reference electrodes are available for electrochemical measurements, like Standard Hydrogen Electrode (SHE), Saturated Calomel Electrode (SCE), silver chloride electrode, and et al. Here, the reference electrode is a Saturated Calomel Electrode based on the reaction between mercury and mercury chloride. The counter electrode is a platinum mesh electrode which oxidises hydrogen to balance the redox reaction at the working electrode. In order to study the kinetics of the catalytic reaction, an electrolyte with low proton concentration is needed to realise a mass transport limited state. The electrolyte used here is the freshly prepared solution with ultrapure water containing 2mM HClO_4 , 0.1M NaClO_4 .

In LSV measurement, the standard for an excellent catalyst is to produce high current density (j) with a small potential over the thermodynamic minimum (overpotential, η). The onset potential, the overpotential at which the reaction current is observed, is an important metric to evaluate a catalyst [11]. However, the ambiguity of the definition on onset potential makes it rather difficult to compare the results from different researchers. The current density value for onset potential could vary from 0.05 mA cm^{-2} to 5 mA cm^{-2} . The more popular metric is the overpotential value located at the current density of 10 mA cm^{-2} , which rose up from solar water splitting [12, 13]. The Tafel slope is an essential metric to address the catalytic mechanism, which can be obtained from the slop analysis of Tafel plot (overpotential vs. $\log j$). Exchange current density is another metric to represent the total electrode activity. It is the current density in the absence of other critical information and at zero overpotential and can be reached from the Tafel equation. An example graph of LSV and Tafel plot of two theoretical catalysts is shown in Figure 2.15. The two catalysts require the same overpotential for reaching the current density of 10 mA cm^{-2} . However, they present different onset potentials. The one in red has a much larger onset potential than the one in blue. The Tafel plot indicates two different HER mechanisms in the two catalysts. A lower Tafel slope is found with the catalyst in red, which means a smaller amount of potential is needed to increase a certain amount of exchange current density.

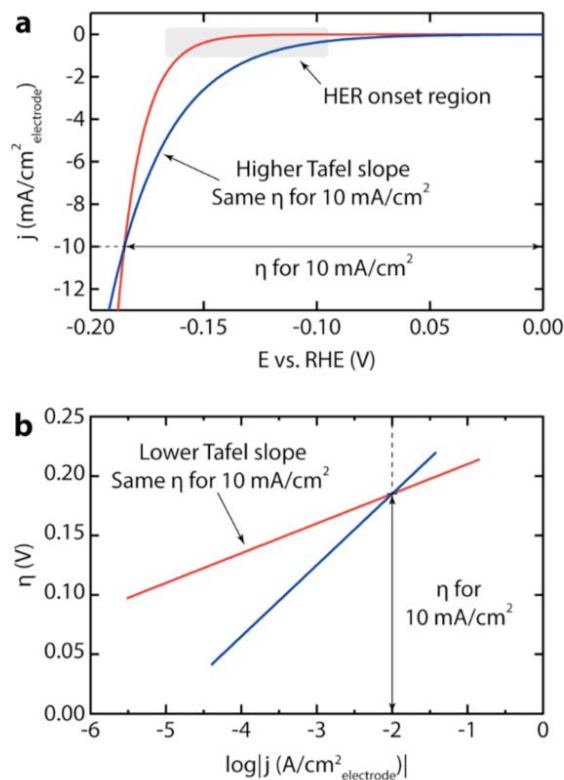


Figure 2.15 An example graph of LSV (a) and Tafel plot (b) based on two theoretical catalysts, reproduced from reference [11].

2.4 Micro-reactor

The term “micro-reactor” here means a chemical reactor with micrometre range dimensions used for analysing chemical reactions and surface science. Generally, the discovery, characterisation and optimisation of catalysts are viewed as the basic steps for developing new catalytic process. Before the emergence of micro-reactor, macroscale reactor was used to fulfil these steps in heterogeneous catalysis. Compared with the traditional macroscale reactor, micro-reactor has shown a series of advantages. Due to the small dimensions of micro-reactor, the mass transfer is improved, and the concentration gradients are reduced, the reaction parameters (pressure and gas flow rate) are easy to tune. The heat transfer at the reaction area

is also enhanced by the high surface to volume ratio, which makes it possible to control the reaction temperature accurately.

Figure 2.16 illustrates a micro-reactor used in this study for CO oxidation, which is designed and fabricated by Ib Chorkendorff's group at Technical University of Denmark (DTU). The micro-reactor with a microchannel system is fabricated on a silicon chip by reactive ion etching and deep reactive ion etching techniques.[14, 15] It has a 16 by 20 mm² surface area with a thickness of 350 μm. There are two inlets (I1, I2), two outlets (O1, O2), a mixing channel and a reaction zone. The reactant gas introduced from I1 and I2 fully mix in mixing channel, then either go to O1 or go to the reaction zone. After reaction occurs in the reaction zone, the gas containing products proceeds to O2 which is connected to quadrupole mass spectrometer (QMS), so the composition of the entire gas can be analysed.

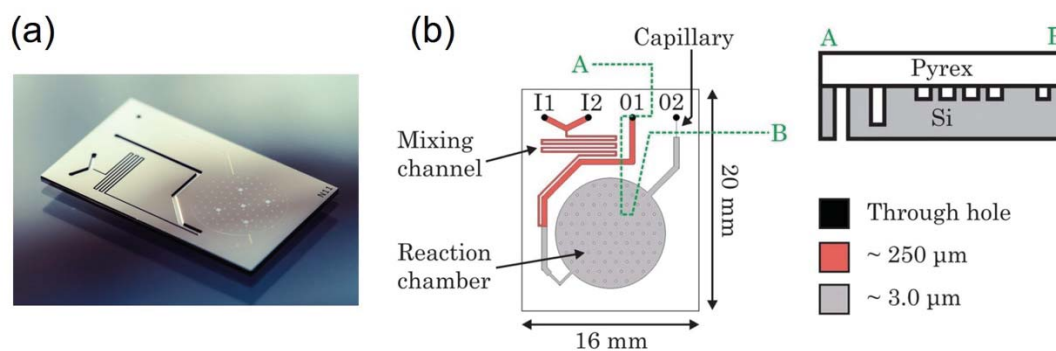


Figure 2.16 (a) A photograph of micro-reactor and (b) a schematic diagram of the design of microreactor, reproduced from reference [15].

Anodic bonding is used to seal the micro-reactor with Pyrex glass lid, and this can ensure the micro-reactor working properly at a pressure between 0.1 to 5.0 bar [16]. Because of the high sensitivity of the micro-reactor, it becomes a versatile tool for many fundamental studies of

model catalytic reactions, especially for the studies of size effects and catalytic activities of size-selected clusters.

2.5 Other Techniques

2.5.1 X-ray Photoelectron Spectroscopy

X-ray photoelectron spectroscopy (XPS) was developed by Kai Siegbahn in the 1960's. It has been widely used in surface characterization for elemental composition, oxidation states, and electronic structures. The basic principle of XPS is concerned with the photoelectric effect [17, 18]. As shown in Figure 2.17, when the sample surface is irradiated by a focused X-ray with energy $h\nu$ (e.g. Mg- $K\alpha$: 1253.6 eV), the electron in the sample will be ejected out. The kinetic energies E_k of the ejected photoelectrons are then analysed by electron spectrometer and recorded by the detector. The binding energy E_b is a characteristic parameter of the element, which can be used to retrospect its atomic energy level and parent element. The binding energy of a photoelectron can be calculated from the following equation [17]:

$$E_b = h\nu - E_k - W, \quad (2.12)$$

where W is the work function dependent on both the spectrometer and the material, which is characteristic to the specific system.

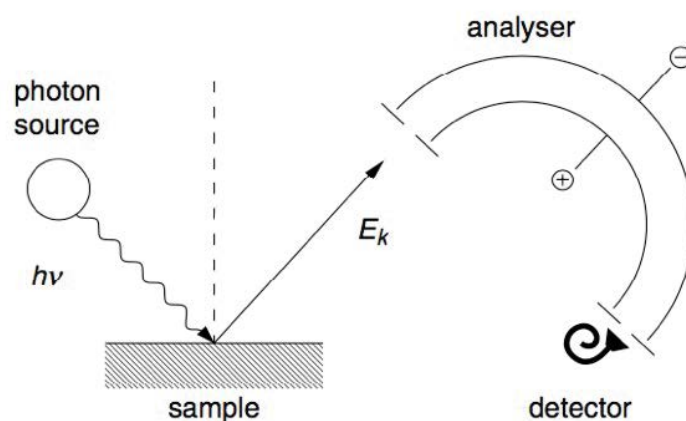


Figure 2.17 Schematic of X-ray photoelectron spectroscopy, reproduced from reference [19].

The principle is to generate and analyse the photoelectrons with kinetic energy E_k by a focused X-ray with energy $h\nu$.

In order to quantitatively determine the elemental information of materials, a narrow energy distribution of X-rays is necessary. This can be obtained by bombarding specific metals with high energy electrons. Normally, Al and Mg are used in the X-ray sources with characteristic energies of 1248.63 eV and 1253.6 eV, respectively [20]. In Modern XPS, a monochromator is usually introduced to obtain monochromatic X-rays.

2.5.2 Low Energy Ion Scattering

Low energy ion scattering (LEIS), sometimes referred to ion scattering spectroscopy (ISS), is a surface-sensitive analytical technique used to characterise the outermost layer of materials. The principle of LEIS is illustrated in Figure 2.18, which is based on binary collisions of the noble ion and the surface atoms of materials. An incident noble gas ion (He^+ , Ne^+ , Ar^+ or Kr^+) with mass m_1 and energy E_i (1-8 keV) is elastically scattered by the surface atom with mass m_2 in an angle of θ . The energy of the scattered ion (E_f) can be expressed as [21]:

$$E_f = \left[\frac{\cos \theta + \sqrt{\left(\frac{m_2}{m_1}\right)^2 - (\sin \theta)^2}}{1 + \frac{m_2}{m_1}} \right]^2 \times E_i, \text{ if } \frac{m_2}{m_1} \geq 1. \quad (2.13)$$

During the measurement, θ is set by the instrument. Then, the mass of the surface atom (m_2) can be derived by measuring E_f . A significant percentage of the noble ions can penetrate the first atomic layer of the sample surface and then neutralised, so that they won't be detected by

the analyser. This means LEIS owns a high surface sensitivity by detecting the outmost atomic layer of the surface.

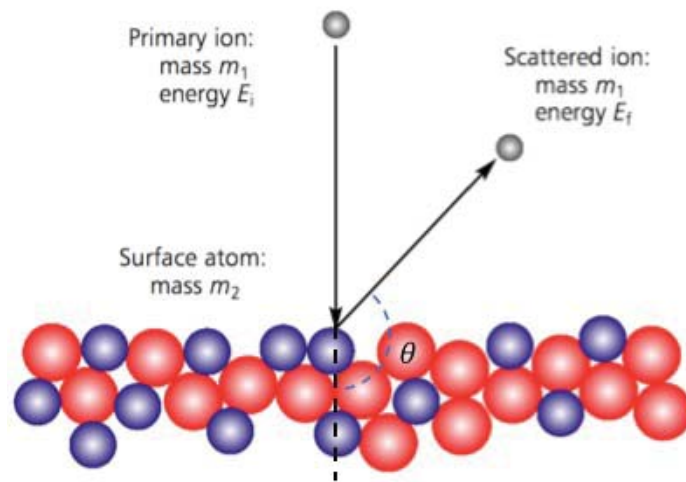


Figure 2.18 Schematic of the principle of low energy ion scattering, reproduced from reference [22]. The incident noble gas ion with mass m_1 and energy E_i (1-8 keV) is elastically scattered by the surface atom with mass m_2 . By analysing the energy of the scattered ion (E_f), m_2 can be derived.

References

- [1] Haberland H, Karrais M, Mall M, Thurner Y. Thin-films from energetic cluster impact: a feasibility study. *Journal of Vacuum Science & Technology a-Vacuum Surfaces and Films* **1992**, 10(5): 3266-3271.
- [2] Von Issendorff B, Palmer RE. A new high transmission infinite range mass selector for cluster and nanoparticle beams. *Rev. Sci. Instrum.* **1999**, 70(12): 4497.
- [3] Crewe AV, Wall J, Welter LM. A high-resolution scanning transmission electron microscope. *J. Appl. Phys.* **1968**, 39(13): 5861-&.
- [4] Varela M, Lupini AR, Benthem Kv, Borisevich AY, Chisholm MF, Shibata N, *et al.* Materials characterization in the aberration-corrected scanning transmission electron microscope. *Annual Review of Materials Research* **2005**, 35(1): 539-569.
- [5] David B. Williams, Carter CB. Transmission electron microscope a textbook for materials science. **2009**.
- [6] Krivanek OL, Dellby N, Spence AJ, Camps RA, Brown LM. Aberration correction in the STEM. *Electron microscopy and analysis*, **1997**, 35-40.
- [7] Krivanek OL, Dellby N, Lupini AR. Towards sub-angstrom electron beams. *Ultramicroscopy* **1999**, 78(1-4): 1-11.
- [8] Haider M, Uhlemann S, Schwan E, Rose H, Kabius B, Urban K. Electron microscopy image enhanced. *Nature* **1998**, 392(6678): 768-769.
- [9] T. N. Scanning transmission electron microscopy of nanomaterials: basics of imaging and analysis. *World Scientific* **2014**.
- [10] Wang ZW, Palmer RE. Intensity calibration and atomic imaging of size-selected Au and Pd clusters in aberration-corrected HAADF-STEM. *Journal of Physics: Conference Series* **2012**, 371: 012010.

- [11] Benck JD, Hellstern TR, Kibsgaard J, Chakthranont P, Jaramillo TF. Catalyzing the hydrogen evolution reaction (HER) with molybdenum sulfide nanomaterials. *ACS Catalysis* **2014**, 4(11): 3957-3971.
- [12] Benck JD, Chen Z, Kuritzky LY, Forman AJ, Jaramillo TF. Amorphous molybdenum sulfide catalysts for electrochemical hydrogen production: insights into the origin of their catalytic activity. *Acs Catalysis* **2012**, 2(9): 1916-1923.
- [13] Chen Z, Cummins D, Reinecke BN, Clark E, Sunkara MK, Jaramillo TF. Core-shell MoO₃-MoS₂ nanowires for hydrogen evolution: a functional design for electrocatalytic materials. *Nano Lett.* **2011**, 11(10): 4168-4175.
- [14] Hynes AM, Ashraf H, Bhardwaj JK, Hopkins J, Johnston I, Shepherd JN. Recent advances in silicon etching for MEMS using the ASE (TM) process. *Sensors and Actuators a-Physical* **1999**, 74(1-3): 13-17.
- [15] Henriksen TR, Olsen JL, Vesborg P, Chorkendorff I, Hansen O. Highly sensitive silicon microreactor for catalyst testing. *Rev. Sci. Instrum.* **2009**, 80(12): 124101.
- [16] Wallis G, Pomerant. Di. Field assisted glass-metal sealing. *Journal of Applied Physics* **1969**, 40(10): 3946-&.
- [17] Watts JF, Wolstenholme J. An introduction to surface analysis by xps and aes. *Wiley-VCH* **2003**.
- [18] Muilenberg G. Handbook of X-ray photoelectron spectroscopy. *Perkin-Elmer Corporation* **1979**: 64.
- [19] Reinert F, Hüfner S. Photoemission spectroscopy: from early days to recent applications. *New Journal of Physics* **2005**, 7: 97-97.
- [20] Chorkendorff I, Niemantsverdriet JW. Concepts of modern catalysis and kinetics. *John Wiley & Sons*, **2017**.

- [21] Cushman CV, Brüner P, Zakel J, Major GH, Lunt BM, Smith NJ, *et al.* Low energy ion scattering (LEIS): a practical introduction to its theory, instrumentation, and applications. *Anal. Methods* **2016**, 8(17): 3419-3439.
- [22] Brongersma HH, Grehl T, Schofield ER, Smith RAP, Ter Veen HRJ. Analysis of the outer surface of platinum-gold catalysts by low-energy ion scattering. *Platinum Met. Rev.* **2010**, 54(2): 81-87.

Chapter 3

Atomic Structures and HER Activities of MoS₂ Clusters and Ni-MoS₂ clusters

The work in this chapter is represented in the publication of “Escalera-López D, Niu Y, Yin J, Cooke K, Rees NV, Palmer RE. Enhancement of the hydrogen evolution reaction from Ni-MoS₂ hybrid nanoclusters. *ACS Catalysis* 2016, 6(9): 6008-6017” [1]. The draft of the published paper was written by me and Daniel Escalera Lopez. I was in charge of the cluster fabrication and STEM analysis, and Daniel Escalera Lopez was in charge of the XPS analysis HER analysis. Most of the text, figures and tables in this chapter are the replica from the publication.

3.1 Introduction

Two-dimensional transition metal dichalcogenides (TMD) have attracted renewed attention since the isolation of graphene [2-4]. Molybdenum disulphide (MoS₂), as a representative member of the TMD family and an earth-abundant material, has been widely investigated because of its intriguing catalytic [5, 6], electronic [7-9], optoelectronic [10], and tribological [11] properties. MoS₂ layers have a sandwich structure with molybdenum atoms arranged between two sulphur sheets [8, 12, 13]. In nanoparticles (NPs), the atoms at the edge sites of the MoS₂ layers, rather than the basal plane atoms, make the main contribution to the catalytic activity [6, 14]. Nanostructured MoS₂ materials have a highly rated prospect as a substitution

of the scarce and costly platinum group metals in catalysis. Intensive research has been conducted since the discovery of the linear relationship of the hydrogen evolution reaction (HER) activity and the number of MoS₂ edge sites [14]. In the case of MoS₂, the focus is on maximizing the proportion of active edge sites and minimizing the in-plane/through-plane charge transfer resistance by the development of single-layered nanoplatelets [15], nanowires [16], mesoporous structures [17] and nanocomposites with highly conductive supports [18].

There are two kinds of edge sites, Mo-edge and S-edge, and only the Mo-edge sites are active to HER due to their near-zero hydrogen adsorption free energy ($\Delta G_{\text{H}} = 0.06$ eV) [19]. Several methods have been proposed to enhance the HER activity, one promising way is to dope the S-edge sites with transition metal (TM) (Fe, Co, Ni) to activate their HER activity by shifting the ΔG_{H} value closer to $\Delta G_{\text{H}} = 0$ (thermo-neutral) [20]. Experiments on MoS₂ nanoparticles and MoS₃ thin films reported a HER enhancement upon non-selective edge doping [21, 22] and later tests on edge-terminated MoS₂ nanofilms demonstrated the 2-fold (in the case of Cu dopant) and almost 3-fold (for Fe, Co, Ni) HER enhancement observed with the activation of the S-edge sites [23]. Nevertheless, TM-doping of MoS₂ nanoparticles is scarcely reported probably due to the difficulty in separating the effects of surface area and morphology changes from the electrocatalytic enhancement [24, 25].

Lamellar MoS₂ NPs, prepared by magnetron-sputtering and gas condensation to create clusters in the gas phase prior to the deposition, are excellent candidates for TM-doping due to their narrow size-distribution and the present ability to control the stoichiometry in the cluster beam source [5]. Here we explored the catalytic activity of Ni-MoS₂ as a representation of TM-doped MoS₂ NPs prepared via a dual-magnetron sputtering and gas condensation deposition technique. Pristine MoS₂ clusters, Ni clusters and Ni-MoS₂ hybrid clusters are prepared to evaluate their electrocatalytic activity to HER. The term “MoS₂” used in this thesis means the general MoS₂-based clusters, and it does not necessarily mean the stoichiometry of Mo and S

is 1:2. Because the clusters produced from cluster beam deposition have the same layered structure with the MoS₂ (Mo:S = 1:2) materials reported in the literatures, we call them MoS₂ clusters in this research.

3.2 Materials and Methods

MoS₂, Ni and hybrid Ni-MoS₂ clusters were prepared using a custom-built cluster beam source at Teer Coatings Ltd (Worcestershire, UK). The system layout is shown in Figure 3.1. The clusters are generated within the first section of the source by sputtering with dual, independent magnetrons and gas condensation. After leaving the magnetron sputtering chamber via a small nozzle (5 mm in diameter), clusters with a positive charge are accelerated and steered by the ion optical electrostatic lenses which guide the beam in the second vacuum chamber. In the next step, the ion beam is focused and directed into the third vacuum chamber for mass selection. By using the Time-of-Flight mass filter, the mass distribution of clusters can be monitored in real time. The cluster size is tuned by varying the sputtering power, gas flux and condensation length. When the desired cluster size distribution within the sampled ion beam is achieved, the high voltages applied to the deflector in the centre of the Ion Optics chamber are switched to a deflection mode, so that the positively ionised fraction of the cluster beam is deflected horizontally towards the deposition chamber. Glassy carbon (GC) stubs (5 mm x 5 mm x 3 mm, mirror finish) are mounted on a carousel, which can be rotated and also translated vertically. The rotation speed of the carousel and its vertical motion are carefully controlled to ensure an even cluster distribution on the substrates. For all the samples, an average cluster spacing of 2.5 nm was targeted. According to this cluster spacing and the mass spectra, the mass loadings are 1.28 $\mu\text{g}/\text{cm}^2$, 3.45 $\mu\text{g}/\text{cm}^2$, and 4.25 $\mu\text{g}/\text{cm}^2$ for Ni, MoS₂ and hybrid Ni-

MoS₂ clusters, respectively. A high voltage bias is applied to the carousel in order to control the impact energy of the clusters landing on the support.

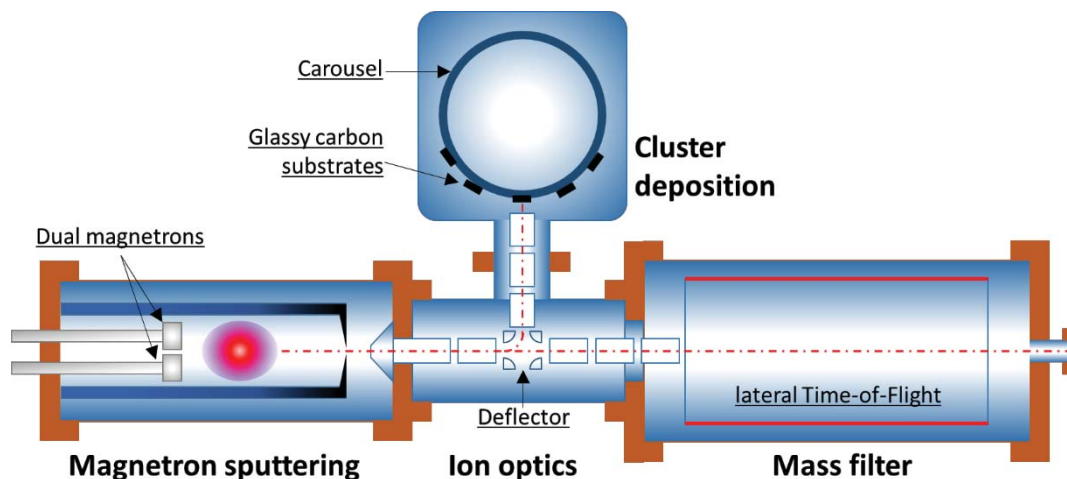


Figure 3.1 Schematic of the cluster beam system (top view). It consists of four sections: magnetron sputtering, ion optics, mass filter and cluster deposition. Note that in the described experiments, the mass filter is only used for cluster size monitoring, not for deposition. The clusters are instead deposited directly onto substrates in the chamber shown at the top of the figure.

During the cluster deposition, a condensation length (i.e. the distance between the sputtering target surface and the exit nozzle) of 24 cm was used and a pressure of approximately 0.23 mbar was maintained in the condensation chamber, with 70 standard cubic centimetres per minute (sccm) argon flow and 10 sccm helium flow. In the preparation of pure MoS₂ or Ni clusters, only the magnetron sputtering source fitted with the respective target (MoS₂ or Ni) was operated, while the other magnetron's power supply was switched off. For the deposition of Ni-doped MoS₂ clusters, the two magnetrons were operated simultaneously.

Clusters were deposited on TEM grids covered with amorphous carbon films for STEM characterization. The clusters were imaged with a 200kV aberration-corrected STEM (JEOL 2100F) in the HAADF mode, and Energy Dispersive X-ray spectroscopy (EDX) was also performed to analyse the elemental composition. X-ray photoelectron spectroscopy (XPS) was performed by Aston university on a Kratos Axis His X-ray photoelectron spectrometer fitted with a charge neutralizer and magnetic focusing lens employing Mg K α achromatic radiation (1253.6 eV).

Electrochemical measurements of HER activity were carried out by Daniel Escalera Lopez in a thermostatted three-electrode electrochemical cell (295 \pm 2 K) with a PC-controlled PGSTAT128N potentiostat (Metrohm Autolab B.V, Netherlands). The electrodes used were a saturated calomel (SCE) reference electrode (BAS Inc, Japan), a bright Pt mesh counter electrode (Alfa Aesar Ltd, UK) and 5mm diameter, 3 mm thick GC type 2 stubs (Alfa Aesar, UK) modified with either pure Ni or Ni-doped/undoped MoS₂ clusters as working electrodes.

All experiments were performed in a 2mM HClO₄, 0.1M NaClO₄ solution (pH 2.70), freshly prepared with ultrapure water (resistivity not less than 18.2 M Ω cm, Millipore Milli-Q Direct 8). Deoxygenation was achieved by vigorous N₂ bubbling prior to each electrochemical experiment and maintained under positive N₂ pressure. This electrolyte was chosen in contrast to other electrolytes more commonly reported in the literature for hydrogen evolution experiments (0.5M H₂SO₄, pH \approx 0.3; 0.1M HClO₄, pH \approx 1) due to the non-coordinating nature of the perchlorate anion being likely to yield more reproducible results and enable a more accurate elucidation of the reaction kinetic parameters. The modified electrodes were preconditioned with 10 cycles between -0.045 and -1.645 V vs. SCE at a scan rate of 50 mVs⁻¹. Electrochemical measurements were made at a range of voltage scan rates from 2 to 1200 mVs⁻¹.

3.3 Structure and Composition Analysis of the Clusters

The time-of-flight mass filter enabled the mass of clusters formed in the sputtering chamber to be monitored before deposition onto the GC stubs. Figure 3.2 shows the mass spectra of the samples employed in the HER measurements. During the preparation of pure MoS₂ samples, a sputtering power of 8W was applied to the MoS₂ target and a peak mass of 4.8×10^4 amu, equivalent to (MoS₂)₃₀₀, was found in the mass spectra (300 being the number of MoS₂ units contained in one MoS₂ cluster). The pure Ni sample was prepared similarly, and a resulting Ni peak mass of 1.3×10^5 amu, equivalent to ~Ni₂₂₀₀, was found (2200 being the number of Ni atoms in one Ni cluster). When the sputtering power for the Ni target was changed from 4W to 8W, the peak mass shifted from 6×10^4 amu to 1.3×10^5 amu, and the peak beam current shifted from 11 pA to 90 pA. Thus, higher sputtering power on the Ni target generates more, and larger, Ni clusters. Consequently, a lower sputtering power of only 3W on the Ni target was used in the preparation of the hybrid Ni-MoS₂ clusters in order to avoid an excess of Ni clusters, while 8W of sputtering power was used on the MoS₂ target. The peak mass of the hybrid Ni-MoS₂ clusters was located at 1.6×10^5 amu, equivalent to a mass of (MoS₂)₁₀₀₀ (1000 equivalent MoS₂ units per Ni-MoS₂ cluster) or Ni₂₇₁₂ (2712 equivalent Ni atoms per Ni-MoS₂ cluster). In the following sections, we will refer to the Ni, MoS₂ and hybrid Ni-MoS₂ clusters as Ni₂₂₀₀, (MoS₂)₃₀₀ and (Ni-MoS₂)₁₀₀₀, respectively.

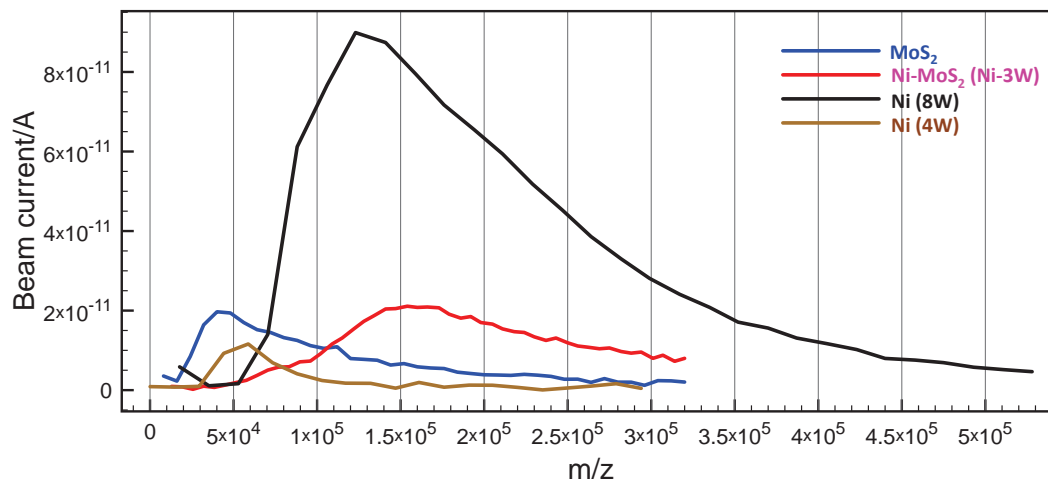


Figure 3.2 Mass spectra obtained by time-of-flight. From the spectra, MoS₂, Ni (8W) and Ni-MoS₂ (3W) show peak masses of around 4.8×10^4 amu ((MoS₂)₃₀₀), 1.3×10^5 amu (~Ni₂₂₀₀) and 1.6×10^5 amu [(MoS₂)₁₀₀₀], respectively. The mass spectra of Ni (4W) is also plotted to show the effect of the power applied to this target.

The STEM images in Figure 3.3 show (top to bottom) the morphologies of MoS₂ clusters, Ni-MoS₂ hybrid clusters and Ni clusters. A HAADF-STEM image is a Z-contrast image, meaning that the image intensity depends on the atomic number of elements, and in practice, the images are dominated by Mo atoms. The distinct intensity contrast across one MoS₂ cluster indicates an incomplete multi-layer structure (the HAADF-STEM intensity line profile analysis is shown in Figure 3.5). Ni-MoS₂ clusters present a broadly similar morphology to that of the pure MoS₂ clusters, while Ni clusters show a quite distinct crystalline structure. This implies that Ni is atomically added to the MoS₂ clusters when the hybrid Ni-MoS₂ clusters are formed. After fast Fourier transformation (FFT) analysis of STEM images in Figure 3.3 and comparison with the crystalline lattice parameters of MoS₂ polymorphs 1T and 2H no clear crystalline structure could be found on either MoS₂ or Ni-MoS₂ clusters. Based on the projected surface areas of more than 100 clusters of each kind, the average diameter distributions are shown in Figure

3.3. The peak values in the distributions for MoS₂ clusters, Ni-MoS₂ clusters and Ni clusters are 2.6 nm, 5.0 nm, and 4.2 nm respectively.

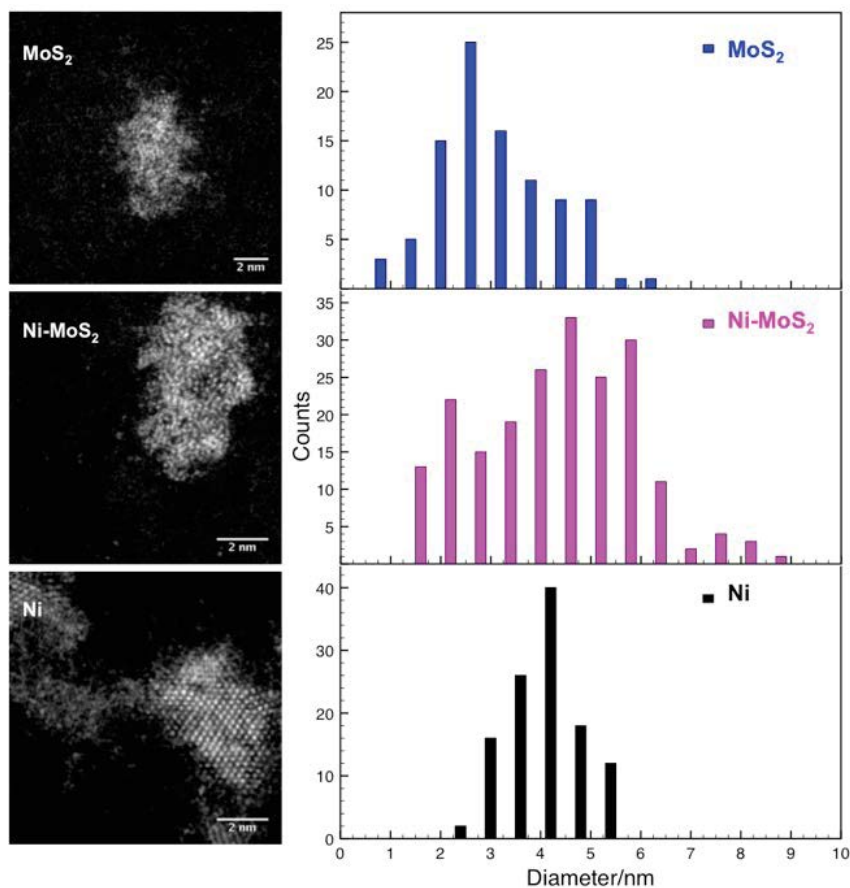


Figure 3.3 STEM images and size distribution in diameter based on the cluster surface area. MoS₂, Ni-MoS₂, and Ni (8W) have a peak value of 2.6 nm, 5.0 nm, and 4.2 nm respectively.

In order to confirm the existence of Ni in the hybrid Ni-MoS₂ clusters, EDX analysis was conducted, and the result is shown in Figure 3.4. Mo, S, and Ni signals are found in the same clusters, which indicate Ni-MoS₂ hybrid clusters were made successfully. The characteristic energy difference between the Mo L-edge and S L-edge is only 14 eV, which is smaller than the energy resolution of the EDX instrument (133 eV). Consequently, Mo and S signals cannot be distinguished by EDX, and the cyan dots in Figure 3.4b are due to the signal overlap of Mo

and S. Ni signals are found both in MoS₂ areas and between them, which means Ni might be located on or between MoS₂ clusters. Figures 3.4c to 3.4e display the individual elemental maps. Cluster shape mismatch between HAADF-STEM image shown in Figure 3.4a and Figures 3.4b to 3.4e is ascribed to STEM image drift during EDX measurement. Compared with the large clusters, the small cluster located at the bottom of each image is much less abundant in Ni, which is found primarily at MoS₂ edge sites and between clusters. During the formation process in the cluster source, small clusters may sometimes aggregate, being bonded to each in the gas condensation process to form big clusters. Generally, the big clusters contain more Ni atoms with random locations. Besides the signals found in the clusters (marked by the yellow shapes), signals can be found outside the clusters; these signals may come from small clusters originating from the deposition process or electron beam sputtering of the deposited clusters. Since Mo and S signals are overlapped with each other, the exact cluster compositions cannot be obtained from EDX analysis.

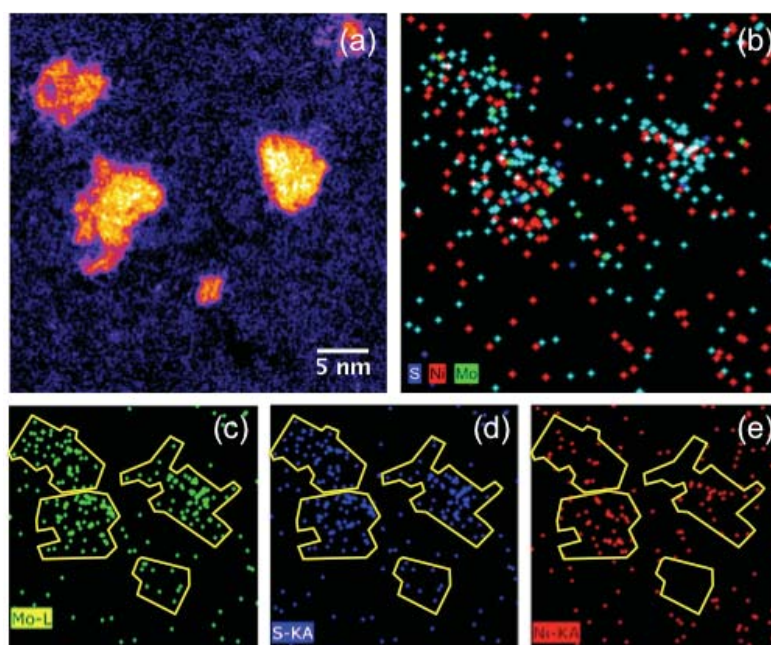


Figure 3.4 STEM image (a) containing large and small clusters used for EDX measurement. (b)EDX mapping shows the composition of Ni-MoS₂ clusters; Mo, S, and Ni are shown in

green, blue, and red respectively. The signal in cyan comes from the overlap of Mo and S signals. Mo, S, and Ni signals are also shown separately in panels c, d and e; where the cluster positions are marked by the yellow shapes.

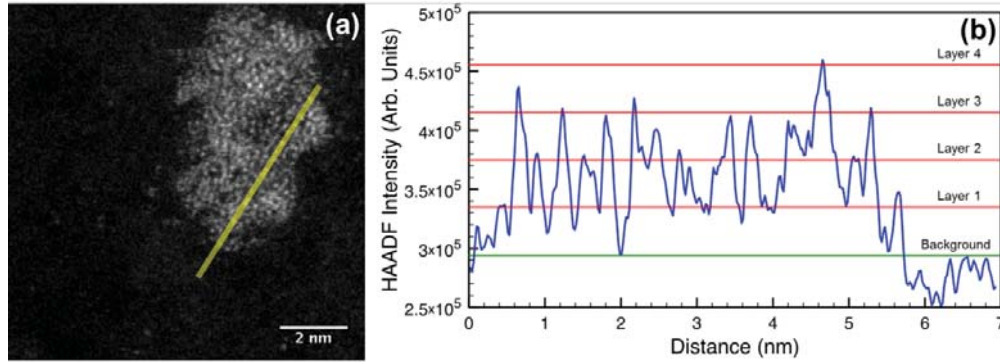


Figure 3.5 (a) STEM image of Ni-MoS₂ hybrid cluster and (b) example HAADF intensity line profile corresponding to the yellow region in (a). The line profile shows step changes in cluster height, and the layer numbers are labelled as a guide.

To identify the composition of the hybrid Ni-MoS₂ clusters, we employ a method based on atom counting and STEM intensity measurement. The HAADF intensity (I) of two kinds of elements (A and B) follows the relationship $I_A/I_B = (Z_A/Z_B)^{1.46}$, in which Z is the atomic number, for our microscope calibration [26]. Thus the intensity relationship between Mo, S and Ni can be expressed as below:

$$I_{Mo} = 4.09 \times I_S = 1.81 \times I_{Ni} \quad (3.1)$$

Since the single atom intensity of Mo is much higher than that of S and Ni, we assume the atoms most easily visible in STEM images are Mo. According to the intensity line profile shown in Figure 3.5, the number of Mo columns intersected by the line and the number of Mo atoms in each column can be obtained. Once all the surface area of the cluster is scanned by such lines, the total number of Mo atoms (N_{Mo}) is obtained. The number of S atoms (N_S) in this cluster can also be derived on the assumption that the ratio of Mo atoms to S atoms is 1:2.

Therefore the composition of the cluster can be regarded as (MoS₂)_{N_{Mo}}Ni_x. Now the integrated intensity of the whole cluster ($I_{cluster}$) can be given by:

$$(I_{Mo} \times N_{Mo}) + (I_S \times 2N_{Mo}) + (I_{Ni} \times x) = I_{cluster} \quad (3.2)$$

Since the intensity of the whole cluster can be measured from STEM image, against using a single Mo atom as the standard, the value of x can be given by combining equations 3.1 and 3.2:

$$x = \frac{1.81I_{cluster}}{I_{Mo}} - 2.67N_{Mo} \quad (3.3)$$

Then the cluster composition is revealed.

By this method, the compositions of six clusters of varying size were calculated and are listed in Table 3.1. The outcome is that there is no fixed ratio of Ni atoms to MoS₂ units in the hybrid clusters, but in general, the proportion of Ni increases with cluster size, which agrees with the EDX results.

Table 3.1 Composition analysis of six hybrid Ni-MoS₂ clusters based on HAADF-STEM images.

Ni-MoS ₂ cluster	Ratio of Ni atoms number to MoS ₂ units number
(MoS ₂) ₃₇₃ Ni ₂₂	0.06
(MoS ₂) ₃₇₈ Ni ₃₀	0.08
(MoS ₂) ₄₆₁ Ni ₇₂₀	1.56
(MoS ₂) ₈₄₄ Ni ₆₄₈	0.77
(MoS ₂) ₁₁₆₃ Ni ₁₂₃₅	1.06
(MoS ₂) ₁₄₅₈ Ni ₂₁₈₁	1.50

The chemical composition and oxidation state of the untested clusters deposited on TEM grids analyzed by STEM imaging were further characterized by XPS at Aston University. Detailed spectra in the Mo 3d and S 2p region for fresh and 14 h air-exposed (MoS₂)₃₀₀ are shown in Figure 3.6. One Mo 3d_{5/2} and Mo 3d_{3/2} spin-orbit doublet found at ~229.8 eV and ~232.9 eV in the fresh (MoS₂)₃₀₀ clusters, which is the characteristic of the Mo⁴⁺ oxidation state of MoS₂ materials [27]. After exposed in air for 14 h, an additional doublet at ~233.1 eV and ~236.2 eV related to the Mo⁶⁺ oxidation state found in MoO₃ [28] and an upward shift of ~0.4 eV in the Mo⁴⁺ components indicate an oxidation state increase in MoS₂ clusters. The fresh S 2p spectrum can be deconvoluted into two components at ~160.7 eV and ~161.9 eV corresponding to the spin-orbit S 2p_{3/2} and S 2p_{1/2} doublet characteristic of the S²⁻ oxidation state [29]. The additional broad signal at ~167 eV related to oxidised sulphur species such as sulfites or sulfates [30]. Quantification of the Mo⁴⁺:S²⁻ peak areas gives a Mo:S ratio of 1:0.90±0.02, which confirms the sulphur-deficient nature of (MoS₂)₃₀₀ clusters.

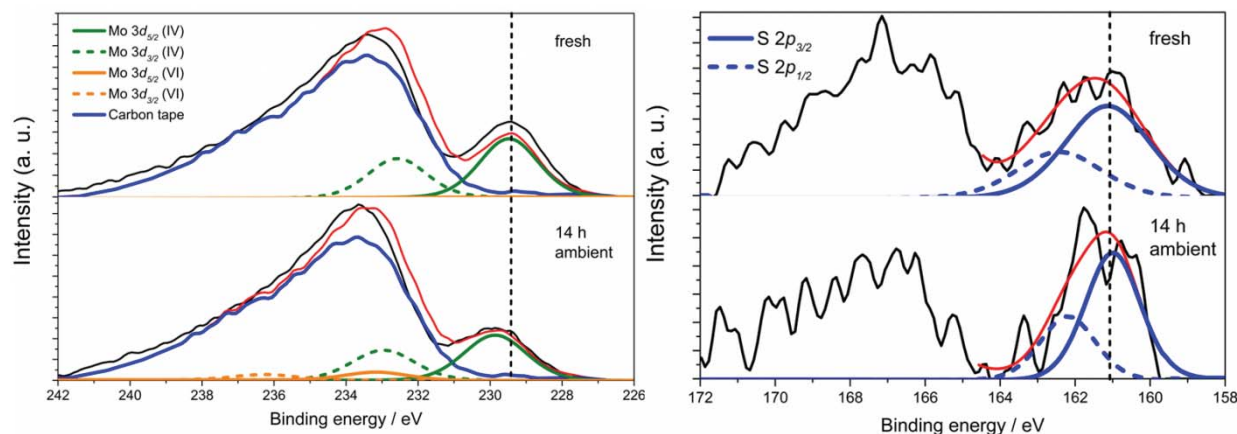


Figure 3.6 Detailed XPS spectra of Mo 3d (left) and S 2p (right) for fresh (top) and 14 h air exposed (bottom) (MoS₂)₃₀₀ clusters. Quantification of the Mo⁴⁺:S²⁻ peak areas gives a Mo:S ratio of 1:0.90±0.02. Labels: raw spectra (solid black), cumulative peak fit (solid red), Mo⁴⁺ 3d_{5/2} (solid green), Mo⁴⁺ 3d_{3/2} (dashed green), Mo⁶⁺ 3d_{5/2} (solid orange), Mo⁶⁺ 3d_{3/2} (dashed orange), S 2p_{3/2} (solid blue) and S 2p_{1/2} (dashed blue).

Detailed spectra in the Mo 3d and S 2p region for 14 h air-exposed (Ni-MoS₂)₁₀₀₀ are shown in Figure 3.7. Both Mo⁴⁺ oxidation state (~229.8 eV and ~232.9 eV) and Mo⁶⁺ oxidation state (~233.1 eV and ~236.2 eV) can be found in the fresh Mo 3d XPS spectrum. An upward shift of 0.2 eV in the Mo⁴⁺ and Mo⁶⁺ components after air exposure as well as a photoemission intensity increase of the latter doublet indicate an oxidation state increase in Ni-MoS₂ clusters. This is also supported by analysis of the Mo⁴⁺:Mo⁶⁺ XPS atomic photoemission percentages (at. %), which reveal a conversion of MoS₂ into MoO₃ from Ni-MoS₂ fresh samples (Mo⁴⁺/Mo⁶⁺ 78.1/21.9 at. %) to air exposed (Mo⁴⁺/Mo⁶⁺ 54.9/45.1 at. %). Quantification of the Mo⁴⁺:S²⁻ peak presents a Mo:S ratio of 1:1.8±0.1 in (Ni-MoS₂)₁₀₀₀ clusters, which is similar to the Mo:S ratio expected in MoS₂. Compared with (MoS₂)₃₀₀ clusters, such difference in the oxidation behaviour could be ascribed to the presence of surface Ni atoms prone to oxidation which would mitigate S²⁻ oxidation under ambient conditions. The lack of definition in the

spin-orbit S 2p_{3/2}:2p_{1/2} doublet found here had been previously ascribed in amorphous MoS₃ materials to the presence of mixed S²⁻/S₂²⁻ oxidation states,²⁵ but in our case it could be due either to the low photoemission counts due to low sample loading (~4 μg cm⁻²) or to the inherent amorphous nature of the MoS₂ clusters provided the S-deficiency of the samples.

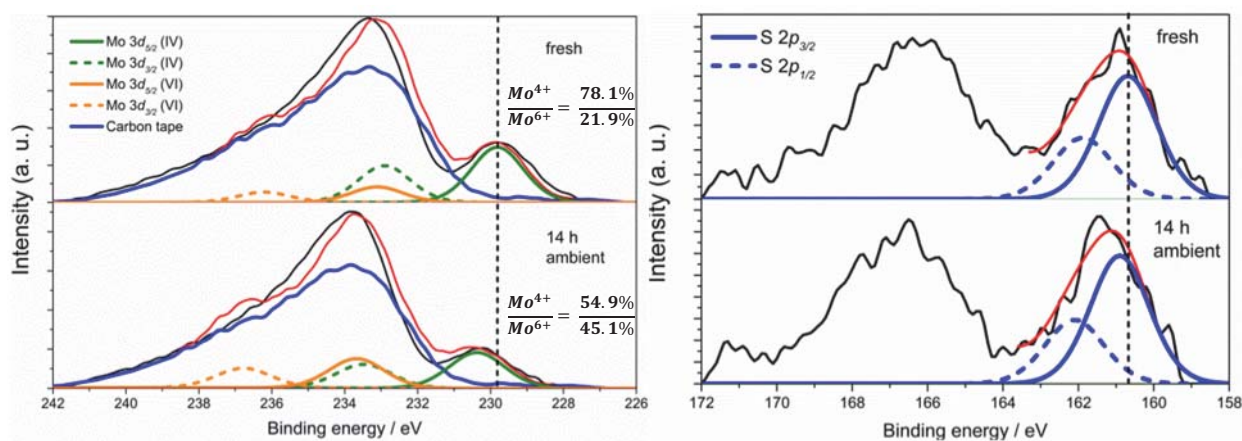


Figure 3.7 Detailed XPS spectra of Mo 3d (left) and S 2p (right) for fresh (top) and 14 h air exposed (bottom) (Ni-MoS₂)₁₀₀₀ clusters. Quantification of the Mo⁴⁺:S²⁻ peak presents a Mo:S ratio of 1:1.8±0.1. Labels: raw spectra (solid black), cumulative peak fit (solid red), Mo⁴⁺ 3d_{5/2} (solid green), Mo⁴⁺ 3d_{3/2} (dashed green), Mo⁶⁺ 3d_{5/2} (solid orange), Mo⁶⁺ 3d_{3/2} (dashed orange), S 2p_{3/2} (solid blue) and S 2p_{1/2} (dashed blue).

Analysis of the Ni 2p Detailed spectra of both Ni and Ni-MoS₂ clusters is paramount to evaluate the oxidation state of the Ni dopant atoms as well as to identify the presence of nickel species such as oxides and sulfides. Deconvolution of the Ni 2p_{3/2} component of the untested Ni clusters (Figure 3.8) shows the predominance of oxidized species such as NiO and Ni(OH)₂, with Ni:NiO:Ni(OH)₂ composition percentages practically invariable after air exposure (7.4:49.8:42.8 fresh, 6.6:51.2:42.2 air exposed). As for (Ni-MoS₂)₁₀₀₀ clusters shown in Figure 3.9, quantitative analysis of the Ni 2p region is not possible due to low signal-noise ratio ascribed to the low Ni content aimed during the cluster formation. The peak position of the Ni

2p_{3/2} component for the fresh (Ni-MoS₂)₁₀₀₀ samples at ~852.8 eV and the lack of clearly defined satellite signals seem to suggest predominance of metallic Ni (theoretical value: 852.7±0.4 eV) [31], but air exposure leads to an upward shift of the Ni 2p_{3/2} component to ~854eV, similar to the 854.6 eV characteristic of the NiO principal XPS peak [32] as well as in increase in the Ni 2p_{3/2} and Ni 2p_{1/2} satellite intensities (~861 and ~872.5 eV, respectively). This would indicate that under air exposure the doping Ni atoms spontaneously increase their oxidation state to Ni²⁺ as found in NiO species, agreeing with the behaviour observed for bare Ni clusters. Presence of a nickel sulfide phase cannot be discarded from XPS results as it is well reported that directly bonded S atoms leave the Ni 2p_{3/2} peak position unaltered [33], and the S 2p_{3/2}:2p_{1/2} doublet overlap commonly reported in nickel sulfides [34] is also found in the bare (MoS₂)₃₀₀ clusters. However, the upward shift of the Ni 2p_{3/2} component to binding energies similar to those of NiO species after air exposure makes the presence of a nickel sulfide phase unlikely. Thus, the Ni oxidation state conversion observed after 14 h air exposure will have significant repercussions in the electrocatalytic performance of the Ni-MoS₂ hybrid clusters.

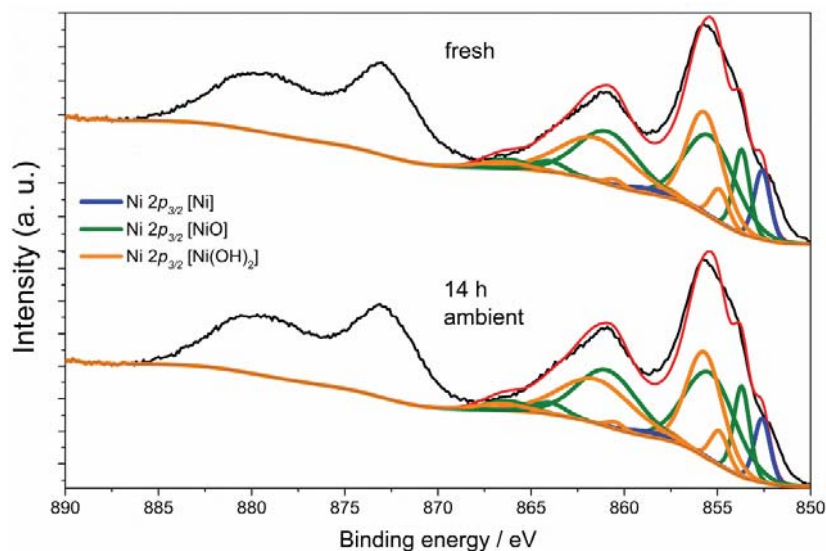


Figure 3.8 Detailed XPS spectra of Ni 2p fresh (top) and 14 h air exposed (bottom) Ni clusters. Labels: raw spectra (solid black), cumulative peak fit (solid red), Ni⁰ 2p_{3/2} peak deconvolution (solid blue), Ni²⁺ (NiO) 2p_{3/2} peak deconvolution (solid green) and Ni²⁺ [Ni(OH)₂] 2p_{3/2} peak deconvolution (solid orange).

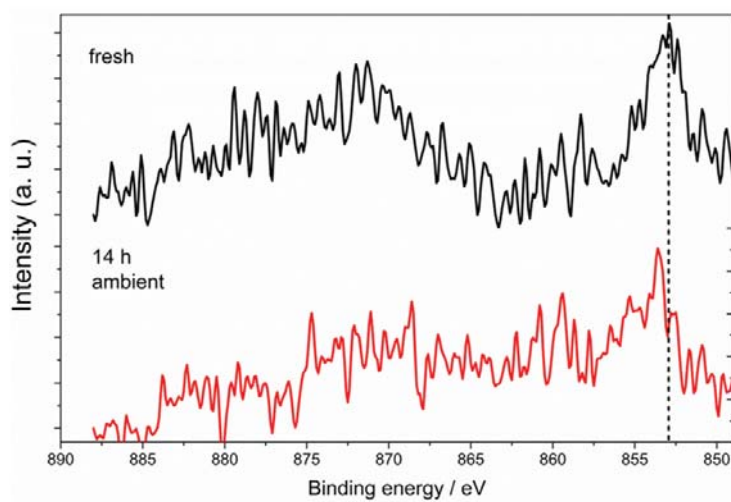


Figure 3.9 Detailed XPS spectra of Ni 2p for fresh (top, solid black) and 14 h air exposed (bottom, solid red) (Ni-MoS₂)₁₀₀₀ clusters. The dashed vertical line indicates peak position of metallic Ni (theoretical value: 852.7±0.4 eV).

3.4 Electrocatalytic Activity to HER

Figure 3.10 shows the linear sweep voltammograms acquired in the 0 to -1.2 V range [normalised vs. Normal Hydrogen Electrode (NHE)] at a scan rate of 25mVs⁻¹ in 2mM HClO₄/0.1M NaClO₄ aqueous electrolyte for all samples tested. A diffusion decay peak profile is observed in all samples due to the low proton concentration present in the electrolyte ($[H^+] \approx 2 \times 10^{-6} \text{ mol cm}^{-3}$), purposefully chosen to perform a better elucidation of the samples' kinetic parameters (Tafel slope analysis).

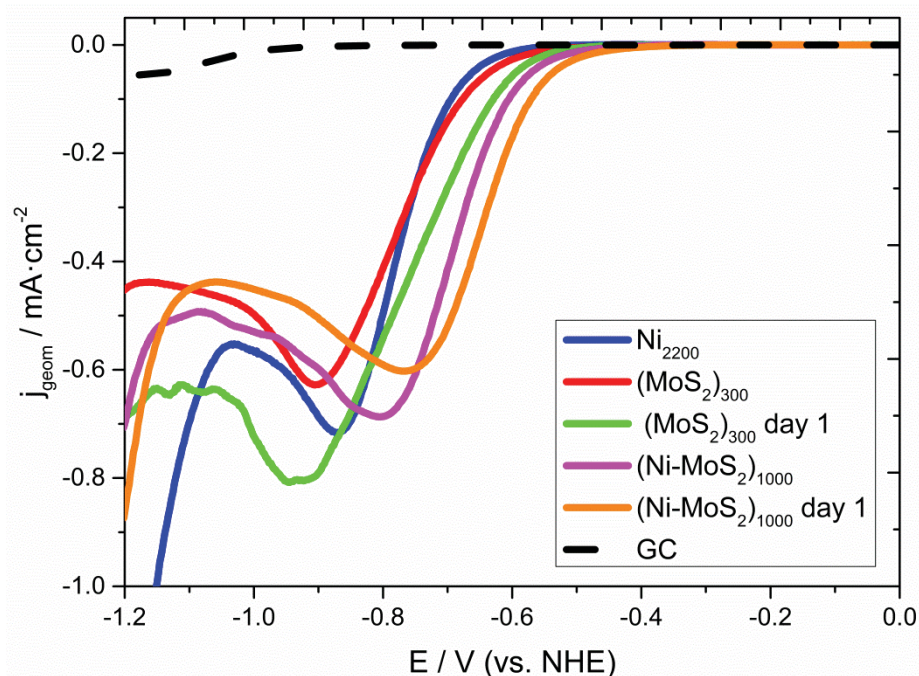


Figure 3.10 Linear sweep voltammograms recorded at 5 mm diameter glassy carbon (dashed black) samples modified with (a) fresh (MoS₂)₃₀₀ (solid red), (b) fresh (Ni-MoS₂)₁₀₀₀ (solid magenta), (c) Ni₂₂₀₀ (solid blue), (d) 14-h air exposed (MoS₂)₃₀₀ (solid green), and (e) 14-h air exposed (Ni-MoS₂)₁₀₀₀ (solid orange) clusters in the 0 to -1.2 V range vs. NHE. Scan rate: 25 mV s⁻¹.

Freshly prepared (MoS₂)₃₀₀ clusters (Figure 3.10a) exhibit an onset potential of ca. 650 mV, reaching a peak half maximum current density ($j_{half\ max}$) of 0.31 mA cm⁻² at an overpotential (η) of ca. 770 mV. The experimental onset potential is approx. 400 mV higher than that of 2H-MoS₂ nanosheets reported in the literature (ca. 200 mV vs NHE): this originates from the MoS₂ preparation methodology and hence the degree of sulphur enrichment.

The main factors that hinder HER activity in MoS₂ materials are their intrinsic conductivity, metal-to-chalcogen ratio, edge site abundance and catalyst loading. Previous investigations from our research group demonstrated that magnetron-sputtered MoS₂ size-selected clusters presented a 2-layer thickness in the 150-500 unit range [5]. In this investigation, it was observed again that (MoS₂)₃₀₀ clusters exhibit an incomplete multilayered structure ranging from 1 to 4 layers. As through-plane electron mobility in MoS₂ is 2200 times slower than in-plane, the absence of single-layered clusters hampers the electrocatalytic activity. XPS analysis performed in this study have revealed that both (MoS₂)₃₀₀ and (Ni-MoS₂)₁₀₀₀ clusters are S-deficient. A high correlation between metal-to-chalcogen ratio and HER activity has been extensively reported. Eng et al. observed a substantial increase in both HER overpotential and Tafel slope in chalcogen deficient TMDs [35], that can be ascribed in the case of MoS₂ to a deficiency of active sites and the formation of oxide species MoO₂/MoO₃ at the S-deficient sites, experimentally confirmed by XPS measurements reported here. The intrinsic MoO₃ material has not been regarded as a catalyst in HER due to the lack of active edges [36].

Sulphur-rich MoS₂ nanostructures with enhanced HER activities and stability in an acidic environment have been prepared by use of gas phase or liquid phase methods. However, evidence has shown that the morphology of MoS₂ is modified by the exposure to the sulphur gas phase or liquid phase [37, 38]. Thus, ex-situ sulfidation treatments were not performed to guarantee that the HER enhancement in the samples is unambiguously due to the Ni-doping of the edge sites. In addition to this, reports by Vruble et al. and Rowley-Neil et al. revealed that

the HER activity of the molybdenum sulfide catalysts is correlated with the catalyst loading: higher molybdenum sulfide catalyst loading lead to enhanced HER performance [39, 40]. Thus, the HER performance of our clusters cannot be unambiguously judged by the current density values obtained at the same overpotentials as those reported by the literature. Assuming a cluster interspacing of 2.5 nm, the mass loadings for Ni₂₂₀₀, (MoS₂)₃₀₀ and (Ni-MoS₂)₁₀₀₀ are 1.28 μg cm⁻², 3.45 μg cm⁻² and 4.25 μg cm⁻², respectively. These values are at least one order of magnitude smaller than those reported in more competitive MoS₂ materials, supporting our claims that the low catalyst loadings lead to overpotentials higher than those reported in the literature.

Electrochemical testing of the (MoS₂)₃₀₀ clusters after the aforementioned testing and exposure to air for 14 hours indicates an enhancement in their electrocatalytic performance to the HER, with a $j_{half\ max}$ of ca. 0.40 mA cm⁻² at $\eta \approx 749$ mV. This is due to the dissolution of the (MoS₂)₃₀₀ clusters outermost layers due to the conversion of MoS₂ to MoO₃, compound soluble in acidic conditions. Yu et al. observed that electrochemical cycling of bilayered MoS₂ nanoflakes assisted in the oxidation of Mo⁴⁺ to Mo⁶⁺ ascribed to air exposure, leading to the complete loss of the MoS₂ outermost layer after re-immersion in the acidic electrolyte used. The loss of such layer resulted in enhanced HER performance and Tafel slope, concluding that the loss of a full MoS₂ monolayer increases the HER activity by a factor of ~4.47 [41]. As the (MoS₂)₃₀₀ clusters have been shown to consist of an incomplete multilayered structure (1 to 4 MoS₂ layers thick,), any loss of the outermost layers will consequently enhance the HER activity.

Similar voltammograms were recorded for (Ni-MoS₂)₁₀₀₀ hybrid clusters (Figure 3.10b). It can be seen that (Ni-MoS₂)₁₀₀₀ hybrid clusters exhibit a significant improvement in the electrocatalytic activity with respect to the undoped counterparts: the onset potential is reduced by ca. 100 mV and the $j_{half\ max}$ (0.35 mA cm⁻²) is reached at $\eta \approx 680$ mV (100 mV less than

(MoS₂)₃₀₀ clusters). To confirm that the HER enhancement is due to the effective Ni-doping of the S-edge sites and not to the presence of HER-active Ni clusters in the sample, the response of a GC sample modified with Ni clusters (average atomic mass units= 2200, Figure 3.10c) was evaluated. Ni₂₂₀₀ clusters exhibited an onset potential and $j_{half\ max}$ similar to (MoS₂)₃₀₀ clusters (0.36 mA cm⁻², $\eta \approx 770$ mV) but with faster HER kinetics (as per Tafel analysis, vide infra). This is evidenced by the fact that Ni₂₂₀₀ clusters achieve a peak current density (j_p) of 0.72 mA cm⁻² at $\eta \approx 870$ mV whereas (MoS₂)₃₀₀ clusters only a $j_p = 0.63$ mA cm⁻² at $\eta \approx 905$ mV. Thus, we can satisfactorily conclude that the HER enhancement observed in (Ni-MoS₂)₁₀₀₀ clusters is due to the increase in active edge sites density upon Ni-doping of the initially inactive S-edge sites.

Exchange current density (j_0) can provide insight on the predicted HER enhancement by Ni-doping as well as an indication of the intrinsic activity per-site. Freshly-prepared (MoS₂)₃₀₀ and (Ni-MoS₂)₁₀₀₀ clusters presented similar j_0 values ($\approx 8 \times 10^{-10}$ A cm⁻²), but after the above electrochemical experiments and 14-h air exposure (Ni-MoS₂)₁₀₀₀ hybrid clusters (Figure 3.10e) showed an almost 3-fold increase with respect to their initial j_0 value (2.1×10^{-9} vs. 7.6×10^{-10}). This significant HER enhancement is in good agreement with previous reports that indicated a 3-fold increase in active sites but a worse per-site activity due to the overall less thermo-neutral ΔG_H values.

Tafel slope analysis was then carried out to provide insight into the HER efficiency of the catalysts and the HER reaction mechanism. Noble metals such as Pt follow the Volmer-Tafel mechanism, in which the rate determining step is the chemical hydrogen desorption from the catalyst surface, with Tafel slopes $b \approx 30$ mV dec⁻¹ [30]. Tafel slope analysis of the 25mV s⁻¹ cathodic scans (Figure 3.11) revealed that all the MoS₂ samples are in the 95-130 mV dec⁻¹ range, (MoS₂)₃₀₀ exhibiting the lowest Tafel slope (94 mV dec⁻¹) after exposure to air for 14

hours. This compares to exfoliated MoS₂ layers reported to display Tafel slopes, $b \approx 120 \text{ mV dec}^{-1}$, in agreement with the Volmer mechanism which dictates the monoatomic hydrogen adsorption to be the limiting step [42]. Edge-rich nanosheets and pure 1T-phase MoS₂ samples exhibited, respectively, $b \approx 55\text{-}60 \text{ mV dec}^{-1}$ and $b \approx 40 \text{ mV dec}^{-1}$ [15, 31].

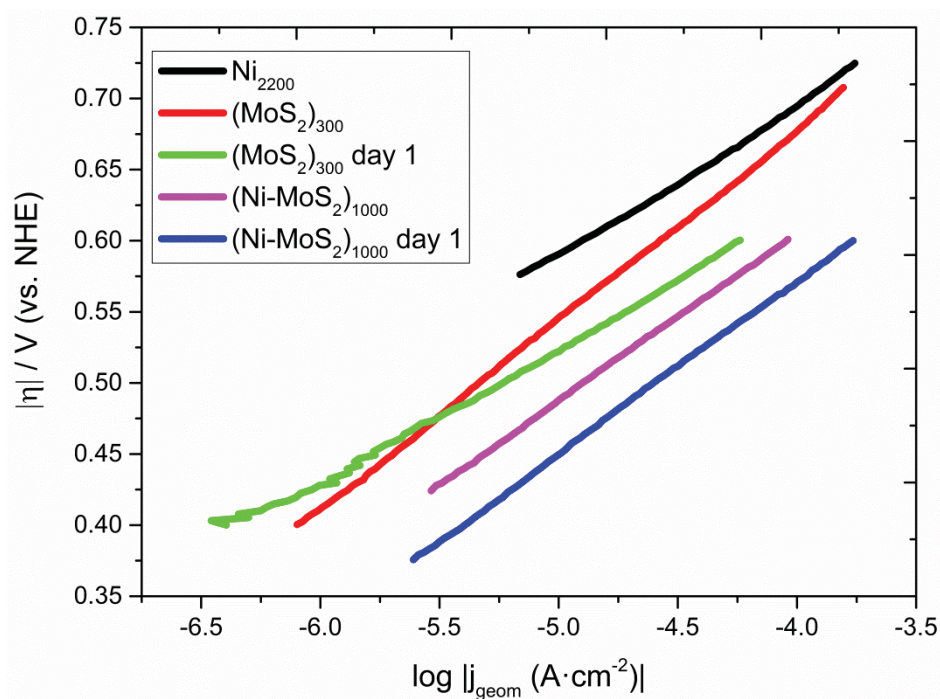


Figure 3.11 Tafel plots (η vs. $\log |j_{geom}|$) of the Ni-doped/undoped MoS₂ clusters with scan rate: 25 mV s^{-1} .

Electrodissolution of oxygen-rich HER inactive regions or electrochemical exfoliation of MoS₂ outermost layers, previously reported in the literature, might expose edge-abundant cluster regions with a higher through-plane conductivity that could explain (MoS₂)₃₀₀ lower Tafel slope after air exposure. Ni₂₂₀₀ samples present a Tafel slope of 106 mV dec^{-1} , similar to the $b \approx 120 \text{ mV dec}^{-1}$ reported in the literature for electrodeposited Ni thin films. When as-prepared Ni-doped/undoped MoS₂ clusters are compared, Ni-doping does not decrease the Tafel slope value significantly, leaving the HER mechanism unchanged as reported previously [23].

The HER enhancement of (Ni-MoS₂)₁₀₀₀ hybrid clusters after 14 h air exposure is probably related to the Ni surface: reports suggest this could comprise a spontaneously formed NiO+Ni(OH)₂ shell several atomic layers thick [43]. Oxygen present in the NiO+Ni(OH)₂ shell acts a proton-acceptor site, reported both theoretically and experimentally to catalyse HER [44, 45]. The presence of NiO after 14 h air exposure of (Ni-MoS₂)₁₀₀₀ hybrid clusters has been confirmed by XPS measurements (see previous analysis), which is also expected to be found in the samples tested electrochemically. This effect would synergistically contribute to the HER enhancement already observed for 14 h air exposed (MoS₂)₃₀₀ related to the dissolution of the MoS₂ outermost layers.

3.5 Conclusions

Size-controlled (MoS₂)₃₀₀ and Ni₂₂₀₀ clusters have been produced by cluster beam deposition with magnetron sputtering and gas condensation techniques. Ni-MoS₂ hybrid clusters have also been successfully fabricated by dual target magnetron sputtering, obtaining a unimodal size distribution with an average cluster size of 1000 equivalent MoS₂ sub-units. The MoS₂ clusters present an incomplete multi-layer structure, which can also be found in Ni-MoS₂ hybrid clusters. EDX mapping on the aberration-corrected HAADF-STEM images confirms that the resulting clusters are a hybrid of Ni and MoS₂ rather than their segregated components. The composition analysis shows that there is no fixed ratio of Ni atoms to MoS₂ units in the hybrid clusters, but in general, the proportion of Ni increases with cluster size, which agrees with the EDX results. Sulphur-deficient nature in both MoS₂ clusters (Mo:S = 1:0.9) and Ni-MoS₂ hybrid clusters (Mo:S = 1:1.8) was revealed by XPS measurements.

The activity of Ni-MoS₂ hybrid clusters is on par with previous reports of electrocatalytic enhancement to HER: an almost 3-fold increase in exchange current densities along with a

significant shift in the onset potential (approx. 100 mV), as well as an almost unaffected Tafel slope ($\approx 120 \text{ mVdec}^{-1}$). This activity is only achieved when clusters are exposed to the atmospheric environment, suggesting that the Ni-doped edge sites become fully HER active only when Ni dopant atoms are oxidised.

References

- [1] Escalera-López D, Niu Y, Yin J, Cooke K, Rees NV, Palmer RE. Enhancement of the hydrogen evolution reaction from Ni-MoS₂ hybrid nanoclusters. *ACS Catalysis* **2016**, 6(9): 6008-6017.
- [2] Novoselov KS, Jiang D, Schedin F, Booth TJ, Khotkevich VV, Morozov SV, *et al.* Two-dimensional atomic crystals. *Proc. Natl. Acad. Sci. U. S. A.* **2005**, 102(30): 10451-10453.
- [3] Akinwande D, Petrone N, Hone J. Two-dimensional flexible nanoelectronics. *Nat. Commun.* **2014**, 5: 5678.
- [4] Chhowalla M, Shin HS, Eda G, Li LJ, Loh KP, Zhang H. The chemistry of two-dimensional layered transition metal dichalcogenide nanosheets. *Nat. Chem.* **2013**, 5(4): 263-275.
- [5] Cuddy MJ, Arkill KP, Wang ZW, Komsa HP, Krasheninnikov AV, Palmer RE. Fabrication and atomic structure of size-selected, layered MoS₂ clusters for catalysis. *Nanoscale* **2014**.
- [6] Gemming S, Seifert G. Nanocrystals: catalysts on the edge. *Nat Nanotechnol* **2007**, 2(1): 21-22.
- [7] Wu W, Wang L, Li Y, Zhang F, Lin L, Niu S, *et al.* Piezoelectricity of single-atomic-layer MoS₂ for energy conversion and piezotronics. *Nature* **2014**, 514(7523): 470-474.
- [8] Ganatra R, Zhang Q. Few-layer MoS₂: A promising layered semiconductor. *ACS Nano* **2014**, 8(5): 4074-4099.
- [9] Laursen AB, Kegnæs S, Dahl S, Chorkendorff I. Molybdenum sulfides: efficient and viable materials for electro- and photoelectrocatalytic hydrogen evolution. *Energy & Environmental Science* **2012**, 5(2): 5577.

- [10] Wang QH, Kalantar-Zadeh K, Kis A, Coleman JN, Strano MS. Electronics and optoelectronics of two-dimensional transition metal dichalcogenides. *Nature Nanotechnology* **2012**, 7(11): 699-712.
- [11] Chen Z, Liu X, Liu Y, Günsel S, Luo J. Ultrathin MoS₂ nanosheets with superior extreme pressure property as boundary lubricants. *Sci. Rep.* **2015**, 5: 12869.
- [12] Yang D, Sandoval S, Divigalpitiya W, Irwin J, Frindt R. Structure of single-molecular-layer MoS₂. *Physical Review B* **1991**, 43(14): 12053-12056.
- [13] Joswig JO, Lorenz T, Wendumu TB, Gemming S, Seifert G. Optics, mechanics, and energetics of two-dimensional MoS₂ nanostructures from a theoretical perspective. *Acc. Chem. Res.* **2015**, 48(1): 48-55.
- [14] Jaramillo TF, Jorgensen KP, Bonde J, Nielsen JH, Horch S, Chorkendorff I. Identification of active edge sites for electrochemical H₂ evolution from MoS₂ nanocatalysts. *Science* **2007**, 317(5834): 100-102.
- [15] Voiry D, Salehi M, Silva R, Fujita T, Chen MW, Asefa T, *et al.* Conducting MoS₂ nanosheets as catalysts for hydrogen evolution reaction. *Nano Lett.* **2013**, 13(12): 6222-6227.
- [16] Chen ZB, Cummins D, Reinecke BN, Clark E, Sunkara MK, Jaramillo TF. Core-shell MoO₃- MoS₂ nanowires for hydrogen evolution: a functional design for electrocatalytic materials. *Nano Lett.* **2011**, 11(10): 4168-4175.
- [17] Kibsgaard J, Chen ZB, Reinecke BN, Jaramillo TF. Engineering the surface structure of MoS₂ to preferentially expose active edge sites for electrocatalysis. *Nature Materials* **2012**, 11(11): 963-969.
- [18] Li YG, Wang HL, Xie LM, Liang YY, Hong GS, Dai HJ. MoS₂ nanoparticles grown on graphene: an advanced catalyst for the hydrogen evolution reaction. *J. Am. Chem. Soc.* **2011**, 133(19): 7296-7299.

- [19] Hinnemann B, Moses PG, Bonde J, Jorgensen KP, Nielsen JH, Horch S, *et al.* Biomimetic hydrogen evolution: MoS₂ nanoparticles as catalyst for hydrogen evolution. *J. Am. Chem. Soc.* **2005**, 127(15): 5308-5309.
- [20] Benck JD, Hellstern TR, Kibsgaard J, Chakthranont P, Jaramillo TF. Catalyzing the hydrogen evolution reaction (HER) with molybdenum sulfide nanomaterials. *ACS Catalysis* **2014**, 4(11): 3957-3971.
- [21] Bonde J, Moses PG, Jaramillo TF, Norskov JK, Chorkendorff I. Hydrogen evolution on nano-particulate transition metal sulfides. *Faraday Discuss.* **2008**, 140: 219-231.
- [22] Vrubel H, Merki D, Hu X. Hydrogen evolution catalyzed by MoS₃ and MoS₂ particles. *Energy & Environmental Science* **2012**, 5(3): 6136.
- [23] Wang H, Tsai C, Kong D, Chan K, Abild-Pedersen F, Nørskov JK, *et al.* Transition-metal doped edge sites in vertically aligned MoS₂ catalysts for enhanced hydrogen evolution. *Nano Research* **2015**, 8(2): 566-575.
- [24] Kibsgaard J, Tuxen A, Knudsen KG, Brorson M, Topsoe H, Laegsgaard E, *et al.* Comparative atomic-scale analysis of promotional effects by late 3d-transition metals in MoS₂ hydrotreating catalysts. *J. Catal.* **2010**, 272(2): 195-203.
- [25] Lauritsen JV, Kibsgaard J, Helveg S, Topsoe H, Clausen BS, Laegsgaard E, *et al.* Size-dependent structure of MoS₂ nanocrystals. *Nat Nanotechnol* **2007**, 2(1): 53-58.
- [26] Wang ZW, Palmer RE. Intensity calibration and atomic imaging of size-selected Au and Pd clusters in aberration-corrected HAADF-STEM. *Journal of Physics: Conference Series* **2012**, 371: 012010.
- [27] Brown NMD, Cui NY, McKinley A. An xps study of the surface modification of natural MoS₂ following treatment in an RF-oxygen plasma. *Appl. Surf. Sci.* **1998**, 134(1-4): 11-21.

- [28] Gruenert W, Stakheev AY, Feldhaus R, Anders K, Shpiro ES, Minachev KM. Analysis of molybdenum(3d) XPS spectra of supported molybdenum catalysts: an alternative approach. *The Journal of Physical Chemistry* **1991**, 95(3): 1323-1328.
- [29] Baker MA, Gilmore R, Lenardi C, Gissler W. XPS investigation of preferential sputtering of S from MoS₂ and determination of MoS_x stoichiometry from Mo and S peak positions. *Appl. Surf. Sci.* **1999**, 150(1-4): 255-262.
- [30] Escalera-Lopez D, Gomez E, Valles E. Electrochemical growth of CoNi and Pt-CoNi soft magnetic composites on an alkanethiol monolayer-modified ito substrate. *Phys. Chem. Chem. Phys.* **2015**, 17(25): 16575-16586.
- [31] Biesinger MC, Payne BP, Lau LWM, Gerson A, Smart RSC. X-ray photoelectron spectroscopic chemical state quantification of mixed nickel metal, oxide and hydroxide systems. *Surf. Interface Anal.* **2009**, 41(4): 324-332.
- [32] Grosvenor AP, Biesinger MC, Smart RS, McIntyre NS. New interpretations of XPS spectra of nickel metal and oxides. *Surf. Sci.* **2006**, 600(9): 1771-1779.
- [33] Jiang N, Tang Q, Sheng ML, You B, Jiang DE, Sun YJ. Nickel sulfides for electrocatalytic hydrogen evolution under alkaline conditions: a case study of crystalline NiS, NiS₂, and Ni₃S₂ nanoparticles. *Catalysis Science & Technology* **2016**, 6(4): 1077-1084.
- [34] Jiang N, Bogoev L, Popova M, Gul S, Yano J, Sun YJ. Electrodeposited nickel-sulfide films as competent hydrogen evolution catalysts in neutral water. *Journal of Materials Chemistry A* **2014**, 2(45): 19407-19414.
- [35] Eng AYS, Ambrosi A, Sofer Z, Simek P, Pumera M. Electrochemistry of transition metal dichalcogenides: strong dependence on the metal-to-chalcogen composition and exfoliation method. *Acs Nano* **2014**, 8(12): 12185-12198.

- [36] Luo Z, Miao R, Huan TD, Mosa IM, Poyraz AS, Zhong W, *et al.* Mesoporous MoO_{3-x} material as an efficient electrocatalyst for hydrogen evolution reactions. *Advanced Energy Materials* **2016**, 6(16).
- [37] Xie S, Xu MS, Liang T, Huang GW, Wang SP, Xue GB, *et al.* A high-quality round-shaped monolayer MoS₂ domain and its transformation. *Nanoscale* **2016**, 8(1): 219-225.
- [38] Burch HA, Isaacs M, Wilson K, Palmer RE, Rees NV. Electrocatalytic regeneration of atmospherically aged MoS₂ nanostructures via solution-phase sulfidation. *Rsc Advances* **2016**, 6(32): 26689-26695.
- [39] Rowley-Neale SJ, Brownson DAC, Smith GC, Sawtell DAG, Kelly PJ, Banks CE. 2d nanosheet molybdenum disulphide (MoS₂) modified electrodes explored towards the hydrogen evolution reaction. *Nanoscale* **2015**, 7(43): 18152-18168.
- [40] Vrabel H, Hu XL. Growth and activation of an amorphous molybdenum sulfide hydrogen evolving catalyst. *Acs Catalysis* **2013**, 3(9): 2002-2011.
- [41] Yu Y, Huang SY, Li Y, Steinmann SN, Yang W, Cao L. Layer-dependent electrocatalysis of MoS₂ for hydrogen evolution. *Nano Lett.* **2014**, 14(2): 553-558.
- [42] Benck JD, Chen ZB, Kuritzky LY, Forman AJ, Jaramillo TF. Amorphous molybdenum sulfide catalysts for electrochemical hydrogen production: insights into the origin of their catalytic activity. *Acs Catalysis* **2012**, 2(9): 1916-1923.
- [43] Medway SL, Lucas CA, Kowal A, Nichols RJ, Johnson D. In situ studies of the oxidation of nickel electrodes in alkaline solution. *J. Electroanal. Chem.* **2006**, 587(1): 172-181.
- [44] Subbaraman R, Tripkovic D, Strmcnik D, Chang KC, Uchimura M, Paulikas AP, *et al.* Enhancing hydrogen evolution activity in water splitting by tailoring Li⁺-Ni(OH)₂-Pt interfaces. *Science* **2011**, 334(6060): 1256-1260.

- [45] Thiel PA, Madey TE. The interaction of water with solid surfaces: fundamental aspects. *Surf. Sci. Rep.* **1987**, 7(6-8): 211-385.

Chapter 4

Modification of Deposited, Size-Selected MoS₂ Clusters by Sulphur-Enrichment and Their HER Activities

Most of the work in this chapter has been represented in my publications of “**Niu Y**, Park S, Palmer R. Modification of deposited, size-selected MoS₂ nanoclusters by sulphur addition: An aberration-corrected stem study. *Inorganics* 2016, 5(4): 1” [1] (the draft of this paper was written by me) and “Escalera-López D, **Niu Y**, Park S, Isaacs M, Wilson K, Palmer RE, Rees NV. Hydrogen evolution enhancement of ultra-low loading, size-selected molybdenum sulfide nanoclusters by sulfur enrichment. *Applied Catalysis B: Environmental* 2018, 235: 84-91” [2] (I was in charge of the cluster fabrication and STEM analysis, and Daniel Escalera Lopez was in charge of the XPS analysis HER analysis). Most of the text and figures have also been used in the publications.

4.1 Introduction

In the MoS₂ nanomaterials, the low coordinated, additional sulphur atoms at Mo-edge sites are notably active in HER [3-6], and these materials are sulphur rich, with stoichiometry MoS_{2+x}, rather than MoS₂. The electrocatalytic activity tends to decrease with an increase in the number of MoS₂ layers, due to poor electron hopping efficiency between the stacked layers [7]. In

general, edge-abundant MoS₂ nanomaterials remain a potential substitute for scarce and costly platinum-based catalysts [4, 8]. Good control over the atomic structure of MoS₂ nanostructures should contribute to the enhancement of the catalytic performance.

Several methods have been developed to fabricate nanostructured MoS₂ with one or several layers, such as chemical exfoliation of bulk MoS₂ [9], chemical vapour deposition (CVD) [7, 10] and solvothermal synthesis [11]. However, the chemical preparation of MoS₂ nanomaterials with well-defined size is still a formidable challenge. The preparation of size-selected MoS₂ clusters by the cluster beam deposition technique was reported by Cuddy et al [12]. The clusters were reported to be somewhat sulphur poor. The sulphur-deficient nature of MoS₂ clusters produced with cluster beam deposition was also discussed in Chapter 3. Here we studied an in vacuum processing approach, based on a combination of sulphur addition (by sublimation) and annealing inside the cluster beam source, to increase the sulphur content of the clusters and to explore structural modifications. The atomic structures of these MoS₂ clusters were characterised with an aberration-corrected STEM in HAADF mode [13-16]. Their catalytic activities to HER were also explored.

4.2 Materials and Methods

Size-selected MoS₂ clusters were produced using a magnetron sputtering (DC, 45 W) and gas condensation cluster beam source (Figure 2.1, Chapter 2) [17]. A 2-inch sputtering MoS₂ target (PI-KEM, 99.9% purity) was used and Ar (180 sccm) and He (160 sccm) gases were introduced to enable sputtering and cluster condensation, respectively. The positively charged clusters were accelerated with ion optical electrostatic lenses and then size-selected with a lateral time-of-flight mass filter [18]. The size-selected MoS₂ clusters were deposited onto amorphous carbon-coated TEM grids (Agar Scientific, 200 Mesh Cu) and thin silica films coated TEM

grids (EMS, 200 Mesh Cu). The mass resolution of the time-of-flight mass filter used in the experiment is ~ 20 (e.g. the error in the deposition of a cluster containing 40 atoms is ± 1.0 atoms). Sulphur addition was conducted in a sulphur atmosphere created by evaporating sulphur using a home-built in-situ thermal evaporator (5 min) shown in Figure 4.1. Annealing (7 min, 215 ± 5 °C) was performed with an electron beam bombardment heating stage. The temperature was monitored using a pyrometer (IMPAC Pyrometer, IPE 140). All the STEM images were taken with a 200 kV spherical aberration-corrected STEM in the HAADF mode. All electrochemical measurements were performed in a conventional 3-electrode electrochemical set-up. The solution and method used in the electrochemical measurements were described in Chapter 3.

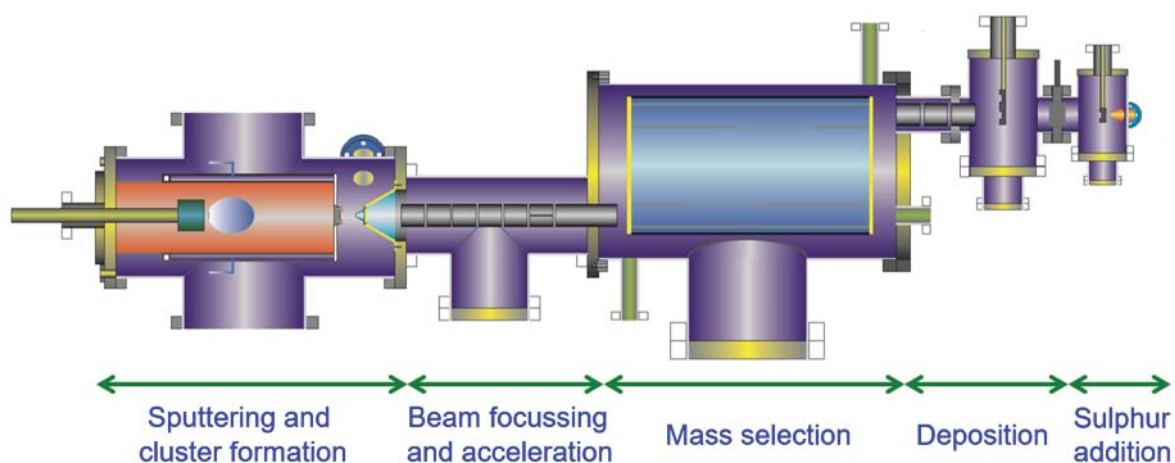


Figure 4.1 Schematic illustration of the size selected cluster beam source together with sulphur addition chamber. The cluster beam source was described in Chapter 2. An additional chamber is attached to the deposition chamber with a thermal evaporator and heating stage in it.

4.3 Atomic Structure of As-Deposited MoS₂ Clusters

Size-selected MoS₂ clusters were produced using a gas condensation, magnetron sputtering cluster source in conjunction with a lateral time-of-flight mass filter [17, 18]. The clusters were deposited onto amorphous carbon covered TEM grids with an impact energy of 1.5 eV per MoS₂ unit [e.g. a 1500 V bias is applied to the substrate in the deposition of (MoS₂)₁₀₀₀]. Figure 4.2a shows an aberration-corrected HAADF-STEM image of (MoS₂)₁₀₀₀ clusters at low magnification with a peak diameter of 5.5 nm (Figure 4.2b). The clusters were deposited with a surface coverage of ~5 % (approx. 5% of the surface area is covered by the clusters) to keep them separate. However, the image shows that some clusters diffused and aggregated after deposition. The HAADF intensity distribution (Figure 4.2c) measured from 155 independent clusters indicates several peaks in the size spectrum. In order to confirm which peak corresponds to the original (MoS₂)₁₀₀₀ clusters, the size of the cluster shown in Figure 4.2d was derived from Mo atom counting used in Chapter 3 [13, 19]. This cluster was found to contain approximately 1100 Mo atoms and is located in peak 3. This indicates peak 3 is the peak corresponding to the original (MoS₂)₁₀₀₀ clusters, while peak 4 corresponds to clusters with double mass. We note there are some clusters located in the lower intensity region (peaks 1 and 2, Figure 4.2c) and, correspondingly, in the smaller diameter region (3.8 ± 1.8 nm, Figure 4.2b). We believe that these smaller clusters may come from the fragmentation of the original clusters during the impact on the substrate surface. It is notable that the sum of the peak intensities of peak 1 and peak 2 in Figure 4.2c is located in the region of peak 3. An interpretation is that, during the formation process in the cluster source, small clusters may sometimes aggregate, being bonded to each other with a rather weak interaction in the gas condensation process. We envisage that such “composite clusters” may break up into two or more smaller clusters when they land on the support.

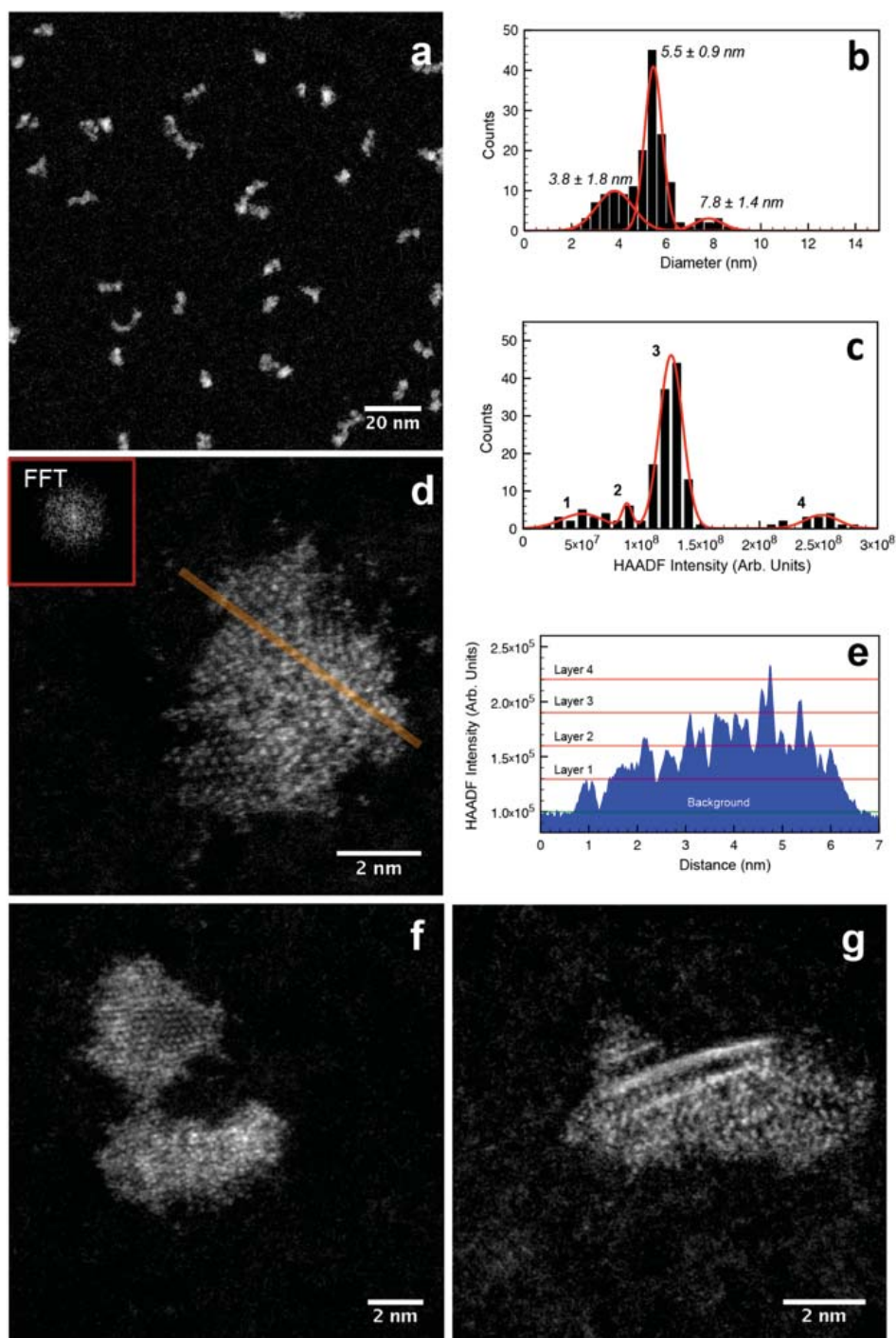


Figure 4.2 STEM images of as-deposited size-selected (MoS₂)₁₀₀₀ clusters shown at (a) low and (d) high magnification with FFT pattern inset. (b) Size distribution and (c) integrated HAADF intensity distribution of independent clusters. (e) HAADF intensity line profile corresponding to the orange line in (d). (f) (MoS₂)₁₀₀₀ cluster with partially crystalline structure.

(g) A side-on (oriented perpendicular to the substrate) MoS₂ cluster displays its layered structure.

Figure 4.2d highlights the atomic structure of one MoS₂ cluster at higher magnification and includes a FFT pattern, inset. The shape of the cluster is rather irregular and the absence of extended crystalline order is confirmed by the diffuse ring in the FFT pattern. While most clusters present such poorly ordered structures, a few clusters are observed with more developed crystalline structure, as shown in Figure 4.2f. The uneven layered structure of cluster is evident in the steps in the HAADF intensity line profile (Figure 4.2e). The STEM image intensity is proportional to the number of MoS₂ layers. The HAADF intensity line profile indicates the cluster has an approximate pyramid shape with four layers in the central part. The layered structure of the MoS₂ clusters is also confirmed by the side-on cluster shown in Figure 4.2g. This side-on structure displays the (002) edge sites with a 0.67 nm interlayer spacing comparable with that of bulk MoS₂ (0.65 nm) [20]. Similar TEM images on particular side-on MoS₂ nanoparticles were reported recently by Fei et al. [21] Such side-on clusters were captured in only a few cases, which might depend on favourable bonding to particular defects on the support.

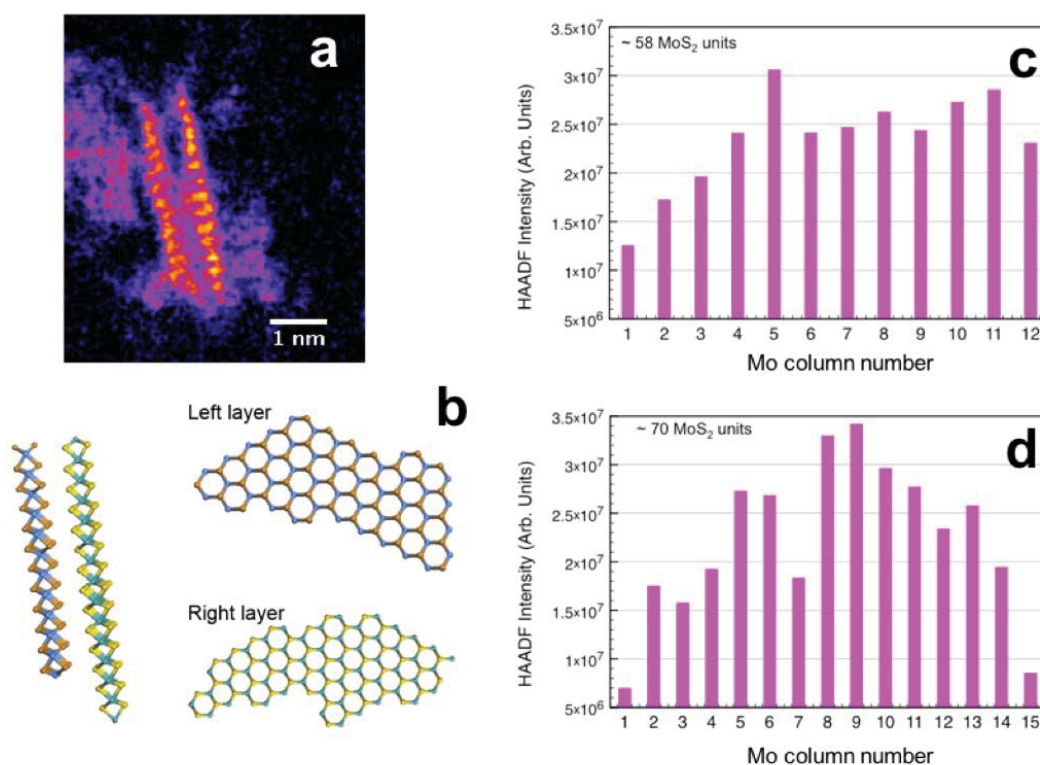


Figure 4.3 HAADF-STEM image (a) and simulated structure (b) of side-on (MoS₂)₆₅₀ cluster (bilayer), and the atomically resolved HAADF-STEM intensity maps of the left (c) and right (d) single layer. The Mo column number in c and d means the counting number of the Mo dot from up to down.

Figure 4.3a illustrates a side-on MoS₂ cluster which was found among (MoS₂)₆₅₀ clusters with an observed interlayer spacing of 0.69 ± 0.07 nm in accordance with that of bulk MoS₂ (0.615 nm), and Figure 4.3b presents a model of this side-on cluster. By comparing its HAADF intensity with the (MoS₂)₆₅₀ cluster, we can determine that this bilayer cluster is a fragment originating from a (MoS₂)₆₅₀ cluster. This implies MoS₂ clusters can realise a given mass by combining two or more small clusters besides increasing single layer area and stack layers, which can also be found in size-selected (MoS₂)₁₀₀₀ clusters.

The HAADF intensity of each Mo column in this bilayer was measured, and the number of MoS₂ units was calculated by comparing with the intensity of (MoS₂)₆₅₀. The atomically

resolved intensity maps (Figure 4.3c, d) show that this bilayer contains ~128 MoS₂ units with 58 units in the left layer and 70 units in the right layer. The changing trends of intensity from column to column indicate that both these two layers have no regular shapes (polygon), and that the left layer has a different shape than the right layer, this can be seen in the structural model of this bilayer based on HAADF intensity (Figure 4.3d). Unlike the trigon or truncated trigon morphologies made by chemical synthesis such as sulphurising Mo islands on Au(111), the irregular shapes of the single MoS₂ layer provide firm evidence showing the quasi-stable growth process of the MoS₂ cluster in the condensation chamber due to short residence time in this chamber and rapid quenching of growth after the supersonic expansion.

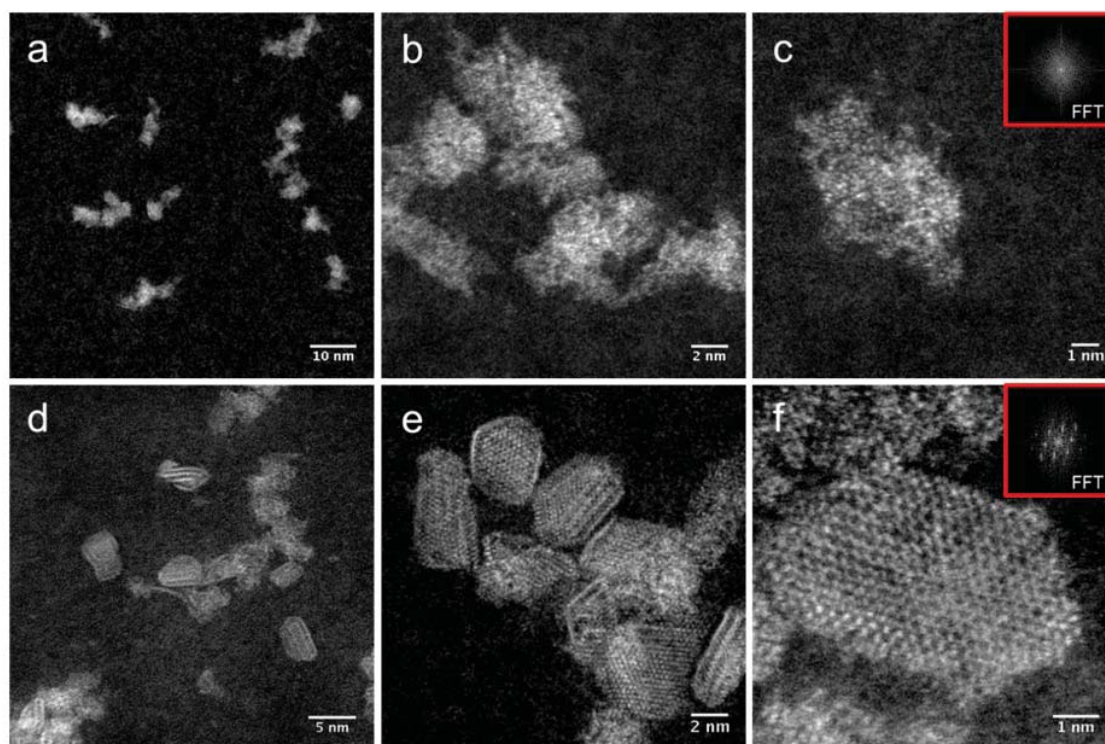


Figure 4.4 (a, b, c) STEM images of (MoS₂)₁₀₀₀ clusters deposited on amorphous carbon at low and high magnifications, and the FFT pattern indicates the amorphous feature of the cluster. (d, e, f) STEM images of (MoS₂)₁₀₀₀ clusters deposited on silica at low and high magnifications, and the FFT pattern indicates the crystalline feature of the cluster.

During the deposition of size-selected MoS₂ clusters, a support-effect was found when (MoS₂)₁₀₀₀ clusters were deposited onto amorphous carbon film and silica film. Figure 4.4 shows the STEM images of the (MoS₂)₁₀₀₀ clusters deposited on those two kinds of supports, and a much different structural feature can be found. The clusters on amorphous carbon display amorphous feature confirmed by FFT (Figure 4.4c) and partial crystalline feature. In contrast, quite a number of the clusters on the silica present clearly crystalline structure. This crystalline structure might come from single- or multi-wall Fullerene-like cage, which is highly stable even after annealing under 215 ± 5 °C (Figure 4.5a). Besides annealing, the crystalline structure also underwent electron beam irradiation, and the related STEM images are shown in Figure 4.5b and 4.5c. After about 20 min electron beam irradiation, a hole was drilled in the middle of the cluster. This might be because the cage structure was destroyed from the weak point (the middle in this case) by the electron beam, the atoms in the middle were pulled away by the adjacent surfaces, and then formed a hole in the middle. However, it can be seen that the cage construction was retained, which implies this is a rather stable structure.

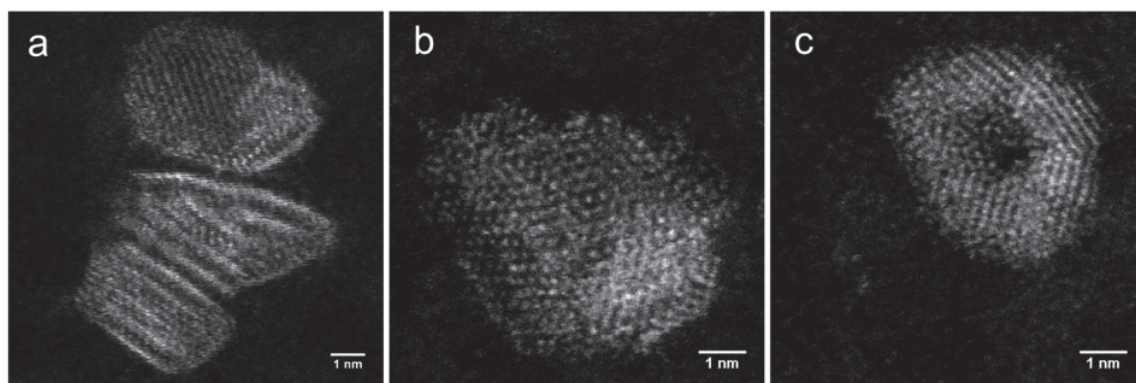


Figure 4.5 STEM image of annealed (7 min, 215 ± 5 °C) (MoS₂)₁₀₀₀ clusters deposited on silica, and STEM images of (MoS₂)₁₀₀₀ clusters deposited on silica (b) before and (c) after electron beam irradiation for ~20 min.

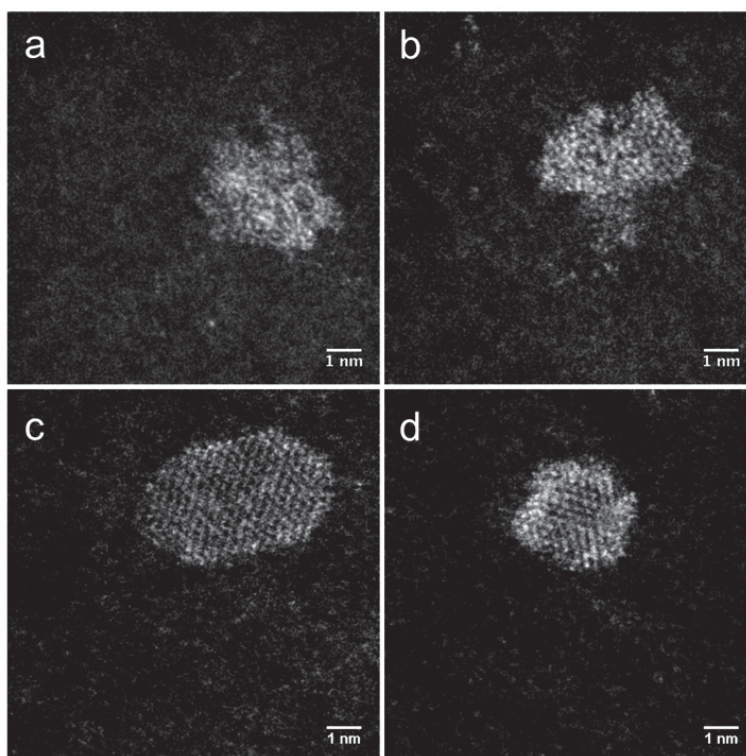


Figure 4.6 STEM images of (MoS₂)₅₀₀ clusters deposited on (a, b) amorphous carbon and (c, d) silica.

The support-effect was also found among (MoS₂)₅₀₀ clusters shown in Figure 4.6. The (MoS₂)₅₀₀ clusters on amorphous carbon (Figure 4.6a and 4.6b) show amorphous feature, while the clusters on silica (Figure 4.6c and 4.6d) present crystalline structures. The cluster shown in Figure 4.6c displays a hexagonal shape with a projected area of 16.71 nm². Given that there are 500 MoS₂ units in the cluster, the calculation indicates the cluster has 2.6 layers rather than a monolayer. It can be seen that four of the six edges of the cluster are brighter than the middle part, which implies there are might be several vertical layers on edge sites in between the bottom layer and up layer. This indicates this cluster might be a Fullerene-like cage, which also happens in the cluster shown in Figure 4.6d.

4.4 Atomic Structure of Sulphur-Added MoS₂ Clusters

One possible cause of the limited crystallinity of the as-deposited MoS₂ clusters observed here is the sulphur deficiency discussed in Chapter 3 and our previous study [12]. Thus, we have explored sulphur addition (by thermal sublimation of solid sulphur for 5 minutes) to the deposited clusters, in vacuum (in the cluster source), accompanied by thermal annealing (7 min, 215 ± 5 °C). The nominal amount of sulphur deposited was equivalent to a thick film (10,000 layers), but the excess sulphur (i.e. beyond that which bonds chemically to the clusters) was sublimed away from the cluster surface given the annealing temperature. Sulphur is long known to sublime at temperatures well below 100 °C [22, 23].

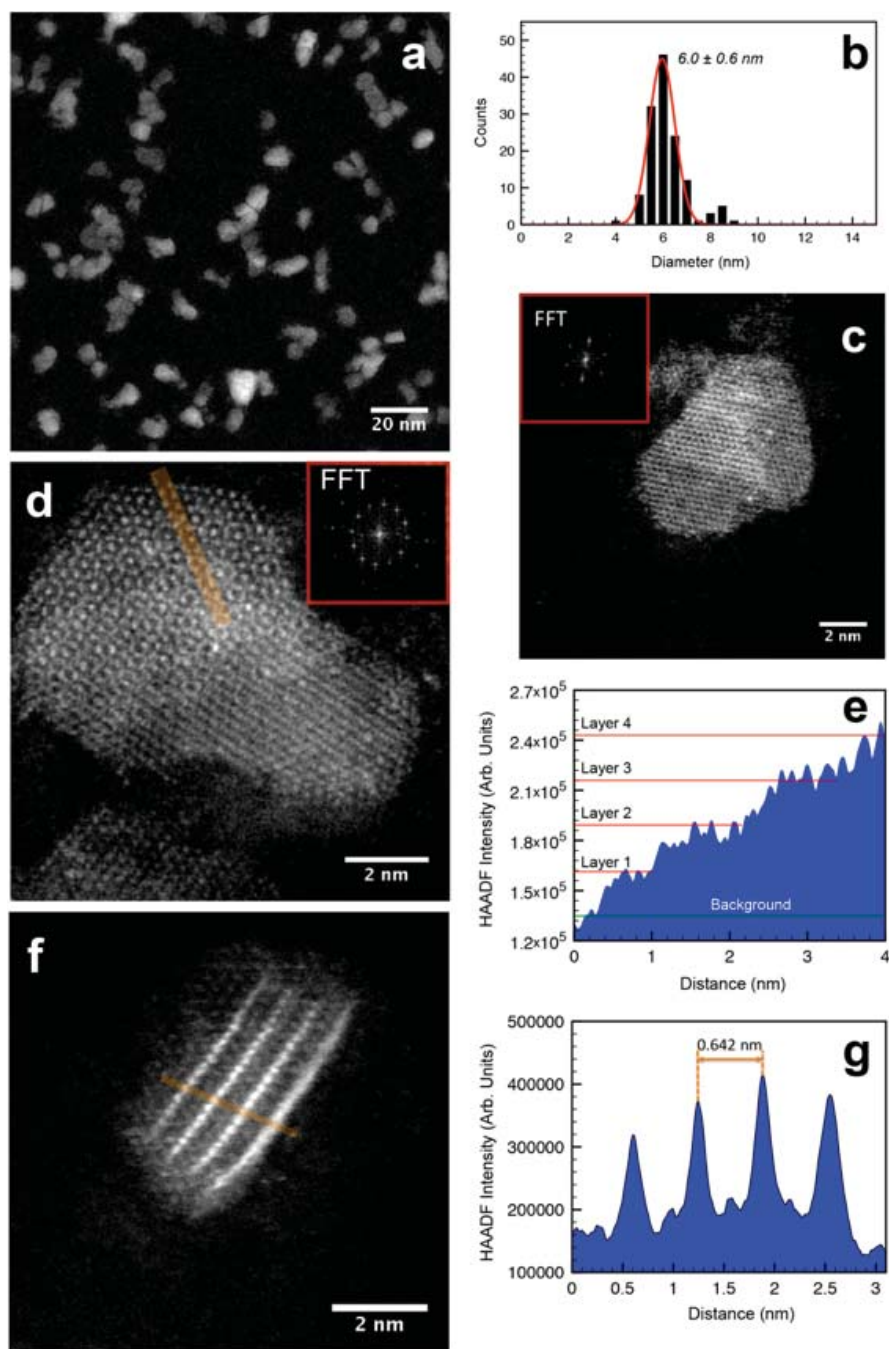


Figure 4.7 STEM images of (a) (MoS₂)₁₀₀₀ clusters with sulphur addition and annealing at low magnification. (b) Size distribution of independent clusters. (c) Bilayered MoS₂ cluster with FFT pattern. (d) MoS₂ cluster with four layers with FFT pattern, indicating a $\sim 30^\circ$ rotation angle between the first (from bottom) and the second layer. (e) HAADF intensity line profile of the line in (d). (f) A side-on MoS₂ cluster with a 0.64 nm interlayer spacing and (g) its HAADF intensity line profile of the line in (e).

The STEM images and HAADF intensities of clusters subjected to this additional treatment are presented in Figure 4.7. Compared with the as-deposited clusters (Figure 4.2a), the STEM image at low magnification (Figure 4.7a) reveals that the “sulphurised” and annealed clusters become larger. The size distribution shown in Figure 4.7b gives a peak diameter of 6.0 nm. The fragmental clusters (3.8 nm, Figure 4.2b) may recombine with each other in this treatment leading to the absence of the peak of smaller size in Figure 4.7b. STEM images at high magnification indicate that most of the clusters have rather crystalline structures. Figure 4.7c shows a single crystalline MoS₂ cluster with a single set of diffraction spots corresponding to the (100) plane with 0.26 nm spaced. The regular honeycomb pattern shown here originates from the atomic arrangements of Mo and S atoms, which is in agreement with the TEM studies on the MoS₂ nanoparticles made by other methods, e.g. CVD and exfoliation [24, 25]. The intensity profile shows this cluster consists of two, non-identical hexagonal layers; the brighter region in the middle has a bi-layered structure with mono-layer structures on the both sides. While some clusters present this kind of layer stacking with the hexagonal atomic structure, some clusters show misorientation between layers, leading to a Moiré pattern. The cluster shown in Figure 4.7d consists of 4 layers; the layer step changes can be seen in the STEM image and are confirmed by the HAADF intensity line profile shown in Figure 4.7e. Layer 2 has a ~30° rotation angle with respect to layer 1, which is indicated by the STEM image and the two sets of diffraction spots in the FFT pattern. As in the case of as-deposited samples, we found a minority of side-on MoS₂ cluster structures after sulphur addition and annealing (Figure 4.7f). This suggests that sulphur deficiency does not deteriorate the layered nature of MoS₂, in agreement with the simulation first-principles study done by Wu et al. [26], and sulphur addition and annealing do not affect layer arrangement of the clusters and that the structural modification into crystalline clusters mainly takes place within the 2D layers.

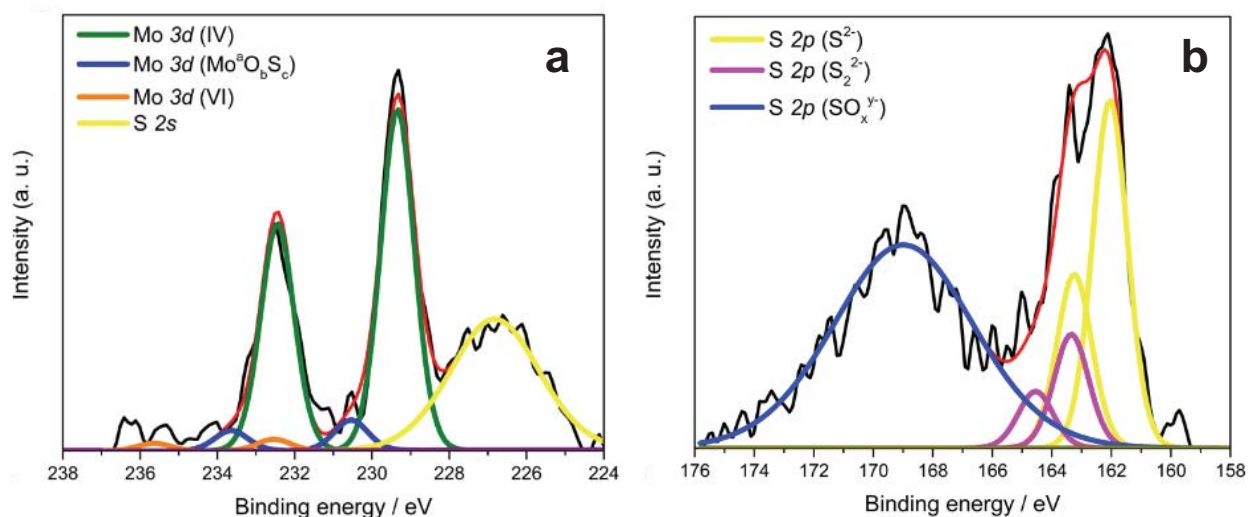


Figure 4.8 Detailed Mo 3d (a) and S 2p (b) XPS spectra of sulphurised, annealed (MoS₂)₁₀₀₀ clusters. Labels: raw spectra (black), cumulative peak fit (red), Mo⁴⁺ 3d_{5/2:3/2} (green), Mo^aO_bS_c 3d_{5/2:3/2} (blue), Mo⁶⁺ 3d_{5/2:3/2} (orange), S 2p_{3/2:1/2} (S²⁻, yellow) and S 2p_{3/2:1/2} (S₂²⁻, magenta).

Detailed XPS spectra on the sulphur-evaporated and annealed (MoS₂)₁₀₀₀ clusters are shown in Figure 4.8. The Mo spectra (Figure 4.8a) could not be solely deconvoluted into the Mo⁴⁺ 3d_{5/2:3/2} spin-orbit doublet characteristic of MoS₂ materials (binding energies of ~229.8 and ~232.9 eV, respectively). Two additional doublets were needed, ascribed to Mo^aO_bS_c (~231.5 and ~234.6 eV, see ESI for Mo^aO_bS_c definition) and Mo⁶⁺ (~233.1 and ~236.2 eV) oxidation states reported in molybdenum compounds such as molybdenum oxysulfides and MoO₃ [27, 28]. The S spectra (Figure 4.8b) were deconvoluted using two 2p_{3/2:1/2} spin-orbit doublets related to the S²⁻ (~161.3 and ~162.5 eV) and the S₂²⁻ (~162.6 and ~163.8 eV) oxidation states. The XPS measurement gives a Mo⁴⁺/Mo^aO_bS_c: S²⁻/S₂²⁻ ratio of 1: 4.9±0.1, which confirms the sulphur-enrichment in the clusters.

4.5 The Effect of The Sulphur Addition and Annealing Treatment

To further understand the effect of the combined sulphur addition and annealing treatment on the MoS₂ cluster structures, we independently treated as-deposited MoS₂ clusters by annealing or sulphur addition alone. Annealed clusters are illustrated in Figure 4.9a and b, where the clusters present poorly ordered structures confirmed by the diffuse FFT pattern. The most notable change is in the cluster size, which now shows two main peaks at 3.1 nm and 8.9 nm in the size distribution, Figure 4.9c. Thus the 5.5 nm peak in the original size distribution (Figure 4.2b) disappeared. As discussed above, some of the as-deposited (MoS₂)₁₀₀₀ clusters are actually the result of weak binding of several smaller clusters in the gas phase. We envisage that these component clusters are liberated in the annealing process, leading to the 3.1 nm peak in Figure 4.9c or migrating and coalescing with other clusters to generate the 8.9 nm peak. Such a process could account for the dissolution of the main peak in Figure 4.9b and the formation of the two new main peaks in Figure 4.9c.

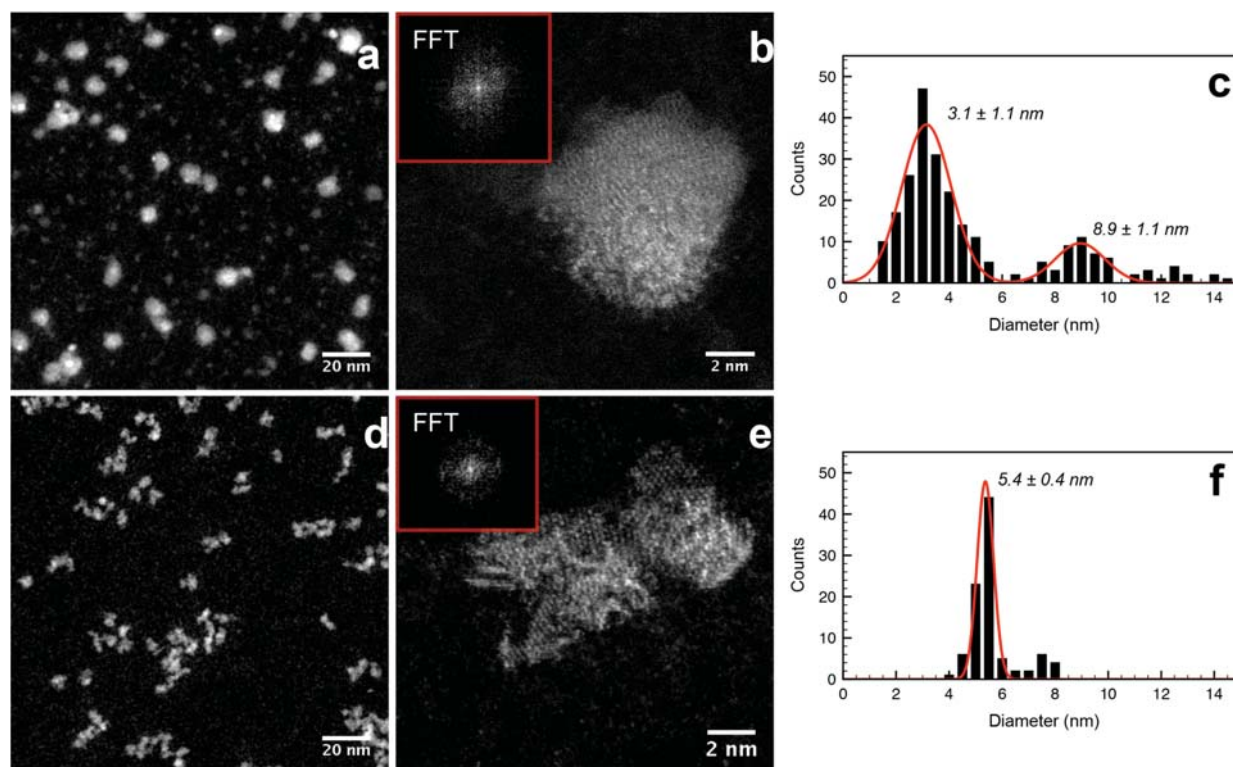


Figure 4.9 STEM images of MoS₂ clusters after (a, b) annealing only and (d, e) after sulphur addition only of as-deposited samples, (MoS₂)₁₀₀₀. (c) and (f) are the corresponding size distributions of the clusters after annealing only and sulphur addition only, respectively.

By contrast with annealing, surface diffusion of clusters and coalescence is rarely observed in the purely sulphurised samples shown in Figure 4.9d. Their size distribution is illustrated in Figure 4.9f showing a similar peak diameter (5.4 nm) as the as-deposited sample (5.5 nm, Figure 4.2b). Note that there is no evidence in the images of a thick film of sulphur on the clusters; we suspect that warming of the sample by radiation from the nearby evaporator is sufficient to induce re-sublimation. These sulphurised MoS₂ clusters (Figure 4.9e) show a partial improvement in crystalline structure, unlike the annealed MoS₂ samples, but not to the same extent as the clusters which are both sulphurised and annealed. We concluded that the

combination of annealing and sulphur addition of as-deposited, amorphous MoS₂ clusters is the best way to create the extended crystalline structures.

It has been reported that the structural damage on a crystalline MoS₂ structure could be induced by the electron beam, where the maximum transferred energy from electron beam with 200 kV (~16 eV for S) is larger than the displacement threshold energy of sulphur atom (~7 eV) [29]. However, the significant damage to the MoS₂ crystalline structure was hardly observed in this work. This is presumably because of a short exposure time to electron beam during taking images (~ 20 s for each image) and a small number of MoS₂ layers. Although it cannot be ruled out the possibility of the electron beam damage on the structure, it does not affect the conclusion through this work.

4.6 Electrocatalytic Activity to HER

The linear sweep voltammograms of as-deposited and sulphur-enriched (MoS₂)₁₀₀₀ clusters are done by Daniel Escalera Lopez and shown in Figure 4.10. The low proton concentration in the electrolyte used ($[H^+] \approx 2 \times 10^{-6} \text{ mol cm}^{-3}$, $\text{pH} \approx 2.7$) is responsible for the diffusion decay peak profile in Figure 4.10a and b, analogous to that found with our previously reported magnetron-sputtered clusters. The as-deposited samples present onset potentials (η_{onset}) of ca. 690 mV for current densities of $j=0.05 \text{ mA cm}^{-2}$, which are ~60 mV positively shifted compared to the recorded η_{onset} for bare glassy carbon. This confirms that even at ultra-low loadings MoS₂ effectively catalyzes the HER. The peak half-maximum overpotentials ($\eta_{\text{half max}}$) and current densities ($j_{\text{half max}}$) metrics previously used to describe the HER catalysis of magnetron-sputtered clusters are found to be ca. 810 mV and 0.31 mA cm^{-2} , respectively. These are in good agreement with the results obtained for (MoS₂)₃₀₀ clusters, which presented a higher cluster loading (ca. $3.5 \mu\text{g cm}^{-2}$) but equivalent surface coverage (~20%) because of the smaller

cluster sizes. Interestingly, such ultra-low loadings of size-selected MoS₂ clusters used in the present work (5% coverage: $\sim 84 \text{ ng cm}^{-2}$, 20% coverage: $\sim 335 \text{ ng cm}^{-2}$) already show HER activities comparable to those of (MoS₂)₃₀₀ clusters with loadings higher by 1 order of magnitude. After sulphur enrichment, all (MoS₂)₁₀₀₀ clusters exhibit remarkable improvements in their HER performance. A consistent 200 mV shift in the HER $\eta_{\text{half max}}$ was found independently of the sample loading

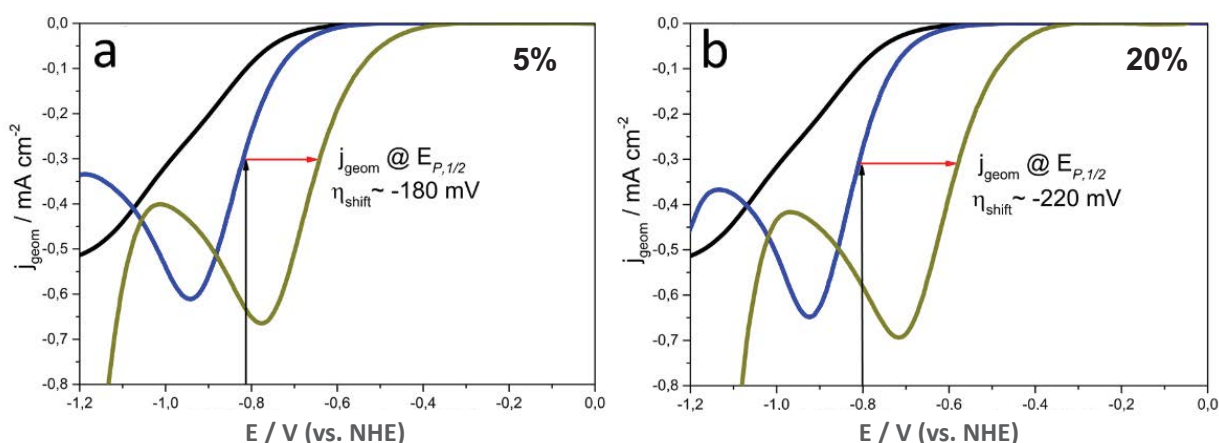


Figure 4.10 Linear sweep voltammograms recorded at 5 mm diameter mirror-polished glassy carbon samples (black) modified with as-deposited (MoS₂)₁₀₀₀ clusters (blue) and sulphurised, annealed (MoS₂)₁₀₀₀ clusters (olive) at surface coverages of 5% (a) and 20% (b).

Tafel analysis of the linear sweep voltammograms shows that the Tafel slopes of all (MoS₂)₁₀₀₀ cluster samples are located in the 143-154 mV dec⁻¹ range irrespective of both loading and sulphur modification, which means the Volmer mechanism applies to all these samples and the electroadsorption of monoatomic hydrogen is the rate-limiting step. This indicates the catalytic mechanism is not affected by the sulphur-addition treatment.

The exchange current density (j_0) analysis presents a $j_0 \approx 8.8 \times 10^{-10} \text{ A cm}^{-2}$ at $\eta_{\text{half max}} = 825 \text{ mV}$ for as-deposited clusters with 5% surface coverage, whereas sulphur-rich clusters present a $j_0 \approx$

2.8×10^{-8} A cm⁻² at an equivalent $\eta_{\text{half max}}$ with the same coverage. For 20% surface coverage, similar enhancements can be found (at $\eta_{\text{half max}} = 814$ mV; $j_0 \approx 5.2 \times 10^{-8}$ vs. 7.9×10^{-10} A cm⁻²). More than 30-fold increase in j_0 indicates improved per-site activities and active site densities: positive shifts in onset potential values under given HER kinetics (i.e. same Tafel slope values) have been related to higher densities of active sites. The ultra-low loadings utilized in this study preclude quantitative comparisons based on the HER metrics commonly cited (η at 10 mA cm⁻² and j_{geom} at 200 mV) in the literature. It is well known that these metrics are heavily affected by the TMD morphologies, catalyst loading, and catalyst layer thickness. Instead, we normalized the j_{geom} values by mass activity (mA mg⁻¹), a metric widely accepted in the noble metal electrocatalysis community. The values obtained at η values as low as 400 mV (close to the HER onset) are ca. 110 mA mg⁻¹ at 5% coverage and ca. 70 mA mg⁻¹ at 20% coverage. For $\eta_{\text{half max}}$ mass activities are ca. 3620 mA mg⁻¹ (as-deposited) and ca. 4010 mA mg⁻¹ (sulphur-added) for 5% coverage; and ca. 980 mA mg⁻¹ (as-deposited) and ca. 1040 mA mg⁻¹ (sulphur-added) for 20% coverage. These values are comparable with the best reported MoS₂ catalysts at 200 mV tested using a high proton concentration electrolyte. This highlights the remarkable activities of the sulphur-added (MoS₂)₁₀₀₀ clusters obtained at very low loadings. The evaluation of the short-term stability of (MoS₂)₁₀₀₀ clusters (20% surface coverage) in HER was carried out by comparing the first and the eleventh LSV measurements. The as-deposited MoS₂ clusters present a 415 mV decay on $\eta_{\text{half max}}$ indicating the high electrochemical instability of the amorphous MoS₂ clusters. In contrast, the sulphur-added MoS₂ clusters are dramatically stable in electrocatalysis with only 30 mV shift on $\eta_{\text{half max}}$. This implies the improved crystallinity of sulphur-added MoS₂ clusters leads to a minor presence of the undercoordinated Mo sites and significantly reduces the MoS₂ leaching.

4.7 Conclusions

In summary, size-selected MoS₂ clusters were produced using a gas condensation, magnetron sputtering cluster source in conjunction with a lateral time-of-flight mass filter and characterised by HAADF-STEM and XPS. The as-deposited clusters on amorphous carbon show layered structure. The sulphur-deficient nature of as-deposited clusters leads to the absence of extended crystalline order in clusters. Besides the laminar clusters, few side-on clusters were found on the support due to the surface defects. A support-effect was found in MoS₂ clusters when they were deposited onto silica film. The size-selected clusters on silica form single- or multi-wall Fullerene-like cage with high stability. In order to obtain well crystalline MoS₂ clusters deposited on amorphous carbon, sulphur-enrichment treatment was conducted to the as-deposited (MoS₂)₁₀₀₀ clusters. A combination of sulphur addition and annealing led to a notable increase in extended crystallinity and a moderate increase in size. The sulphur-rich nature was confirmed by the XPS measurement. Clusters with annealing only show decomposition and coalescence, resulting in both larger and smaller sizes compared with the as-deposited samples, whereas the clusters simply sulphurised retain their size but are only partially crystallised. Thus, to obtain the most crystalline MoS₂ clusters, the combination of annealing and sulphur addition is needed.

The HER measurement shows a clear enhancement to HER activity in sulphur-enriched MoS₂ clusters. The more than 30-fold increases in j_0 value surpasses the HER enhancements in (Ni-MoS₂)₁₀₀₀ hybrid clusters. Cluster benchmarking by mass activity emphasises the remarkable performance of sulphur-enriched (MoS₂)₁₀₀₀ size-selected clusters at the ultra-low loading level. These results are comparable to the state-of-the-art MoS₂-based catalysts, reflecting the significant activities of size-selected MoS₂ clusters obtained at ultra-low loadings, resembling previous enhancements reported for noble metals.

References

- [1] Niu Y, Park S, Palmer R. Modification of deposited, size-selected MoS₂ nanoclusters by sulphur addition: an aberration-corrected stem study. *Inorganics* **2016**, 5(1): 1.
- [2] Escalera-López D, Niu Y, Park SJ, Isaacs M, Wilson K, Palmer RE, *et al.* Hydrogen evolution enhancement of ultra-low loading, size-selected molybdenum sulfide nanoclusters by sulfur enrichment. *Applied Catalysis B: Environmental* **2018**, 235: 84-91.
- [3] Gemming S, Seifert G. Nanocrystals: catalysts on the edge. *Nat Nanotechnol* **2007**, 2(1): 21-22.
- [4] Hinnemann B, Moses PG, Bonde J, Jorgensen KP, Nielsen JH, Horch S, *et al.* Biomimetic hydrogen evolution: MoS₂ nanoparticles as catalyst for hydrogen evolution. *J. Am. Chem. Soc.* **2005**, 127(15): 5308-5309.
- [5] Jaramillo TF, Jorgensen KP, Bonde J, Nielsen JH, Horch S, Chorkendorff I. Identification of active edge sites for electrochemical H₂ evolution from MoS₂ nanocatalysts. *Science* **2007**, 317(5834): 100-102.
- [6] Kibsgaard J, Jaramillo TF, Besenbacher F. Building an appropriate active-site motif into a hydrogen-evolution catalyst with thiomolybdate [Mo₃S₁₃]²⁻ clusters. *Nat. Chem.* **2014**, 6(3): 248-253.
- [7] Yu Y, Huang SY, Li Y, Steinmann SN, Yang W, Cao L. Layer-dependent electrocatalysis of MoS₂ for hydrogen evolution. *Nano Lett.* **2014**, 14(2): 553-558.
- [8] Karunadasa HI, Montalvo E, Sun YJ, Majda M, Long JR, Chang CJ. A molecular MoS₂ edge site mimic for catalytic hydrogen generation. *Science* **2012**, 335(6069): 698-702.
- [9] Wang TY, Liu L, Zhu ZW, Papakonstantinou P, Hu JB, Liu HY, *et al.* Enhanced electrocatalytic activity for hydrogen evolution reaction from self-assembled

- monodispersed molybdenum sulfide nanoparticles on an Au electrode. *Energy & Environmental Science* **2013**, 6(2): 625-633.
- [10] Van der Zande AM, Huang PY, Chenet DA, Berkelbach TC, You Y, Lee GH, *et al.* Grains and grain boundaries in highly crystalline monolayer molybdenum disulphide. *Nat Mater* **2013**, 12(6): 554-561.
- [11] Xie JF, Zhang H, Li S, Wang RX, Sun X, Zhou M, *et al.* Defect-rich MoS₂ ultrathin nanosheets with additional active edge sites for enhanced electrocatalytic hydrogen evolution. *Adv. Mater.* **2013**, 25(40): 5807.
- [12] Cuddy MJ, Arkill KP, Wang ZW, Komsa HP, Krasheninnikov AV, Palmer RE. Fabrication and atomic structure of size-selected, layered MoS₂ clusters for catalysis. *Nanoscale* **2014**.
- [13] Wang ZW, Toikkanen O, Yin F, Li ZY, Quinn BM, Palmer RE. Counting the atoms in supported, monolayer-protected gold clusters. *J. Am. Chem. Soc.* **2010**, 132(9): 2854-2855.
- [14] Wang ZW, Palmer RE. Determination of the ground-state atomic structures of size-selected Au nanoclusters by electron-beam-induced transformation. *Phys. Rev. Lett.* **2012**, 108(24).
- [15] Jian N, Palmer RE. Variation of the core atomic structure of thiolated (Au_xAg_{1-x})_{312±55} nanoclusters with composition from aberration-corrected HAADF STEM. *The Journal of Physical Chemistry C* **2015**, 119(20): 11114-11119.
- [16] Jian N, Stapelfeldt C, Hu KJ, Froba M, Palmer RE. Hybrid atomic structure of the schmid cluster Au₅₅(PPh₃)₁₂C₁₆ resolved by aberration-corrected STEM. *Nanoscale* **2015**, 7(3): 885-888.

- [17] Pratontep S, Carroll SJ, Xirouchaki C, Streun M, Palmer RE. Size-selected cluster beam source based on radio frequency magnetron plasma sputtering and gas condensation. *Rev. Sci. Instrum.* **2005**, 76(4).
- [18] von Issendorff B, Palmer RE. A new high transmission infinite range mass selector for cluster and nanoparticle beams. *Rev. Sci. Instrum.* **1999**, 70(12): 4497.
- [19] Escalera-López D, Niu Y, Yin J, Cooke K, Rees NV, Palmer RE. Enhancement of the hydrogen evolution reaction from Ni-MoS₂ hybrid nanoclusters. *ACS Catalysis* **2016**, 6(9): 6008-6017.
- [20] Shi Y, Zhou W, Lu AY, Fang W, Lee YH, Hsu AL, *et al.* Van der waals epitaxy of MoS₂ layers using graphene as growth templates. *Nano Lett.* **2012**, 12(6): 2784-2791.
- [21] Fei L, Lei S, Zhang WB, Lu W, Lin Z, Lam CH, *et al.* Direct tem observations of growth mechanisms of two-dimensional MoS₂ flakes. *Nat. Commun.* **2016**, 7: 12206.
- [22] Tucker RP. Notes on the sublimation of sulfur between 25 degrees and 50 degrees C. *Ind. Eng. Chem.* **1929**, 21: 44-47.
- [23] Grugel RN, Toutanji H. Sulfur “concrete” for lunar applications – sublimation concerns. *Adv. Space Res.* **2008**, 41(1): 103-112.
- [24] Ji Q, Zhang Y, Gao T, Zhang Y, Ma D, Liu M, *et al.* Epitaxial monolayer MoS₂ on mica with novel photoluminescence. *Nano Lett.* **2013**, 13(8): 3870-3877.
- [25] Muscuso L, Cravanzola S, Cesano F, Scarano D, Zecchina A. Optical, vibrational, and structural properties of MoS₂ nanoparticles obtained by exfoliation and fragmentation via ultrasound cavitation in isopropyl alcohol. *The Journal of Physical Chemistry C* **2015**, 119(7): 3791-3801.
- [26] Wu Z, Wang Y, Ye Y, Feng J, Zhang M, Luo Y, *et al.* First-principles study of monolayer MoS₂ with deficient and excessive Mo_n and S_n (n = -3→3) clusters on 5×5 supercells. *Computational Materials Science* **2016**, 121: 124-130.

- [27] Schmidt E, Sourisseau C, Meunier G, Levasseur A. Amorphous molybdenum oxysulfide thin-films and their physical characterization. *Thin Solid Films* **1995**, 260(1): 21-25.
- [28] Gruenert W, Stakheev AY, Feldhaus R, Anders K, Shpiro ES, Minachev KM. Analysis of molybdenum(3d) XPS spectra of supported molybdenum catalysts: an alternative approach. *The Journal of Physical Chemistry* **1991**, 95(3): 1323-1328.
- [29] Garcia A, Raya AM, Mariscal MM, Esparza R, Herrera M, Molina SI, *et al.* Analysis of electron beam damage of exfoliated MoS₂ sheets and quantitative HAADF-STEM imaging. *Ultramicroscopy* **2014**, 146: 33-38.

Chapter 5

Reduced Sintering of Mass-Selected Au Clusters on SiO₂ by Alloying with Ti

Most of the work in this chapter has been represented in my publications of “**Niu Y**, Schlexer P, Sebok B, Chorkendorff I, Pacchioni G, Palmer RE. Reduced sintering of mass-selected Au clusters on SiO₂ by alloying with Ti: an aberration-corrected STEM and computational study. *Nanoscale* 2018, 10(5): 2363-2370” [1]. The draft of the published paper was written by me (cluster fabrication and STEM study), Bela Sebok (XPS and LEIS analysis) and Philomena Schlexer (DFT calculation). Most of the text, figures and tables have also been used in the publication.

5.1 Introduction

Looking at the experimentally measured catalytic activities of Au nanoparticles on different supports in the CO oxidation reaction, two main conclusions can be drawn. The Au nanoparticles are not active above a size of approx. 5 nm and on some oxide supports, such as SiO₂, they are not active at all, regardless of size [2]. Although supported Au nanoparticles have genuine potential in technological applications, a major issue hindering their implementation is rapid sintering. It has been shown that Au atoms are mobile and can migrate to form 3D islands on a TiO₂ surface even at 150-160 K [3, 4]. Also on silica, Au particles tend to sinter quickly, unless defects are present on the surface to which the Au particles bind more

strongly [5]. However, the defects have to be present on the surface before the cluster deposition and are unlikely to be formed in situ [6]. Figure 5.1 illustrates the two principal sintering mechanisms for supported inter-particles: Ostwald ripening and Smoluchowski ripening. Several studies were made to investigate the sintering mechanism of supported Au nanoparticles. According to the work of Yang et al. [7], Au clusters on TiO_2 sinter by Ostwald ripening between 300 K and 410 K and the sintering is accelerated by the presence of a mixture of CO and O_2 . The sintering modes of mass-selected Au clusters deposited on amorphous carbon were studied by Hu et al. [8] They found that the sintering process is size-dependent; $\text{Au}_{561\pm13}$ and $\text{Au}_{923\pm20}$ clusters exhibit Ostwald ripening, whereas $\text{Au}_{2057\pm45}$ ripens through cluster diffusion and coalescence (Smoluchowski ripening) [8].

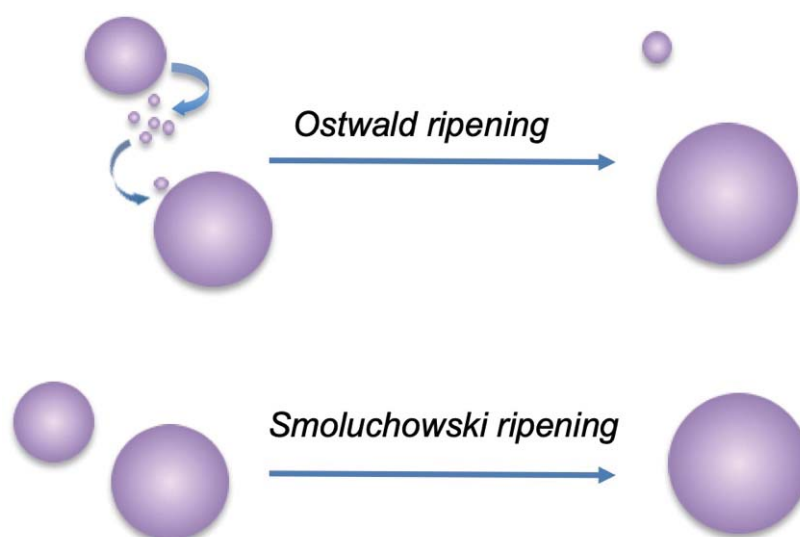


Figure 5.1 Schematic illustration of the two sintering mechanisms of supported particles: Ostwald ripening, in which large particles grow into larger ones at the expense of smaller particles through atom/small cluster diffusion; and Smoluchowski ripening, in which whole particles diffuse and coalesce with neighboring particles.

The stabilisation of supported nanoparticles against sintering has attracted significant research effort [9]. Two pathways are usually described: alloying the particles or encapsulating them within an oxide or organic shell. The latter may hinder the use of nanoparticles in catalytic

applications because of surface passivation, but alloying may provide a route to nanoparticles which are both stable and active. In particular, the investigations of mass-selected alloy nanoparticles synthesised in the gas phase have already shown the unique properties of such materials. Examples include increased activity in the oxygen reduction reaction (ORR) for the case of Pt_xY and Pt_xGd nanoparticles as a result of strain [10, 11] and the dynamic behaviour of CuZn nanoparticles under methanol synthesis reaction conditions [12]. With regards to sintering, it has been shown that alloying Au with Ir, Cu or Ag increases the stability of chemically synthesised nanoparticles on oxide supports [13-19]. However, studies of the effects of alloying on the stability of mass-selected nanoparticles against sintering have lacked to date. Here we show that the sintering rate of mass-selected Au/Ti alloy clusters is much lower than that of mass-selected pure Au clusters on silica. The composition of the clusters was characterised by X-ray Photoelectron Spectroscopy (XPS) and Low Energy Ion Scattering (LEIS), while aberration-corrected Scanning Transmission Electron Microscopy (STEM) was used to investigate the sintering process via direct real space imaging with atomic resolution. Complementarily, *ab initio* calculations confirm stronger binding between alloyed Au/Ti clusters and the SiO_2 surface compared with pure Au clusters.

5.2 Materials and Methods

Au_{2057} (405,229 amu) and Au/Ti (400,000 amu) clusters were produced with a DC magnetron sputtering, gas condensation cluster beam source (Chapter 2) from Au (PI-KEM, 99.99%) and Au/Ti (PI-KEM, 50/50 at%, 99.99%) targets, respectively. The clusters with a specific mass were selected by a lateral time-of-flight mass filter before deposition onto the support with a kinetic energy of approx. 0.5 eV/atom. The mass-selected clusters were deposited onto thin silica films suspended on copper TEM grids (EMS, USA) with a loading of approx. 10%

(projected surface area coverage), i.e., approx. 10% of the surface covered by clusters. Then the clusters were imaged with 200 kV aberration-corrected STEM in HAADF mode after transfer under atmospheric conditions.

The clusters were also deposited onto the reaction zone of micro-reactor described in Chapter 2 (solid Si substrates terminated with a 50 nm thermally grown SiO₂ layer) with the same loading as on TEM grids for CO oxidation measurements. An Ar⁺ beam from the cluster source was used to clean the micro-reactor and create surface defects to anchor the clusters with a beam current of ~1 nA for ~500 s (at 1000 eV Ar⁺). The micro-reactor samples were then transferred under atmospheric conditions to DTU for CO oxidation measurement, XPS characterisation (non-monochromatized Mg K α line from a SPECS XR50 x-ray gun, using an OMICRON NanoSAM 7 channel energy analyser) and LEIS measurement (1 KeV He⁺ from an Omicron ISE100 ion gun using the same energy analyser). The CO oxidation measurement was performed in 1 bar of O₂:CO=4:1 with the temperature gradient between room temperature and 370 K (100°C), meanwhile the CO, O₂ and CO₂ signal was recorded with QMS. In this research, the ratio of O₂/CO is not a crucial factor since a full conversion of CO is not expected. In order to study the stability of the clusters, the micro-reactor samples were heated in 1 bar of O₂:CO=4:1 to 100°C. Then XPS and LEIS were conducted before and after heating to investigate the surface composition of the clusters and the effect of the heating.

Density functional theory (DFT) calculations were carried out by Philomena Schlexer (University of Milano-Bicocca) with the Vienna Ab Initio Simulation Package (VASP 5.2) [20-23] using the Perdew, Burke and Ernzerhof (PBE) exchange-correlation functional [24, 25]. Electron-ion interactions were described via the projector augmented wave (PAW) method [26, 27]. A periodic fully hydroxylated α -quartz (001) surface was used to represent the silica surface [28]. A (3 \times 3) surface supercell was used with lattice parameters of $a = b = 15.11 \text{ \AA}$ and $\gamma = 120^\circ$ and with a slab thickness of 9 layers of [SiO₄] tetrahedra. The slabs were separated

by more than 20 Å of vacuum to ensure enough space for the metal clusters. Wave functions were expanded in a plane wave basis up to a kinetic energy of 400 eV. A Γ -centred K-point grid in the Monkhorst-Pack scheme [29] was used, which was set to the Γ -point. As dispersion forces can be important for the cluster-support interaction, the semi-empirical dispersion correction proposed by Grimme [30] (known as the DFT-D2 approach) was applied. As the DFT-D2 approach is assumed to overestimate the dispersion in oxides, we changed the C_6 and R_0 parameters as suggested by Tosoni and Sauer [31]. The resulting approach is called DFT-D2'. Atomic charges q were determined via the Bader decomposition scheme [32-34]. The adsorption energies of the clusters, E_{ADS} , are defined in equation 5.1, where $E(\text{Au}_x\text{Ti}_y)$ are the metal clusters in the gas-phase and S is the support.

$$E_{\text{ADS}} (\text{Au}_x\text{Ti}_y/\text{S}) = E(\text{Au}_x\text{Ti}_y/\text{S}) - E(\text{Au}_x\text{Ti}_y) - E(\text{S}) \quad (5.1)$$

5.3 STEM Study of the Sintering Process

The mean diameters of Au_{2057} and Au/Ti (400k amu) clusters deposited onto thin silica film were measured, based on projected surface area, and found to be 4.07 nm and 3.94 nm, respectively. The shape of Au_{2057} clusters can be obtained from the relationship between the cluster diameter (D) and the number of Au atoms (N) [35]. The shape of the Au cluster would be pseudospherical, if their $D \sim N^{1/3}$ relations correspond with the spherical geometric model, $D_s = \kappa N^{1/3}$. Here, $\kappa = 0.328$ nm, is calculated from the experimental data [36]. This value is corresponding to twice of the Wigner-Seitz radius, $r_{\text{ws}} = 0.165$ nm [37]. The diameters of the Au_{2057} clusters fit a quasi-spherical geometric model well, indicating that they do not relax substantially to a hemispherical shape on the surface.

To evaluate whether the addition of Ti enhances the stability of the alloy clusters compared with the pure Au clusters, and to shed light on the sintering mechanism(s), the process of

sintering induced by electron beam irradiation was investigated with the aberration-corrected STEM. Figure 5.2 shows sequential images of Au and Au/Ti cluster dimers exposed to the electron beam.

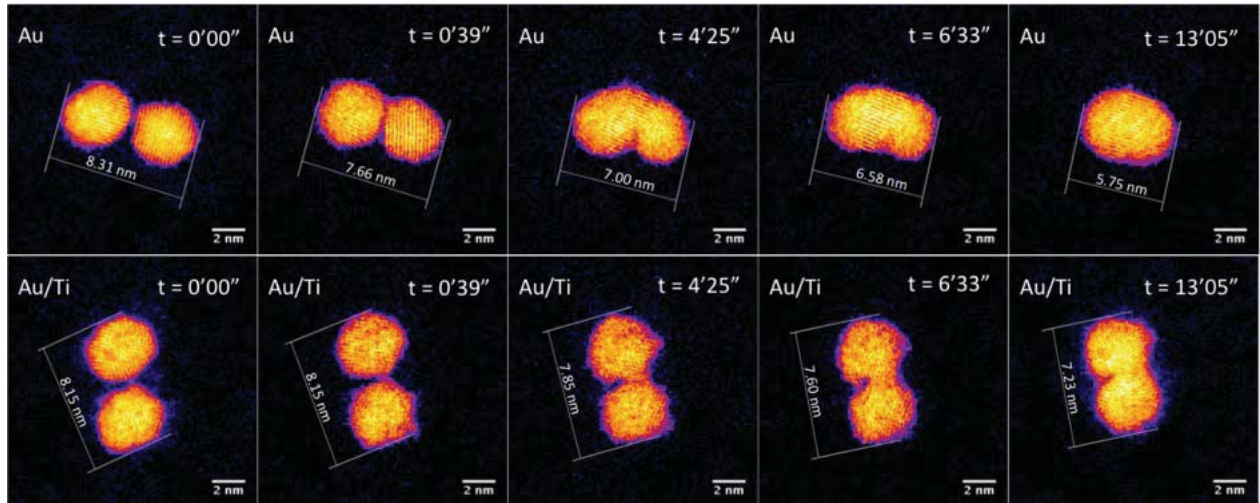


Figure 5.2 STEM images of dimers of Au₂₀₅₇ and of Au/Ti clusters continuously exposed to electron beam irradiation, with an acquisition time of 1.3 seconds per frame and a dose of $6.3 \times 10^3 \text{ e}^-$ per Ångström² per frame. At the beginning of imaging, the gap sizes between the Au₂₀₅₇ and Au/Ti cluster pairs are ~0.30 nm and ~0.25 nm, respectively.

The observed sintering process of the Au clusters can be divided into two phases according to the STEM images and the change of the measured major axis of the Au dimer. In the first phase, the two Au clusters are seen to move toward each other once they are exposed to the electron beam driven by surface plasmon coupling [38, 39], which can be confirmed by the major axis of the Au dimer shrinking from 8.31 nm to 7.66 nm after 39 s, as plotted in Figure 5.3. The cluster migration can be clearly observed in Figure 5.4, in which a more significant gap (~0.75 nm) lies in between the two Au clusters. The cluster migration leads the two initially separated clusters to make contact with each other. Afterwards, in the second phase, a process of coalescence, presumably driven by the peripheral atom diffusion, decreases the surface area of

the dimer. Two different shrink rates of the major axis of the dimer can be found in these two phases of sintering, which are ~ 1.00 nm/min and ~ 0.17 nm/min for the first and second phases, respectively (Figure 5.3). Thus, the sintering behaviour of the Au dimer starts at a relatively high rate with the two clusters quickly migrating towards each other. After about 50 s, once the clusters collide, the second and slower phase of sintering begins, and the rate of peripheral Au atom diffusion regulates the rate of sintering. In the case of the Au₂₀₅₇ clusters, 8 pairs of Au cluster dimers were imaged with the STEM, and 6 pairs of them showed similar sintering behaviour as that discussed above. The clusters in the other 2 pairs of dimers with a gap size of ~ 0.8 nm in between were merely found to move away from each other during imaging.

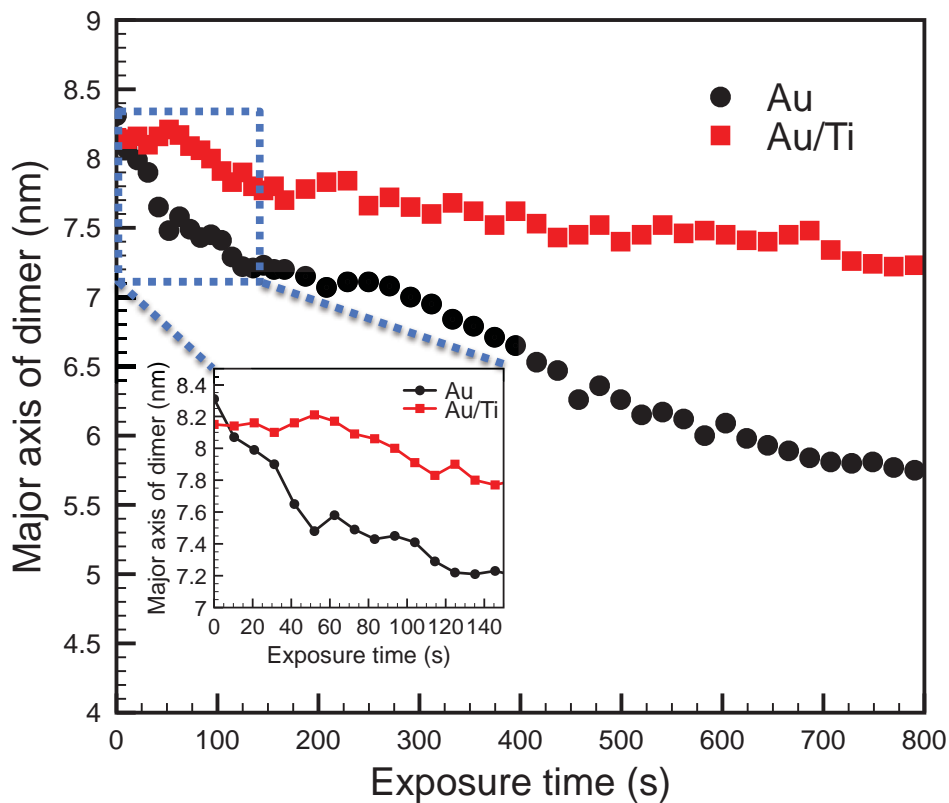


Figure 5.3 The length of the major axis of the cluster dimers as a function of the time of exposure to the electron beam. The inset shows an enlarged view of the graph in the blue square.

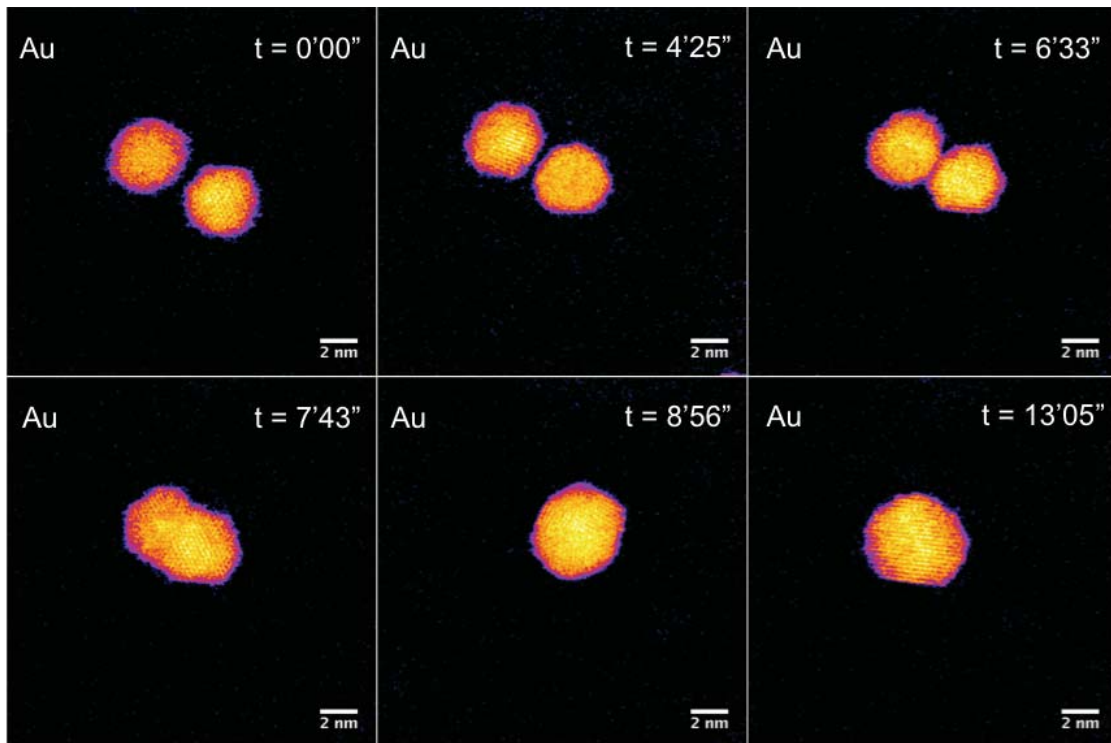


Figure 5.4 Sintering process of Au_{2057} dimer continuously exposed to electron beam irradiation with acquisition time of 1.3 seconds per frame and a dose of $6.3 \times 10^3 \text{ e}^-$ per \AA^2 per frame. At the beginning of imaging, the gap size is $\sim 0.75 \text{ nm}$.

Compared with the Au clusters, the Au/Ti clusters show different sintering behaviour, although once more it can be divided into two phases. In the first phase, the Au/Ti clusters remain at their original positions instead of quickly migrating towards each other like the Au clusters. Thus, the Au/Ti cluster dimer retains the same length of major axis (8.15 nm) after being exposed to the electron beam for 39 s. In this first phase, only peripheral atom diffusion is found. However, once diffusing atoms found in the gap between the two clusters make a first physical connection between the clusters, the second phase of sintering is initiated. In this phase, coalescence takes place around the bridge formed in between, but the coalescence rate here (0.08 nm/min) is much lower than that of the Au cluster dimer, Figure 5.3. This can also be confirmed by the sintering process of the connected Au dimer and Au/Ti dimer illustrated in

Figure 5.5 and 5.6, respectively. The two Au or Au/Ti clusters are already connected with each other by the atoms in between before exposed to the electron beam, and a much slower coalescence rate presents in the case of Au/Ti dimer.

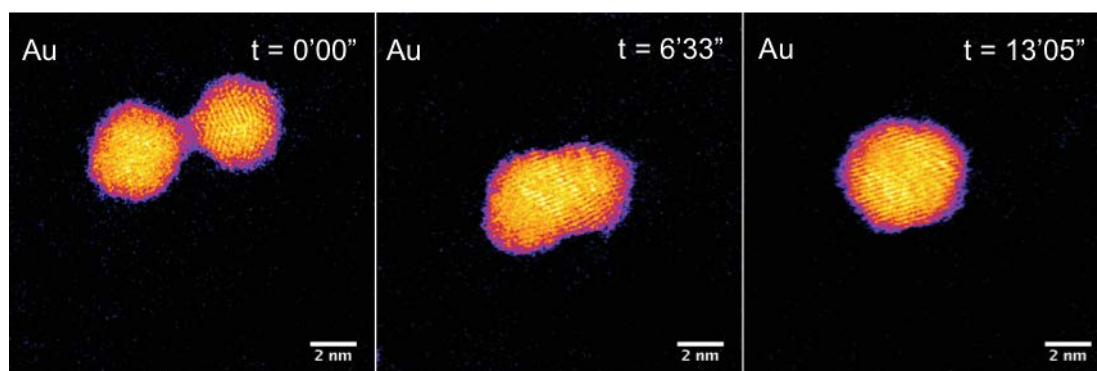


Figure 5.5 Sintering process of Au₂₀₅₇ dimer continuously exposed to electron beam irradiation with an acquisition time of 1.3 seconds per frame and a dose of 9.8×10^3 e⁻ per Angstrom² per frame. The two clusters are already connected with each other at the beginning and quickly coalesce into one cluster.

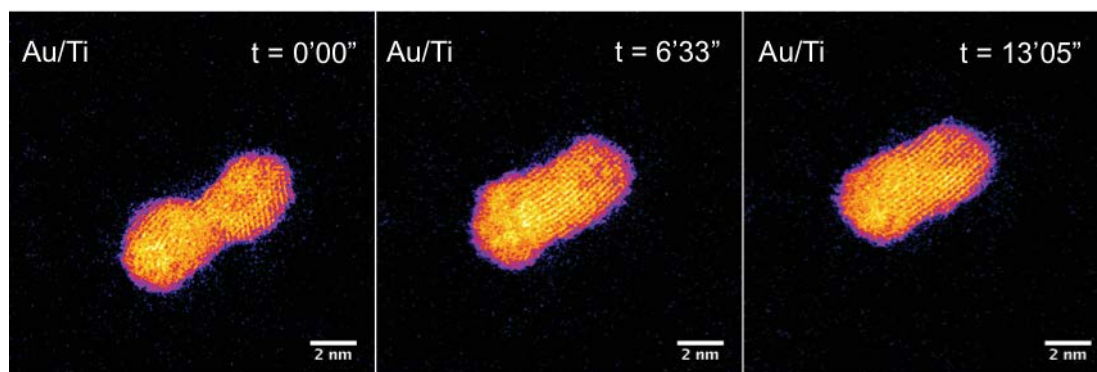


Figure 5.6 STEM images of Au/Ti (400k amu) cluster dimer with two connected clusters continuously exposed to electron beam irradiation with an acquisition time of 1.3 seconds per frame and a dose of 9.8×10^3 e⁻ per Angstrom² per frame.

The different sintering behaviour of Au/Ti clusters compared with Au clusters on silica can be attributed to the strong interaction between Ti and the lattice oxygen of the silica support, which

tends to anchor the clusters in the dimer against sintering. However, the anchoring effect is insufficient to prevent coalescence once two clusters come into contact, so it can slow down the coalescence process but cannot prevent it completely. If the distance between two neighbouring clusters is large enough (see below) that the diffusing atoms cannot “build a bridge” between them, then sintering is exceptionally slow.

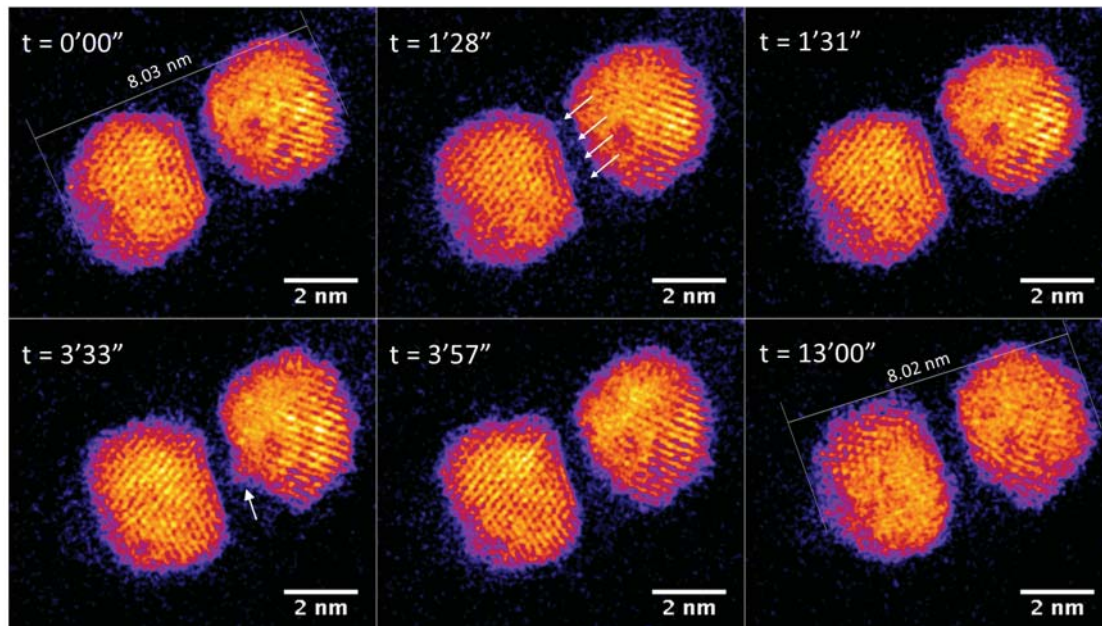


Figure 5.7 STEM images of Au/Ti cluster dimers, with a larger gap (~ 0.65 nm) between than Figure 3, continuously exposed to electron beam irradiation with an acquisition time of 1.3 seconds per frame and a dose of 9.8×10^3 e⁻ per Angstrom² per frame.

Figure 5.7 (and Figure 5.8) shows an Au/Ti cluster dimer with a slightly larger gap than that in Figure 5.2. It can be seen that the two clusters do not sinter after electron exposure for as long as 13 min, and basically, the major axis of this dimer retains the same value. Peripheral atom diffusion is again found during electron exposure. At 1 min 28 s, the atoms highlighted by arrows can be found located between the two clusters, and then disappear 3 s later by moving away from the dimer area or binding to one of the two clusters. It is further observed that the

cluster on the right exhibits a transient asperity due to the accumulation of diffusing atoms at 3 min 33 s. However, the distance between the clusters is too large for a contact bridge to be formed, and the asperity has decayed at 3 min 57 s. This confirms that sintering does not happen between Au/Ti clusters if the cluster distance is too large for the diffusing atoms to build a bridge in between. In future, experimental studies of hundreds of such dimer pairs may lead to the precise measurement of a critical distance for sintering by bridge formation, dependent on temperature and other key parameters (including in the case of the electron beam experiments, the current). In the case of Au/Ti clusters, 14 pairs of Au/Ti clusters dimers were imaged with STEM, and all of them showed similar behaviour against sintering.

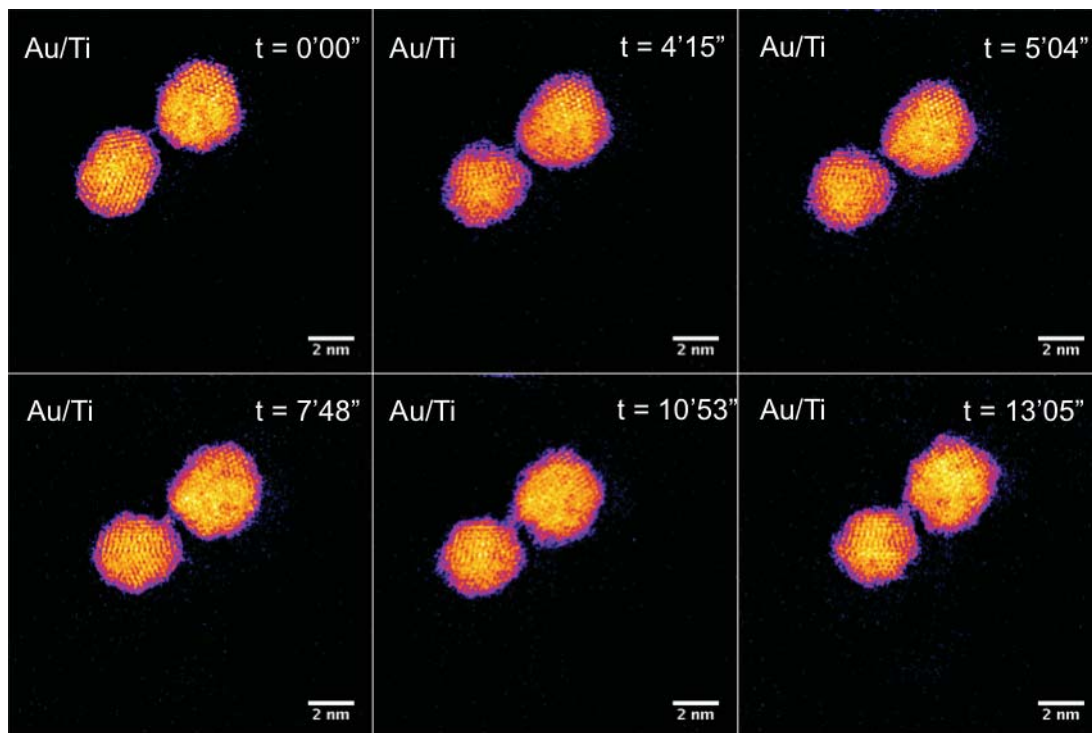


Figure 5.8 STEM images of Au/Ti (400k amu) cluster dimer continuously exposed to electron beam irradiation with an acquisition time of 1.3 seconds per frame and a dose of $9.8 \times 10^3 \text{ e}^-$ per Angstrom² per frame. The gap size is $\sim 0.60 \text{ nm}$ at the beginning of imaging.

5.4 XPS and LEIS of the clusters

XPS was used to provide information on the composition of the deposited clusters. Typical XPS spectra are shown in Figure 5.9 for both the Au₂₀₅₇ and Au/Ti clusters deposited on micro-reactors, as received after transport under atmospheric conditions, and also after heating in a mixture of O₂ and CO in order to simulate the effect of CO oxidation conditions. In all samples, the Si in the SiO₂ binding state, originating from the substrate, can be detected. Traces of carbonaceous contaminants from atmospheric exposure are also visible in the spectra. In case of the Au₂₀₅₇ cluster sample, no significant changes are visible in the XPS spectra taken before and after heating in O₂/CO (Figure 5.9A). In the case of the Au/Ti clusters, the relative intensity of the Au signal compared with the Si signal (normalized peak size) in the spectrum decreases after heating. This is consistent with a segregation process in which more Ti is drawn to the cluster surface, which is underlined by the change of the Au:Ti ratio determined from the spectra. The as-received clusters show a surface Au:Ti ratio of 60:40, while after heating the ratio is approx. 40:60.

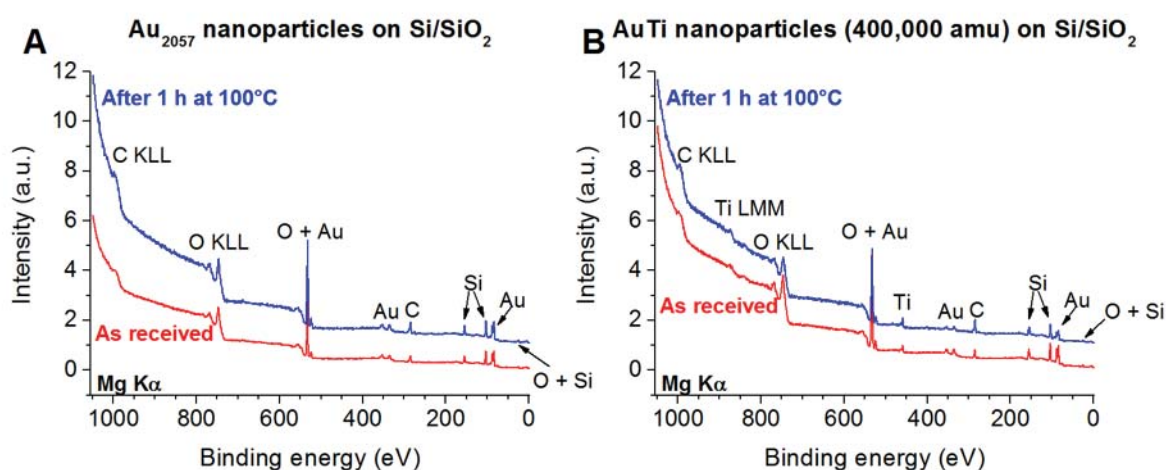


Figure 5.9 XPS spectra of Au₂₀₅₇ (A) and Au/Ti (B) clusters deposited on Si/SiO₂ slabs before and after 100°C for 1 h in 1 bar of O₂:CO=4:1 mixture. Spectra were calibrated for Au 4f_{7/2}

line to appear at the binding energy of 84 eV and were normalised with the area of the Si 2s peak. The plots were offset in y-direction for better visibility.

The binding state of Ti in Au/Ti clusters were revealed by the surface detailed spectra of the Ti 2p region shown in Figure 5.10. After transporting under atmospheric conditions the Ti is oxidized and present on the surface as TiO₂ which does not change after heating under a gas mixture of O₂ and CO. However, the relative amount of Ti compared to Si is increasing. This could be the result of a segregation process and the enrichment of the outer layers of the clusters with Ti.

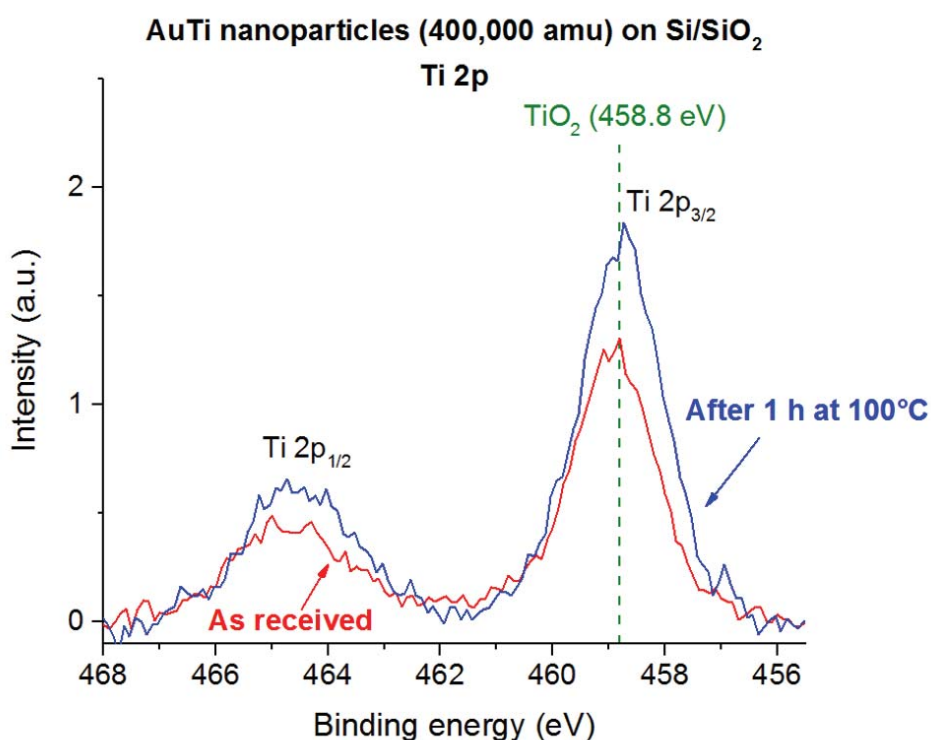


Figure 5.10 Detailed XPS spectra of the Ti 2p region recorded before (A) and after (B) 100°C for 1 h in 1 bar of CO/O₂ in case of the sample having Au/Ti mass-selected clusters deposited. The spectra were shifted to give an Au 4f_{7/2} binding energy of 84 eV and were normalised with the area of the Si 2s peak.

In order to further investigate the surface of the samples, LEIS spectra were recorded (Figure 5.11) characterising the outermost layer of the sample surface. In both Au and Au/Ti cluster samples, O, Si and Au are detectable on the surface before heating, as expected for Au-containing clusters deposited on a SiO₂ surface. In the case of the sample with Au₂₀₅₇ clusters (Figure 5.11A), small additional contaminant(s) can be detected having a mass of approx. 39 amu (Cl, K or Na), which could originate from the handling of the sample. In the case of Au/Ti clusters (Figure 5.11B), after heating the samples, the Si and O peaks disappear from the spectra. As XPS confirms the presence of SiO₂, this disappearance is most probably the effect of carbonaceous contaminants on the surface completely covering the support. Nevertheless, in both samples Au is still clearly visible at the outermost surface.

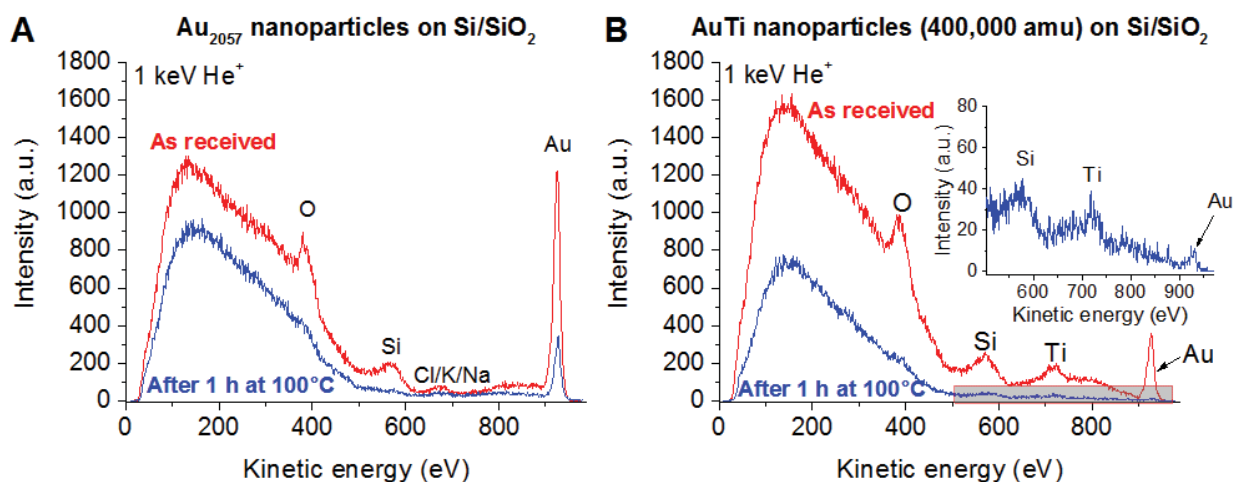


Figure 5.11 LEIS spectra of Au₂₀₅₇ (A) and Au/Ti (B) clusters deposited on Si/SiO₂ slabs before and after (inset) 100°C for 1 h in 1 bar of O₂:CO=4:1 mixture taken with 1 keV He⁺ ions.

Based on the XPS and LEIS measurements, a segregation process upon heating in O₂/CO is changing the surface composition of the Au/Ti clusters, but in line with the computational investigation (see below) Au atoms are still present on the surface, thus opening up the possibility of Au catalysis using the Au/Ti clusters under realistic reaction conditions.

5.5 DFT Calculations of Surface Anchoring

In order to understand more details on the anchoring effect of Au/Ti clusters, DFT calculations were conducted in a collaboration with Philomena Schlexer (University of Milano-Bicocca). The size of the observed particles (around 2000 atoms) is such that we cannot directly model them with DFT calculations. We assumed that it is likely that these particles will adopt shapes derived from a Wulff construction, such as a truncated octahedron dominated by (100) and (111) surfaces. To investigate further the role of Ti atoms against sintering, we considered, amongst others, the adsorption of Au₂₀ and Au₁₀Ti₁₀ tetrahedral clusters which exhibit (111) faces only. While these clusters are smaller than in the experiment, the nature of the bonding with the surface is rather local, and the essence of the interaction between cluster and support is sufficiently well represented by the chosen model. Before adsorbing the clusters on the surface, we optimised the geometries of the free-standing clusters. Our previous study found that size-selected Au₂₀ clusters present a tetrahedral structure when they are soft-landed on amorphous carbon film [40]. Other experimental [41] and computational [42] studies also identify the tetrahedral geometry. In our simulations, we also find that the tetrahedral structure is the lowest energy geometry for free Au₂₀ clusters. For the bimetallic Au₁₀Ti₁₀ cluster, we considered this and other structures, while also testing different distributions of the two elements within the clusters. We considered several cluster isomers, but the potential energy surface (PES) possesses a substantial number of local minima, which cannot be extensively

explored without a global search algorithm. In this respect, our results are representative of some potential structures, but we do not pretend to have identified the global minimum on the PES. We find that the best cluster shape for the Au₁₀Ti₁₀ cluster is not in fact a pyramid, but a compact structure with Ti atoms sitting mainly inside the cluster and a majority of Au atoms in the outer layer.

After the optimisation of the free-standing clusters, the most stable cluster isomers were deposited on the fully hydroxylated α -quartz (001) surface. This choice is dictated by the assumption that under experimental conditions the silica surface is not hydroxyl-free. Fully dehydroxylated silica surfaces can be obtained only after thermal treatment above 600 °C [43], and SiO₂ surfaces get partially hydroxylated even under high vacuum conditions almost instantly [44]. Since our samples are exposed to air, it is likely that a given concentration of OH groups will be present. The density of the OH groups in our model is probably higher than that in the real samples, but no quantitative assessment is possible. The resulting structures are shown in Figure 5.12, and relevant adsorption parameters are summarized in Table 5.1.

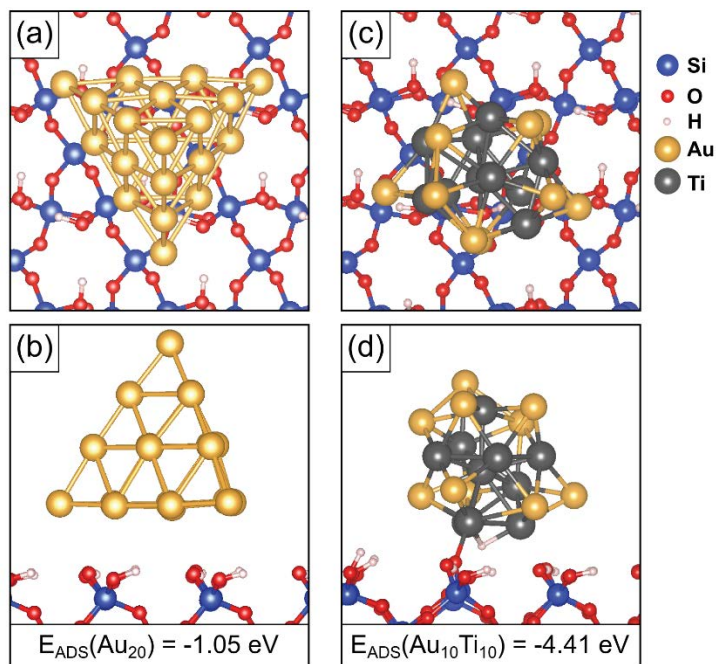


Figure 5.12 (a) Top and (b) side views of Au_{20} supported on the fully hydroxylated α -quartz (001) surface from DFT simulations. (c) Top view and (d) side view of $\text{Au}_{10}\text{Ti}_{10}$ supported on the same surface.

We find that the Au_{20} cluster exhibits a relatively low adsorption energy on the silica surface, only -1.05 eV, Table 5.1. The atoms in the supported Au clusters show an average Bader charge close to zero, indicating the absence of chemical interaction with the surface. The relatively weak binding of the Au cluster on the surface is thus largely due to dispersion forces.

Table 5.1 Adsorption energies E_{ADS} (eV), average Bader charges q_{AVG} (Au or Ti) ($|e|$) on the Au or Ti atoms in the cluster and total Bader charge on the cluster q_{TOT} (Cluster) ($|e|$) from DFT simulations.

	E_{ADS}	$q_{\text{AVG}}(\text{Au})$	$q_{\text{AVG}}(\text{Ti})$	$q_{\text{TOT}}(\text{Cluster})$
Au₂₀ free-standing	---	0	---	0
Au₂₀ on silica	-1.05	0	---	0
Au₁₀Ti₁₀ free-standing	---	-0.77	0.77	0
Au₁₀Ti₁₀ on silica	-4.41	-0.79	0.93	1.39

The Au₁₀Ti₁₀ bimetallic cluster, on the other hand, exhibits a much larger adsorption energy of -4.41 eV. Only around 20% of the adsorption energy is due to dispersion forces. The large adsorption energy is due to a spontaneous local reaction of the cluster with the surface, via hydrogen reverse spillover. This can be seen in the side view in Figure 6 (d). The surface ≡Si-O-H group is split, enabling the H atom to bind to the cluster at a Ti hollow site, while the residual ≡Si-O* group binds to an adjacent Ti atom of the cluster, with a resulting Ti-O bond length of 1.96 Å. This local reaction anchors the cluster to the support via the formation of a ≡Si-O-Au₁₀Ti₁₀ complex. We expect this strong local binding interaction to anchor the AuTi bimetallic clusters to the hydroxylated silica surface, and to operate independently of the cluster size, leading to reduced sintering, as observed in the experiments.

Of course, in the experimental situation, the clusters are exposed to ambient conditions between deposition and the sintering experiments. Thus, we may expect some oxidation of the Ti atoms at the periphery of the Au/Ti clusters, after the removal of the sample out of the deposition chamber, as the XPS confirms that Ti is present on the surface in the form of TiO₂. However, during and directly after the deposition of the clusters in UHV, the metallic clusters can react with the silica surface, as shown in the calculations.

5.6 CO Oxidation on Au and Au/Ti clusters

The CO oxidation measurement was carried out with the micro-reactor decorated with Au₂₀₅₇ or Au/Ti clusters. Figure 5.13 shows the catalytic activity measurement results of the first pair of micro-reactors with Au and Au/Ti clusters. In the case of Au₂₀₅₇ clusters, the gas signals (CO₂, CO and O₂) just fluctuate around the baseline with the changing of temperature with no production of CO₂ and consumption of CO and O₂, which implies that Au₂₀₅₇ clusters are not active to CO oxidation under the test conditions. However, catalytic activity can be found in Au/Ti clusters as shown in Figure 5.13b. The signal of CO₂ production increases and decreases with the temperature ramping, but a deactivation presents with the maximum CO₂ signal slowly going down.

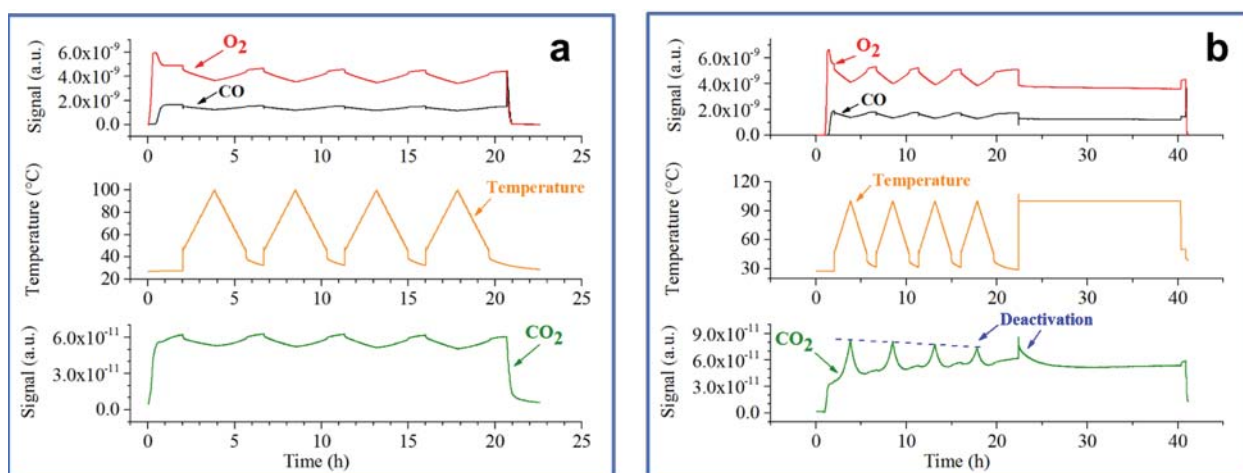


Figure 5.13 CO oxidation activity measurements of the first pair of Au₂₀₅₇ (a) and Au/Ti (400k amu) (b) micro-reactor samples. The measurements were performed in 1 bar of O₂:CO=4:1 with temperature ramping between room temperature and 100°C.

The non-active performance of Au₂₀₅₇ clusters can be explained by the inert support and serious sintering among the Au₂₀₅₇ clusters. On one hand, Au clusters supported on SiO₂ is not a

favourable combination for CO oxidation as shown in Figure 1.17. Figure 5.14 shows the scanning electron microscope (SEM) images of Au₂₀₅₇ and Au/Ti clusters before and after heating under 100°C for 1 h in 1 bar of O₂:CO=4:1 mixture. The according size distributions are shown in Figure 5.15. A severe sintering can be found in Au₂₀₅₇ clusters and leads to a considerable increase of the cluster size, which drives the clusters to permanently lose their catalytic activity. The significant difference in the catalytic performance between Au₂₀₅₇ and Au/Ti clusters implies that the Ti in Au/Ti clusters plays as not just a cluster anchor but also a catalytic participator. The Ti dioxides on the cluster surface may play a role of active oxygen supplier to make the reaction happen. The deactivation of Au/Ti clusters may be due to the accumulation of carbonates on the cluster surface or the surface segregation.

In a period of almost a year, another ~25 micro-reactors were tested for CO oxidation, but none of them showed catalytic activity to CO oxidation. This is due to some technical issues with the CO oxidation measurement set-up at DTU (it turned out that the temperature control and temperature measurement with the micro-reactor were unreliable). Therefore, no constant conclusion can be drawn here in terms of catalytic activity.

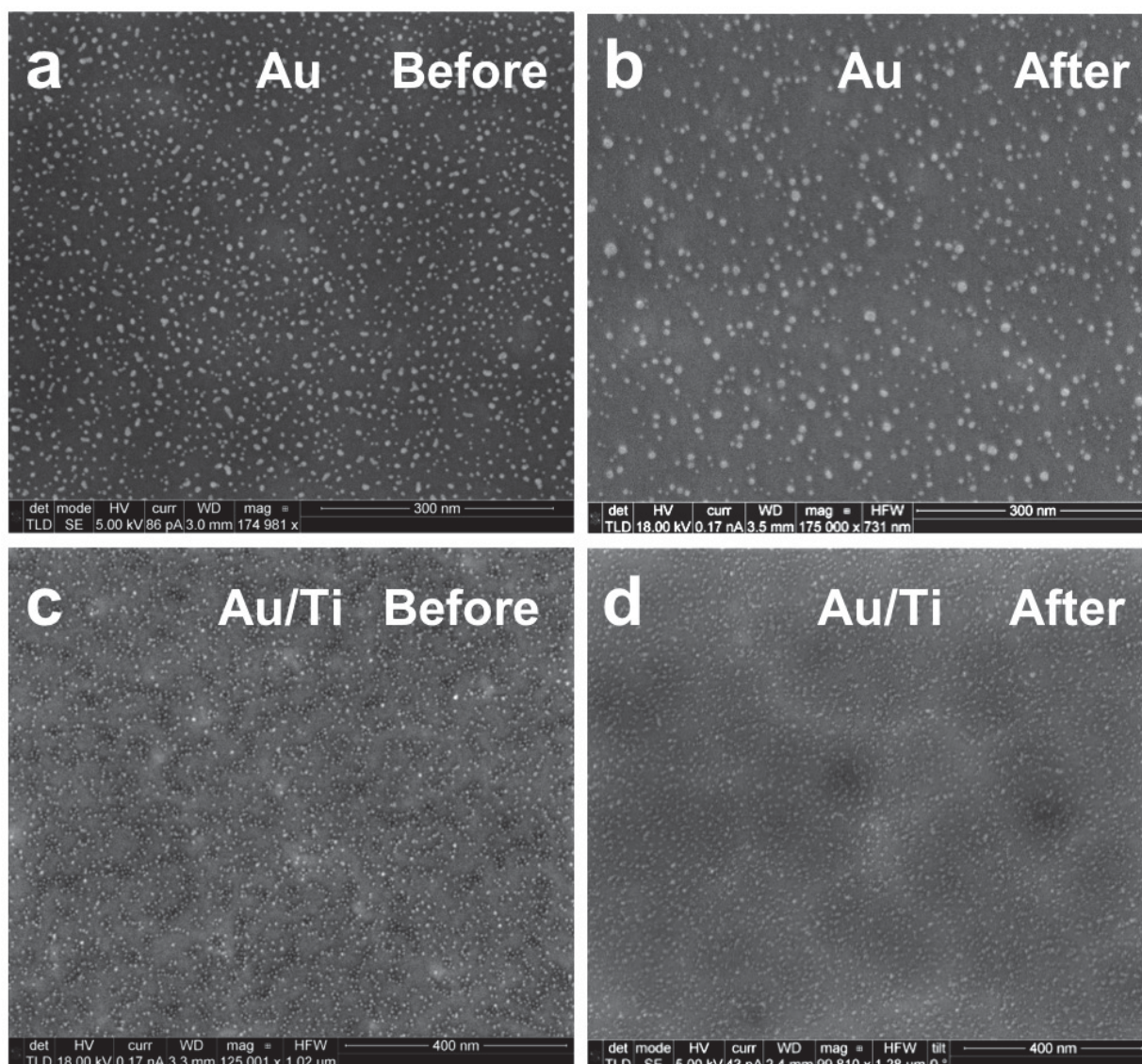


Figure 5.14 SEM images of Au₂₀₅₇ (a, b) and Au/Ti (400k amu) (c, d) clusters before and after 100°C for 1 h in 1 bar of O₂:CO=4:1 mixture.

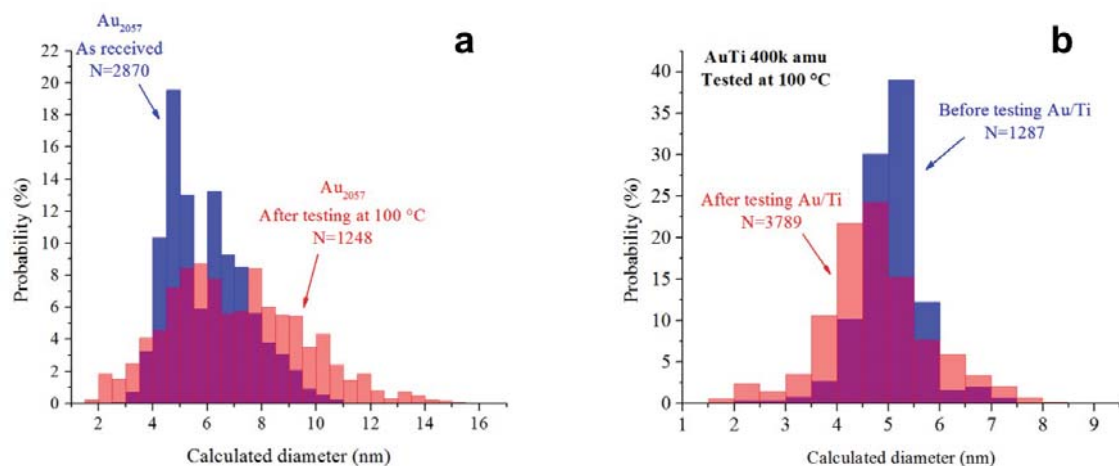


Figure 5.15 Size distributions of Au₂₀₅₇ (a) and Au/Ti (400k amu) (b) clusters before and after 100°C for 1 h in 1 bar of O₂:CO=4:1 mixture.

5.7 Conclusions

Size-selected Au/Ti nanoalloy clusters (400, 000 amu) and pure Au₂₀₅₇ (405, 229 amu) clusters were produced by gas-phase synthesis with a magnetron sputtering, gas condensation cluster beam source and deposited onto silica supports. Chemical characterisation of the deposited clusters was provided by XPS and LEIS measurements. Upon heating the clusters in an O₂/CO environment to simulate catalytic reaction conditions, the surface composition of the Au/Ti clusters was changed by a segregation process, but both Au and Ti were still visible on the surface.

The sintering behaviour of the clusters under electron beam annealing was explored by aberration-corrected STEM imaging in real space and real time. Two neighbouring Au₂₀₅₇ clusters in a dimer were found to quickly migrate and, in a second slower phase, coalesce with each other. In contrast, Au/Ti dimers showed a strong anchoring effect against sintering due to the presence of the reactive Ti atoms, most notably when the gap between them exceeded 0.60 nm. Sintering can still happen if two Au/Ti clusters are extremely close to each other, but this

is due to atom diffusion between the two clusters instead of cluster migration. Sintering is expected to be exceedingly slow if the distance between the Au/Ti clusters is large enough and the diffusing atoms cannot “build a bridge” in between.

DFT calculations show that, in model bimetallic clusters (20 atoms), the Au atoms prefer a position at the surface of the clusters, in good agreement with the outcome of the LEIS experiments. The calculations furthermore show that Au clusters can be bonded much more strongly (by a factor of 5) to silica support by alloying them with Ti. This effect is due to the increased reactivity of the Au/Ti bimetallic clusters when they present a surface containing a reactive metal (Ti). Future computations may address the role of the oxidation of the bimetallic Au/Ti clusters, but the qualitative enhancement of surface anchoring against sintering is expected to be preserved. The presence of surface Au atoms in size-selected Au/Ti nanoalloy clusters and the anchoring effect due to Ti incorporation may open up new possibilities in Au-based nanocatalysis.

References

- [1] Niu Y, Schlexer P, Sebok B, Chorkendorff I, Pacchioni G, Palmer RE. Reduced sintering of mass-selected Au clusters on SiO₂ by alloying with Ti: an aberration-corrected STEM and computational study. *Nanoscale* **2018**, 10(5): 2363-2370.
- [2] Hvolbæk B, Janssens TVW, Clausen BS, Falsig H, Christensen CH, Nørskov JK. Catalytic activity of Au nanoparticles. *Nano Today* **2007**, 2(4): 14-18.
- [3] Zhang L, Persaud R, Madey TE. Ultrathin metal films on a metal oxide surface: growth of Au on TiO₂ (110). *Physical Review B* **1997**, 56(16): 10549-10557.
- [4] Parker SC, Grant AW, Bondzie VA, Campbell CT. Island growth kinetics during the vapor deposition of gold onto TiO₂(110). *Surf. Sci.* **1999**, 441(1): 10-20.
- [5] Veith GM, Lupini AR, Rashkeev S, Pennycook SJ, Mullins DR, Schwartz V, *et al.* Thermal stability and catalytic activity of gold nanoparticles supported on silica. *J. Catal.* **2009**, 262(1): 92-101.
- [6] Schlexer P, Pacchioni G. Adsorption and dimerization of late transition metal atoms on the regular and defective quartz (001) surface. *Top. Catal.* **2017**, 60(6-7): 459-470.
- [7] Yang F, Chen MS, Goodman DW. Sintering of Au particles supported on TiO₂(110) during CO oxidation. *Journal of Physical Chemistry C* **2009**, 113(1): 254-260.
- [8] Hu KJ, Plant SR, Ellis PR, Brown CM, Bishop PT, Palmer RE. Atomic resolution observation of a size-dependent change in the ripening modes of mass-selected Au nanoclusters involved in CO oxidation. *J. Am. Chem. Soc.* **2015**, 137(48): 15161-15168.
- [9] Cao A, Lu R, Veser G. Stabilizing metal nanoparticles for heterogeneous catalysis. *Phys. Chem. Chem. Phys.* **2010**, 12(41): 13499-13510.
- [10] Hernandez-Fernandez P, Masini F, McCarthy DN, Strebel CE, Friebel D, Deiana D, *et al.* Mass-selected nanoparticles of Pt_xY as model catalysts for oxygen electroreduction. *Nat. Chem.* **2014**, 6(8): 732-738.

- [11] Velazquez-Palenzuela A, Masini F, Pedersen AF, Escudero-Escribano M, Deiana D, Malacrida P, *et al.* The enhanced activity of mass-selected ptxgd nanoparticles for oxygen electroreduction. *J. Catal.* **2015**, 328: 297-307.
- [12] Holse C, Elkjaer CF, Nierhoff A, Sehested J, Chorkendorff I, Helveg S, *et al.* Dynamic behavior of CuZn nanoparticles under oxidizing and reducing conditions. *Journal of Physical Chemistry C* **2015**, 119(5): 2804-2812.
- [13] Liu XY, Wang AQ, Wang XD, Mou CY, Zhang T. Au-Cu alloy nanoparticles confined in SBA-15 as a highly efficient catalyst for CO oxidation. *Chem. Commun.* **2008**(27): 3187-3189.
- [14] Gomez-Cortes A, Diaz G, Zanella R, Ramirez H, Santiago P, Saniger JM. Au-Ir/TiO₂ prepared by deposition precipitation with urea: improved activity and stability in CO oxidation. *Journal of Physical Chemistry C* **2009**, 113(22): 9710-9720.
- [15] Liu XY, Wang AQ, Yang XF, Zhang T, Mou CY, Su DS, *et al.* Synthesis of thermally stable and highly active bimetallic Au-Ag nanoparticles on inert supports. *Chem. Mater.* **2009**, 21(2): 410-418.
- [16] Ma GC, Binder A, Chi MF, Liu C, Jin RC, Jiang DE, *et al.* Stabilizing gold clusters by heterostructured transition-metal oxide-mesoporous silica supports for enhanced catalytic activities for CO oxidation. *Chem. Commun.* **2012**, 48(93): 11413-11415.
- [17] Guan YJ, Hensen EJM. Selective oxidation of ethanol to acetaldehyde by Au-Ir catalysts. *J. Catal.* **2013**, 305: 135-145.
- [18] Sandoval A, Louis C, Zanella R. Improved activity and stability in CO oxidation of bimetallic Au-Cu/TiO₂ catalysts prepared by deposition-precipitation with urea. *Applied Catalysis B-Environmental* **2013**, 140: 363-377.

- [19] Han CW, Majumdar P, Marinero EE, Aguilar-Tapia A, Zanella R, Greeley J, *et al.* Highly stable bimetallic AuIr/TiO₂ catalyst: physical origins of the intrinsic high stability against sintering. *Nano Lett.* **2015**, 15(12): 8141-8147.
- [20] Kresse G, Hafner J. Ab-initio molecular-dynamics for liquid-metals. *Physical Review B* **1993**, 47(1): 558-561.
- [21] Kresse G, Hafner J. Ab-initio molecular dynamics simulation of the liquid-metal amorphous-semiconductor transition in germanium. *Physical Review B* **1994**, 49(20): 14251-14269.
- [22] Kresse G, Furthmuller J. Efficient iterative schemes for ab initio total-energy calculations using a plane-wave basis set. *Physical Review B* **1996**, 54(16): 11169-11186.
- [23] Kresse G, Furthmuller J. Efficiency of ab-initio total energy calculations for metals and semiconductors using a plane-wave basis set. *Computational Materials Science* **1996**, 6(1): 15-50.
- [24] Perdew JP, Burke K, Ernzerhof M. Generalized gradient approximation made simple. *Phys. Rev. Lett.* **1996**, 77(18): 3865-3868.
- [25] Perdew JP, Burke K, Ernzerhof M. Generalized gradient approximation made simple. *Phys. Rev. Lett.* **1997**, 78(7): 1396-1396.
- [26] Blochl PE. Projector augmented-wave method. *Physical Review B* **1994**, 50(24): 17953-17979.
- [27] Kresse G, Joubert D. From ultrasoft pseudopotentials to the projector augmented-wave method. *Physical Review B* **1999**, 59(3): 1758-1775.
- [28] Schlexer P, Pacchioni G. Modelling of an ultra-thin silicatene/silicon-carbide hybrid film. *Journal of Physics-Condensed Matter* **2016**, 28(36).

- [29] Monkhorst HJ, Pack JD. Special points for brillouin-zone integrations. *Physical Review B* **1976**, 13(12): 5188-5192.
- [30] Grimme S. Semiempirical GGA-type density functional constructed with a long-range dispersion correction. *J. Comput. Chem.* **2006**, 27(15): 1787-1799.
- [31] Tosoni S, Sauer J. Accurate quantum chemical energies for the interaction of hydrocarbons with oxide surfaces: CH₄/MgO(001). *Phys. Chem. Chem. Phys.* **2010**, 12(42): 14330-14340.
- [32] Henkelman G, Arnaldsson A, Jonsson H. A fast and robust algorithm for bader decomposition of charge density. *Computational Materials Science* **2006**, 36(3): 354-360.
- [33] Sanville E, Kenny SD, Smith R, Henkelman G. Improved grid-based algorithm for bader charge allocation. *J. Comput. Chem.* **2007**, 28(5): 899-908.
- [34] Tang W, Sanville E, Henkelman G. A grid-based bader analysis algorithm without lattice bias. *Journal of Physics-Condensed Matter* **2009**, 21(8).
- [35] Young N, Li Z, Chen Y, Palomba S, Di Vece M, Palmer R. Weighing supported nanoparticles: size-selected clusters as mass standards in nanometrology. *Phys. Rev. Lett.* **2008**, 101(24).
- [36] Arkill KP, Mantell JM, Plant SR, Verkade P, Palmer RE. Using size-selected gold clusters on graphene oxide films to aid cryo-transmission electron tomography alignment. *Sci. Rep.* **2015**, 5: 9234.
- [37] Han Y, He DS, Liu Y, Xie S, Tsukuda T, Li ZY. Size and shape of nanoclusters: single-shot imaging approach. *Small* **2012**, 8(15): 2361-2364.
- [38] Batson PE, Reyes-Coronado A, Barrera RG, Rivacoba A, Echenique PM, Aizpurua J. Plasmonic nanobilliards: controlling nanoparticle movement using forces induced by swift electrons. *Nano Lett.* **2011**, 11(8): 3388-3393.

- [39] Batson PE. Surface plasmon coupling in clusters of small spheres. *Phys. Rev. Lett.* **1982**, 49(13): 936-940.
- [40] Wang ZW, Palmer RE. Direct atomic imaging and dynamical fluctuations of the tetrahedral Au₂₀ cluster. *Nanoscale* **2012**, 4(16): 4947-4949.
- [41] Gruene P, Rayner DM, Redlich B, van der Meer AFG, Lyon JT, Meijer G, *et al.* Structures of neutral Au₇, Au₁₉, and Au₂₀ clusters in the gas phase. *Science* **2008**, 321(5889): 674-676.
- [42] Molina LM, Hammer B. The activity of the tetrahedral Au₂₀ cluster: charging and impurity effects. *J. Catal.* **2005**, 233(2): 399-404.
- [43] Armistead C, Tyler A, Hambleton F, Mitchell S, Hockey JA. Surface hydroxylation of silica. *The Journal of Physical Chemistry* **1969**, 73(11): 3947-3953.
- [44] D'Souza AS, Pantano CG. Mechanisms for silanol formation on amorphous silica fracture surfaces. *J. Am. Ceram. Soc.* **1999**, 82(5): 1289-1293.

Chapter 6

Conclusions and Outlook

This thesis focuses on the production, characterisation and catalytic performance of nanoclusters fabricated by cluster beam deposition based with the magnetron sputtering, gas condensation technique. MoS₂-based clusters and Au-based clusters have been demonstrated for electrochemistry (HER) and gas phase heterogeneous catalysis (CO oxidation), respectively. The atomic structure analysis of the clusters was performed with aberration-corrected HAADF-STEM, and the chemical analysis was conducted with EDX, XPS and LEIS.

Size-controlled (MoS₂)₃₀₀ clusters deposited on amorphous carbon present an incomplete multi-layer structure with the absence of extended crystalline order. Such a layered structure was also found in Ni-MoS₂ hybrid clusters [with the mass corresponding to (MoS₂)₁₀₀₀] produced by dual-magnetron sputtering. The EDX mapping of the aberration-corrected HAADF-STEM images confirms the hybrid nature of Ni-MoS₂ clusters. But the composition analysis shows that there is no fixed ratio of Ni atoms to MoS₂ units in the hybrid clusters. XPS measurements reveal the sulphur-deficient nature in both MoS₂ clusters and Ni-MoS₂ hybrid clusters, and the ratios of Mo:S are 1:0.9 and 1:1.8, respectively. Compared with the MoS₂ clusters, a significant enhancement in HER activity by the Ni-MoS₂ hybrid clusters was found when Ni dopant atoms are oxidised: approx. 100 mV shift in the onset potential and an almost 3-fold increase in exchange current densities. The unaffected Tafel slope ($\approx 120 \text{ mVdec}^{-1}$) indicates the HER catalytic mechanism (Volmer mechanism) is not altered by the Ni-MoS₂ hybrid clusters.

In order to overcome the sulphur deficiency of MoS₂ clusters, a sulphur-enrichment technique based on a combination of sulphur addition (by sublimation) and annealing inside the cluster beam vacuum chamber was performed on size-selected MoS₂ clusters. This process led to a notable increase in extended crystallinity and a moderate increase in size (from 5.5 nm to 6.0 nm in diameter). XPS measurements confirm the sulphur-rich nature with a Mo:S ratio of 1:4.9. Compared with the as-deposited MoS₂ clusters, the clusters treated with annealing only still present poorly ordered structures but evolve into both larger and smaller sizes due to decomposition and coalescence; whereas the clusters treated with simply sulphur addition are partially crystallized and retain their size. Thus, the combination of annealing and sulphur addition is the necessary step to obtain the most crystalline MoS₂ clusters. In addition, during the cluster deposition, a support effect was found while MoS₂ clusters were deposited onto silica films. The size-selected clusters on silica form single- or multi-wall Fullerene-like cage with high stability.

Compared with Ni-MoS₂ clusters, the sulphur-enriched MoS₂ clusters show even more enhancement on the HER activities with more than 30-fold increases in exchange current densities. The mass activity analysis of sulphur-enriched (MoS₂)₁₀₀₀ size-selected clusters reveals a remarkable performance on HER at the ultra-low loading level. In the future, doping TM elements (Fe, Co, Ni) into sulphur-enriched MoS₂ clusters could be conducted to verify several theoretical studies, which treat crystalline MoS₂. The catalytic activity of sulphur-enriched MoS₂ clusters [TM-MoS_{2+x}] in HER should be further improved by TM- MoS_{2+x} hybrid clusters.

Au nanoparticles have proved to be good catalysts with genuine potential in technological applications, however, a major issue hindering their implementation is their rapid sintering. Here, we explored the stabilisation of supported Au clusters against sintering by alloying with Ti. Size-selected Au₂₀₅₇ clusters and similar mass Au/Ti nanoalloy clusters (400, 000 amu)

were produced by cluster beam deposition onto silica films. XPS and LEIS measurements were conducted on both as-deposited clusters and the clusters treated with a simulative catalytic reaction condition ($O_2:CO=4:1$, $100^\circ C$). The chemical characterization shows that the surface composition of the Au/Ti clusters was changed by a segregation process, but both Au and Ti were still visible on the surface of the clusters. This is in good agreement with the DFT calculations on model bimetallic clusters ($Au_{10}Ti_{10}$).

A strong anchoring effect was found in the case of Au/Ti clusters by HAADF-STEM study and confirmed by DFT calculation. Different sintering mechanisms were revealed between Au_{2057} cluster dimers and Au/Ti cluster dimers. In the case of Au_{2057} clusters, the two neighbouring clusters in a dimer first migrate quickly and then coalesce with each other in a second slower phase. In contrast, due to the presence of the reactive Ti atoms, Au/Ti dimers were strongly stabilised against sintering by stopping cluster migration, most notably when the gap between them exceeded 0.60 nm. Sintering can still happen if two Au/Ti clusters are extremely close to each other, but this is due to the physical connection built by the atom diffusion between the two clusters. Sintering is expected to be exceedingly slow if the distance between the Au/Ti clusters is large enough so that the diffusing atoms cannot “build a bridge” in between.

Preliminary CO oxidation measurements on Au and Au/Ti clusters indicates Au/Ti clusters are promising as catalysts. However, there were problems with steady catalytic performance due to technical issues in the micro-reactor set-up. Future tests of the catalytic activity could be carried on once these technical issues are solved. CO oxidation measurement could also be performed with the conventional method (e.g. the plug flow reactor). Instead of clusters ~ 4.0 nm in diameter, smaller clusters may be used for future investigations, since they are more active and can generate stronger production signals.

In general, cluster beam deposition has been demonstrated as a versatile technique for cluster fabrication and modification for different applications. In this work, MoS₂ clusters have been fabricated and tested for HER. Beyond that, the sulphur-enriched MoS₂ clusters with crystalline structure can provide a tunable band gap for visible-light harvesting and abundant active sulphur-saturated edges, which can be studied as photocatalysts for hydrogen production, photosynthesis and etc. Moreover, crystalline MoS₂ can provide suitable interlayer spacing for ion accommodation, which can be used for battery studies. The Au/Ti binary clusters utilised in this work can also be tested as catalysts for other reactions (e.g. isomerization of epoxides into allylic alcohols), and the Au clusters can also be alloyed with other elements to catalyse corresponding reactions (e.g. Au/Si for benzylation of aromatics).